The Behavior of Orthopyroxene in Carbonatitic Melts

by

Rebecca Susan Stone

A thesis submitted in partial fulfillment of the requirements for the degree of

Master of Science

Department of Earth and Atmospheric Sciences
University of Alberta

© Rebecca Susan Stone, 2016

Abstract

The composition of primary kimberlitic melts has been the subject of much debate because of the heterogeneous nature of kimberlites, their ubiquitous modification by mantle and crustal contamination, their high susceptibility to alteration during and after emplacement, and the fact that the melts do not quench to a glass. Recently Russell et al. (2012) proposed that primary kimberlitic melts are originally carbonatitic. In their model, the melt assimilates orthopyroxene during ascent because of its low silica activity, which causes the melt to evolve to more kimberlitic compositions and triggers the massive exsolution of CO_2, which in turn explains the rapid ascent of the kimberlite magma. Russell et al. (2012) supported their model with experiments performed at atmospheric pressures that used Na_2CO_3 as the model carbonatitic melt. To better simulate the conditions of a rising kimberlite melt in the mantle I investigated the assimilation of orthopyroxene in a variety of carbonatitic melts in the system $CaO\text{-}MgO\text{-}Al_2O_3\text{-}SiO_2\text{-}CO_2 \pm H_2O$ at pressures between 2.5 and 6.0 GPa. These melts had been determined to be in equilibrium with lherzolite assemblages (Opx + Cpx + Ol ± Grt) at pressures of 6, 6.9, 10, and 16.5 GPa in previous studies (Dalton and Presnall, 1998; Girnis et al., 2011; Keshav and Gudfinnsson, 2014; Ghosh et al., 2014).

At pressures between 4 GPa and 6 GPa, orthopyroxene remained in equilibrium with the carbonatitic melt with no signs of assimilation into the melt, nor were there any signs of CO_2 exsolution. At 2.5 GPa the experiments

show that carbonatitic melt and orthopyroxene reacted to form olivine and diopside, exsolving CO_2. The formation of clinopyroxene in this orthopyroxene assimilation reaction, but its absence in kimberlite at the surface, can be explained by a second decarbonation reaction at lower pressure where clinopyroxene reacts with a carbonatitic melt to form more forsterite and additional CO_2 exsolution further driving kimberlite ascent. This reaction could also cause the evolution of the melt towards more calcitic compositions or the crystallization of calcite, explaining why calcite rather than dolomite is the common groundmass mineral in kimberlite. Xenocrystic clinopyroxene could also contribute to this reaction, making it an important secondary mineral for kimberlite melt evolution.

In addition to the assimilation experiments, a number of orthopyroxene and xenolith assimilation calculations using the same carbonatitic melts in our experiments were done in order to determine whether carbonatites can indeed evolve to kimberlites via mantle contamination. Even at 50 wt.% mantle contamination none of the melts reach kimberlite compositions by orthopyroxene assimilation. However, by adding clinopyroxene and garnet to the assimilation calculation, the Girnis et al. (2011) composition which lies more towards a transitional melt composition (intermediate between that of a carbonatite and a kimberlite) can evolve to kimberlitic melts. It is also possible through extensive orthopyroxene assimilation, fuelled not only by bulk mantle contamination but by wallrock reactions as well, that a range of carbonatitic melts can evolve to kimberlite compositions.

In supplementary calculations (Appendix 5), the possible correlation of kimberlite composition to the orthopyroxene content of the lithospheric mantle was explored. The results show that weak correlation exists between the compositions of kimberlites and the petrology of xenoliths at the craton scale, but no correlation is present when compared on the scale of individual kimberlite fields.

Future work must look at the contribution of other mantle minerals in addition to orthopyroxene in more compositionally complex systems to fully understand how kimberlites form.

Acknowledgements

First I would like to acknowledge the Natural Sciences and Engineering Research Council (NSERC) Discovery Grant which provided funding for this thesis.

I would like to thank Diane Caird for training me on how to machine the parts used in the high pressure and temperature experiments, make the 18/11 M HT assemblies, and operate the multi-anvil apparatus. She also was responsible for running and interpreting the x-ray diffraction analyses of the synthetic enstatite synthesized for this project.

Andrew Locock trained me on the JEOL electron microprobe and taught me how to get good WDS data analyses for this project. His help with this and his general comments on this project were greatly appreciated.

I would like to thank Graham Pearson for providing the kimberlite and xenolith databases and suggesting that I investigate the relationships between kimberlite silica content and orthopyroxene content of the host craton.

Martin Von Dollen was instrumental in creating a new mounting and polishing procedure for the carbonatitic melts, I thank him for his contribution

Finally I would like to thank my supervisor, Robert Luth, for training me on the piston cylinder apparatus, his comments on this thesis, but most of all, for introducing me to the world of high pressure and temperature experimental petrology. You have given me many amazing opportunities and great guidance. Thank you for letting me work on this project and taking me on as a graduate student.

Table of Contents

List of Tables

List of Figures

Chapter 1: Introduction

1.1. Abstract

Constraining the composition of a kimberlitic melt when it first forms, known as the primary kimberlitic melt, has been a problem petrologists have been trying to solve for decades using a large variety of methods. There are many factors obscuring the original melt composition, but assimilation of mantle minerals such as orthopyroxene has great potential to change the primary kimberlite melt composition during ascent through the mantle to the composition of kimberlite observed in emplaced pipes. This chapter will provide background information on kimberlites, the ways that mantle contamination and the exsolution of volatiles can change the kimberlitic melt on ascent, the previous attempts to remove the effects of these processes, and current theories on kimberlite formation. The final section will introduce the aims of this thesis, which is to explore orthopyroxene dissolution in possible primary kimberlitic melts using high pressure and temperature multi-anvil experiments and orthopyroxene assimilation models.

1.2. Introduction

Kimberlites are a rare type of alkalic ultramafic rock found in association with ancient cratons throughout Earth's geological history. They are characterized by high CO_2 and H_2O contents, abundant mantle xenoliths and xenocrysts (25 – 50%), and highly silica-undersaturated whole-rock compositions. Kimberlitic melts are thought to form at depths between 200 and 650 km (Mitchell, 2008; Ringwood et al., 1992; Russell et al., 2012), and rise rapidly to the Earth's surface entraining abundant mantle and crustal material en route. When they reach the surface, they are emplaced in explosive eruptions to form diatremes as pyroclastics and pyroclastic breccias, with off-branching dykes and sills hosting hypabyssal-facies kimberlite (Figure 1.1, Mitchell 1995).

By entraining mantle material (xenoliths and xenocrysts) from various depths en route to the surface, kimberlites give geologists a valuable glimpse of the structure, mineralogy, and geochemistry of the upper mantle. Lherzolites and harzburgites dominate the xenolith assemblage found in kimberlites; other rock types such as mafic granulite, eclogites, dunites, pyroxenites, metasomatised peridotite, and glimmerites can also be present within the xenolith assemblage (Mitchell, 1986). Olivine is the most common xenocryst found in kimberlites, and can be accompanied by xenocrysts of clinopyroxene, pyrope, spinel, ilmenite, and in some cases diamond (Mitchell, 1986). It is the presence of diamond in particular that has generated such widespread economic and academic interest in kimberlites. Aside from their monetary value as a gemstone, diamonds and their mineral inclusions contain information on the upper mantle and transition zone complimentary to that gleaned from the other entrained xenocrysts and xenoliths. Diamond geochemistry, morphology, and their inclusions have been used to determine mantle chemistry, mineralogy, temperature, and oxygen fugacity (Shirey et al., 2013; Stachel and Harris, 2008; Stachel and Luth, 2015), which in turn helps constrain the different processes taking place within the mantle.

Not all kimberlite pipes host diamonds, however, and it is still not clear whether this is a result of the kimberlite not sampling diamondiferous mantle or of processes occurring in the kimberlite during ascent. Understanding how kimberlites form could provide a better understanding of diamond formation and the processes that take place in the upper mantle and transition zone. This is a difficult problem in that the original composition of kimberlitic melt is unknown because kimberlites are highly heterogeneous, contain many xenoliths and xenocrysts as outlined above, and are also highly susceptible to alteration once emplaced because of their ultra-basic nature. Furthermore, there are no examples of kimberlite melt that have quenched to glass. This large number of unknowns has led to a number of proposed "primary kimberlite" melt compositions and formation models. The next few sections will review the different processes that can change the primary kimberlitic melt composition, past attempts to constrain the melt composition, and the current theories on kimberlite formation.

1.3. Processes Concealing Primary Kimberlitic Melt Composition

1.3.1. Mantle Contamination:

As mantle xenoliths and xenocrysts are swept up by the kimberlitic melt, the differing stability of each mineral in the melt results in the preferential preservation of some xenoliths/xenocrysts, and the partial or complete dissolution of others, modifying the composition of the host kimberlitic melt. By comparing the xenolith/xenocryst assemblage to current estimates of mantle mineralogy, one can infer the relative stabilities of mantle minerals within a kimberlitic melt. The mineralogy of the peridotitic upper mantle consists on average of approximately 63-72% olivine, 20% orthopyroxene, 3-12% garnet, and 6-10% clinopyroxene (Pearson et al., 2003). If all mantle minerals were stable in kimberlitic melts, the xenocryst assemblage should be nearly identical to the mantle assemblage; however, this is not the case. Instead what is observed in kimberlites around the world is an almost entirely olivine-dominated xenocryst assemblage (Mitchell, 1986). Clinopyroxene and garnet are usually present, but in lower percentages than seen in the upper mantle and with textures that show dissolution or reactions with the melt, i.e. kelyphite rims on garnet. Orthopyroxene is completely absent or rare, sometimes present only as a few sparse grains showing extensive dissolution textures (Figure 1.2). By comparing these observations to the mineralogy of the upper mantle, one can deduce that olivine is highly stable in kimberlitic melts, clinopyroxene and garnet are unstable but have dissolution rates low enough to preserve some xenocrysts, and orthopyroxene is highly unstable. The near absence of orthopyroxene in the kimberlite xenocryst assemblage has major implications for kimberlite contamination because excessive amounts of dissolution of a mineral that is a major constituent of the mantle has the potential to change the kimberlitic melt significantly.

In order to understand the variable solubility of mantle minerals, petrologists have conducted dissolution experiments using a range of melt compositions, mantle conditions, and mineral assemblages. An early paper examined the dissolution of olivine, clinopyroxene, orthopyroxene, spinel, and garnet in alkali basalts (Brearley and Scarfe, 1986). They found that with increasing pressure at low levels of superheating that the relative stabilities of olivine, clinopyroxene, and orthopyroxene were controlled by the liquidus phase relationships of the melt. However, when the temperature was increased at constant pressure the stabilities of the liquidus minerals changed, which they attributed to the changing structure of the melt with temperature. Experiments on diopsidic melts show that with increasing temperature melts transition from polymerized pyroxene-like structures to less polymerized olivine-like structure dominated by SiO_4^{4-} units (Mysen et al., 1979). Therefore at low levels of superheating, clinopyroxene is more stable in the melt than olivine, but at higher levels olivine is more stable (Figure 1.3). Orthopyroxene was found to behave similarly to clinopyroxene at low pressures and olivine at high pressures, mostly likely because of liquidus phase relationships particular to the composition of alkali basalt used in the experiments.

Shaw et al. (1998) and Shaw (1999) studied orthopyroxene dissolution in similar, Si-undersaturated alkaline basalt melts at atmospheric pressure and mantle pressures between 0.4-2 GPa. He found that orthopyroxene dissolved rapidly (Shaw 1999) and formed complex reaction zones consisting of olivine, clinopyroxene, and a Si-rich glass similar to what had been observed previously in some mantle xenoliths (Shaw, 1999; Shaw et al., 1998). The presence of H_2O was found to greatly increase the rate of dissolution compared to anhydrous experiments. More recently orthopyroxene dissolution was studied in a natural kimberlitic starting composition from the Nyurbinskaya pipe (Chepurov et al., 2013). They studied the dissolution of orthopyroxene, clinopyroxene, olivine, and garnet at 4 GPa at temperatures between 1300 and 1500ºC and found that clinopyroxene had the highest dissolution rate at lower temperature followed by orthopyroxene, garnet, and then olivine. At temperatures above 1400ºC however, orthopyroxene becomes less stable and dissolves more rapidly. Chepurov et al. also observed that orthopyroxene begins melting incongruently leading to the formation of olivine, which simultaneously enriches the melt in SiO_2 at 1400ºC. However it is also possible that orthopyroxene can be assimilated via a reaction between enstatite and magnesite to form forsterite and CO_2 (Eggler et al., 1979). The observation that clinopyroxene is more unstable than orthopyroxene in these experiments, where the opposite is inferred from the observations on natural kimberlites outlined above, may imply that the kimberlitic compositions seen at the surface are significantly different than their original primary melts (in either major-element composition or volatile contents) and therefore are not appropriate proxies for studying xenocryst dissolution.

The reason why orthopyroxene becomes unstable in kimberlitic melts may be because of the low silica nature of the kimberlite and the relatively silicic composition of orthopyroxene (Mitchell, 1973). By using a combination of Schrienemakers' analysis and calculated reactions in P-T-log($a_{SiO_2}^{liq}$) space, Luth (2009) investigated how the activity of silica in a kimberlitic melt would affect the relative stabilities of orthopyroxene, clinopyroxene, and olivine en route to the surface. In cases where olivine and orthopyroxene are in equilibrium with a silicate liquid, the activity of silica in the liquid is buffered via the reaction:

$$Mg_2Si_2O_6(opx) = Mg_2SiO_4(fo) + SiO_2(liq) \qquad (1)$$

and the activity of silica increases with increasing temperature or with decreasing pressure. However in cases where the silica is no longer buffered by this reaction the activity of silica in the melt changes very little with decreasing pressure (Figure 1.4). Because of this and the fact that equation 1 is dependent on pressure, once a kimberlitic melt leaves its source region it is no longer in equilibrium with orthopyroxene. Thus any orthopyroxene that the liquid encounters should react with the melt to form forsterite and a SiO_2 enriched melt. The kinetics of this process of orthopyroxene dissolution in kimberlitic melts has yet to be investigated under mantle conditions.

As mentioned previously, lherzolites and harzburgites dominate the xenolith assemblage, often making up greater than 90% of the assemblage and rarely falling below 80% (Harte, 1983). Orthopyroxene is protected from dissolution in these rocks to some extent by neighbouring olivine and clinopyroxene grains. More pyroxene-rich rocks such as websterites and eclogites are much rarer, and may undergo partial assimilation during ascent due to the instability of orthopyroxene and clinopyroxene. Dunite also is a rare kimberlite xenolith; however unlike pyroxenites and eclogites, they are more likely to be fully preserved within the kimberlitic melt due to the modal proportion of stable olivine they contain. More exotic species such as MARIDs (**M**ica, **A**mphibole, **R**utile, **I**lmenite, **D**iopside) and PICs (**P**hlogopite, **I**lmenite, **C**linopyroxene) are also rare xenoliths found in kimberlites. Their similar REE (Rare Earth Element) profiles to Type II and Type I kimberlites, respectively, have led authors to suggest that these rocks form during or shortly before kimberlite volcanism events by metasomatism via alkaline silicate melts that are related to the primary kimberlitic melt e.g. (Grégoire et al., 2002). Their genetic link to kimberlitic magmatism may cause MARIDs and PICs to be relatively stable in a kimberlitic melt and will contribute little to mantle contamination.

Determining the extent of mantle contamination in a kimberlite is difficult. Some authors have tried estimating the degree of orthopyroxene contamination by assuming a fixed ratio between orthopyroxene and olivine, estimating the amount of xenocrystic olivine, and then using that to “correct” from the kimberlite composition (Patterson et al., 2009). However, there are difficulties in distinguishing xenocrystic and phenocrystic olivines because of their similar morphology but complicated petrology, which complicates estimates of xenocryst abundances (Brett et al., 2009; Bussweiler et al., 2015; Pilbeam et al., 2013). The ratio of olivine to orthopyroxene can also vary with depth and geographic location (Griffin et al., 1999; Griffin et al., 2003a; Griffin et al., 2003b; Pearson et al., 2003), so using one ratio for estimates is an oversimplification.

It is also unknown if the dissolution of clinopyroxene or the reaction between garnet and melt to create kelyphite rims has any appreciable effect on the melt composition and needs further study. However, given the high survivability of garnet and clinopyroxene relative to orthopyroxene, and their lower modal abundance in peridotitic mantle, reactions of garnet and clinopyroxene should have second-order effects on modifying the composition of the kimberlite melt. In order to determine the composition of primary kimberlitic melts, a better understanding of mantle contamination and better methods to constrain it are required.

1.3.2. Exsolution of Volatiles:

As the kimberlite melt ascends the decrease in pressure leads to the exsolution of volatiles, mainly CO_2 and H_2O (Brooker et al., 2011). Like other aspects of kimberlite melt composition, the original volatile content of the kimberlite is unknown because the extent of exsolution is unconstrained. Analyses of hypabyssal kimberlites have shown that at the surface kimberlites have volatile concentrations as high as 20 wt.% CO_2 and 15 wt.% H_2O (Brooker et al., 2011), but it is unclear how these values relate to the concentrations in the kimberlitic melt. However, kimberlites do host abundant amounts of calcite and phenocrystic olivine with high amounts of trace water consistent with results of other studies (Brooker et al., 2011).

Attempts to reconstruct the volatile content of kimberlites are complicated by post-emplacement alteration which is often quite extensive such as serpentinization, the most prevalent alteration found in kimberlites. The reaction replaces both olivine and calcite in the kimberlite, adding SiO_2, MgO, and H_2O while removing CaO and CO_2 (Sparks et al., 2009). Attempts to remove the affects of serpentinization have been complicated by the fact that some serpentine in kimberlite may be primary (Mitchell, 2008) and differentiating primary and secondary serpentine is not an easy task.

1.4 Past attempts on constraining kimberlitic melt composition:

For half a century petrologists have been trying to remove the above influences in order to estimate the composition of parental kimberlitic melts (the melt composition after mantle contamination and right before emplacement) or primary kimberlitic melts (the initial melt composition at the source free of any of the above influences). Petrologists have attempted this using a number of different techniques spanning the fields of petrology, whole-rock geochemistry, radiogenic and stable isotope geochemistry, experimental petrology, and modeling. This section will provide a review of these past attempts and the resulting kimberlitic melt compositions that have been proposed.

1.4.1 Hypabyssal Kimberlites and Modeling:

Petrologists use hypabyssal kimberlites to calculate the melt composition of the kimberlite melt when it nears the surface, not the primary kimberlitic melt composition, though some do not acknowledge this distinction explicitly. Having a better idea of the composition of the emplaced kimberlite may help estimate primary kimberlitic melt compositions once better models for removing mantle contamination and the effects of volatile exsolution are available. A summary of analyses of hypabyssal kimberlites by various authors are reported in Table 1.1 (Harris et al., 2004; Kjarsgaard et al., 2009; Kopylova et al., 2007; Le Roex et al., 2003; Price et al., 2000). Kopylova et al. (2007) recognized that their primary melt composition was too magnesian to be produced by partial melting of peridotite at high pressures. The more magnesian composition may be the result of serpentinization. Spark et al. (2009) took these compositions and corrected them for serpentinization. They attempted to reverse the effects of alteration by replacing serpentine with the appropriate amounts of olivine and calcite, which they found lowered the contents of SiO_2 and MgO of the kimberlite. None of the compositions suggested by Harris et al. (2004), Kopylova et al. (2007), and Le Roex et al. (2003) could dissolve the volatile concentrations characteristic of primitive kimberlites (Brooker et al., 2011). Kjarsgaard et al. (2009) tried to remove crustal contamination by filtering out kimberlites that showed crustal signatures and correcting for the entrainment of olivine or the partial assimilation of peridotite. They presented a range of melt compositions for the Lac de Gras kimberlite field that is representative of the intruding kimberlitic melt, which they recognized would differ from a melt generated at the source.

A study of the Foxtrot kimberlite field in Northern Québec attempted to remove the effects of mantle contamination from hypabyssal kimberlite (Patterson et al., 2009) by assuming that the majority of olivine was xenocrystic based on grain morphology and geochemistry, and that orthopyroxene had been completely assimilated into the melt in a ratio of 20% orthopyroxene to 80% olivine, and removed those influences from the bulk composition. Both the original melt and the resulting calculated parental melt is listed in Table 1.2. What resulted was a melt much lower in MgO and SiO_2 and more enriched in CO_2 as compared to the other hypabyssal melt compositions.

1.4.2 Melt Inclusions:

Inclusions found in megacrysts (large crystals around 1 to 20 cm in size from the mantle mineral assemblage that may be either genetically related (xenocryst) or a crystallization product (phenocryst) of the kimberlite) and xenocrysts have been interpreted to be samples of the melt in which they formed, possibly the primary kimberlitic melt. Araújo et al. (2009) and Achterbergh et al. (2002) found carbonatitic to Ca-Mg-silicic to Mg-silicic melts in Cr-diopside of megacrystalline lherzolite xenoliths from the Slave craton. Araújo et al. (2009) proposed that these inclusions were kimberlitic/carbonatitic melt that had metasomatised the peridotite and caused the recrystallization of the Cr-rich diopside that trapped the globules. Olivines, Cr-rich spinels, and diamonds from the same area also host carbonatite melt inclusions (Kamenetsky et al., 2012; Klein-BenDavid et al., 2007). It is possible that the inclusions may be from other precursor magmas that precede the kimberlite event; however, these findings have been interpreted as evidence to suggest primary kimberlitic melts are carbonatitic in nature.

1.4.3 Experimental Studies of Partial Melts in Equilibrium with Carbonated Peridotite:

In the 1970's, a series of experiments in the system $CaO-MgO-SiO_2-CO_2$ were performed that studied the compositions of melts produced by small amounts of partial melting of model peridotite (Wyllie and Huang, 1975). At constant pressure (~ 3 GPa), the melt produced was carbonatitic at temperatures between approximately 1200ºC to 1350ºC and become more kimberlitic at higher temperatures between approximately 1400ºC to 1550ºC. These results have led many to conclude that the genesis of primary kimberlite melt is through small degrees of partial melting of a carbonated peridotite (Harris et al., 2004; Kopylova et al., 2007; Le Roex et al., 2003; Price et al., 2000; Russell et al., 2012). The production of broadly kimberlitic melts in this manner has been thoroughly documented since Wyllie and Huang (1975). Researchers continued investigating other compositional systems i.e. Na_2O-CaO-Al_2O_3-MgO-SiO_2-CO_2 at lower pressures (Eggler, 1978) and also began new sets of experiments studying the mantle assemblages in equilibrium with melts similar to natural kimberlites (Eggler and Wendlandt, 1979a). A series of experiments at the end of the 70's found that volatiles have a significant impact on the production of these melts by lowering the solidus of carbonated peridotite (Wyllie, 1980). These early experiments were all conducted at pressures ranging from 0.5 to 2 GPa; too low to directly model the genesis of kimberlite, which forms between pressures of approximately 5 to 18 GPa. The first high-pressure experiments were done by Canil and Scarfe (1990) at pressures between 4 and 12 GPa using a series of systems ranging in complexity that included volatiles, CO_2 and/or H_2O (Canil and Scarfe, 1990). From their experiments they suggested that primary kimberlitic melts are produced at pressures greater than 7 GPa by the partial melting of a magnesite peridotite.

Nearly a decade later, using simple systems at pressures of 3 GPa and 6 GPa, Moore and Wood (1998) and Dalton and Presnall (1998) showed that there is a continuous transition from carbonate to silicate melts (kimberlitic) as the degree of partial melting increases in conjunction with temperature (Dalton and Presnall, 1998b; Moore and Wood, 1998). They found that there was a dramatic transition that occurred over a narrow temperature range of ≤ ~150ºC (Figure 1.5). The melt composition in between a carbonatite and kimberlite melt they called a "transitional" melt. Later groups found similar results as they increased the complexity of the systems used and varied peridotite composition over a range of temperatures and pressures (Brey et al., 2007; Dasgupta and Hirschmann; Foley et al., 2009; Ghosh et al., 2014; Girnis et al., 2011; Gudfinnsson and Presnall, 2005; Keshav and Gudfinnsson, 2014; Ringwood et al., 1992). Table 1.3 summarizes the pressures, temperatures, and systems used in these experiments.

Although melts with similar compositions to hypabyssal kimberlites can be produced by partial melting of carbonated peridotite; it is not guaranteed that these represent primary kimberlite melts because they are being compared to material that has undergone extensive contamination. Isotopic studies suggest that if they do originate in this manner, the peridotite needs to have a complex metasomatic history to explain the data (Mitchell, 2004). A set of experiments run by Mitchell (2004) studying the sub-liquidus phase relationships of a sample of a natural hypabyssal kimberlite from Ondermatjie at pressures of 5-12 GPa and 900-1400ºC also supports a complex metasomatised mantle source.

1.5 Current theories on kimberlite formation:

Ringwood et al. (1992) studied the liquidus mineralogy of an average Group 1 kimberlite at 16 GPa. They found that the kimberlitic melt was in equilibrium with majorite and wadsleyite. Based on these experiments, the close chemical relationship between ocean island basalts and kimberlites that in turn implies a connection with plumes, and the occurrence of these rock types close to old subducted oceanic lithosphere, Ringwood et al. (1992) presented an intricate model to explain the formation of kimberlites. In their model the source was created when a slab of subducted oceanic lithosphere approximately 50-100 km thick becomes trapped at the 650 km discontinuity creating a layer of garnetite. At the temperatures and pressures of the 650 km discontinuity the garnetite undergoes partial melting that metasomatises the overlying rock (consisting of majorite and wadsleyite) giving it enriched characteristics, such as LREE (Light Rare Earth Element) enrichment and higher U/Pb and Th/U ratios. After a long period of time (10^8 to 10^9 years), a rising convection current in the mantle causes the garnetite layer to buckle upwards and increases the ambient mantle temperature (Figure 1.6). Due to the refractory nature of the garnetite layer partial melting only occurs in the overlaying re-fertilized harzburgitic layer, creating kimberlitic, lamporitic, and low Al_2O_3 magmas that then quickly ascend to the surface.

Girnis et al. (1995) propose a more complicated model based on their own kimberlite liquidus experiments that investigated liquidus and sub-liquidus phases at pressures of 4.5-5.5 GPa and the results from Ringwood et al. (1992). Their work showed that a CO_2-saturated Group 1A kimberlite is in equilibrium with a depleted harzburgitic phase assemblage, similar in composition to some rare sub-calico harzburgite xenoliths found in kimberlite, at pressures between 5.5 to 6 GPa. The inconsistencies between the garnets produced in these experiments as compared to the majority of garnets found in kimberlite, especially in Cr and Ti contents, suggest that primary kimberlitic melts are not a result of simple partial melting of a depleted garnet harzburgite (Girnis et al., 1995). Because the isotopic signature of kimberlite suggests an asthenospheric origin, Girnis et al. 1995 proposed that kimberlitic melts are produced by the interaction of asthenospheric/transitional partial melts and depleted harzburgites sitting at the base of the lithosphere. If mantle temperatures are high enough then a CO_2 undersaturated primary kimberlitic will percolate up and become trapped in the lower lithosphere and the process of assimilating any surrounding magnesite while crystallizing olivine and garnet will cause CO_2 saturation eventually triggering CO_2 exsolution, leading to the rapid ascent of the kimberlite.

Recently, another model was proposed by Russell et al. (2012), who suggested that kimberlite melts are originally carbonatitic in composition, a theory that has been gaining popularity with a number of authors (Brooker et al., 2011; Bussweiler et al., 2015; Canil and Bellis, 2008; Girnis et al., 2011; Kamenetsky et al., 2012; Patterson et al., 2009). In the Russell et al. model, the carbonatitic melt transitions to a kimberlitic melt during ascent through orthopyroxene assimilation. After performing experiments with Na_2CO_3 and orthopyroxene at 1 atmosphere and temperatures between 1000 and 1100ºC, they found that the dissolution of orthopyroxene into the primary kimberlitic magma causes massive exsolution of CO_2 over very short time scales, which they proposed explains the rapid ascent inferred for kimberlites (Canil and Fedortchouk, 1999). Although the experiments that led to this model were very elegant, there were several issues with the experiments that require further examination. The carbonatitic melt used was oversimplified as they used Na_2CO_3 only and their experiments were conducted at atmospheric pressures, not at the conditions CO_2 exsolution would take place in the mantle.

1.6 Scope of this Thesis:

The aim of this thesis is to further investigate the viability of the Russell et al. (2012) model and to gain a better understanding of the interaction between orthopyroxene and possible kimberlitic melts. This will be accomplished by exploring orthopyroxene assimilation models using carbonatitic and kimberlitic compositions selected from the literature, studying the relationship between the concentration of silica in kimberlite with respect to the abundance of orthopyroxene in the lithosphere for cratons around the world, and finally, a series of orthopyroxene assimilation experiments similar to those done by Russell et al. (2012) using more complex carbonatite starting compositions and pressures/temperatures consistent with kimberlite formation conditions.

Chapter 1 Figures:

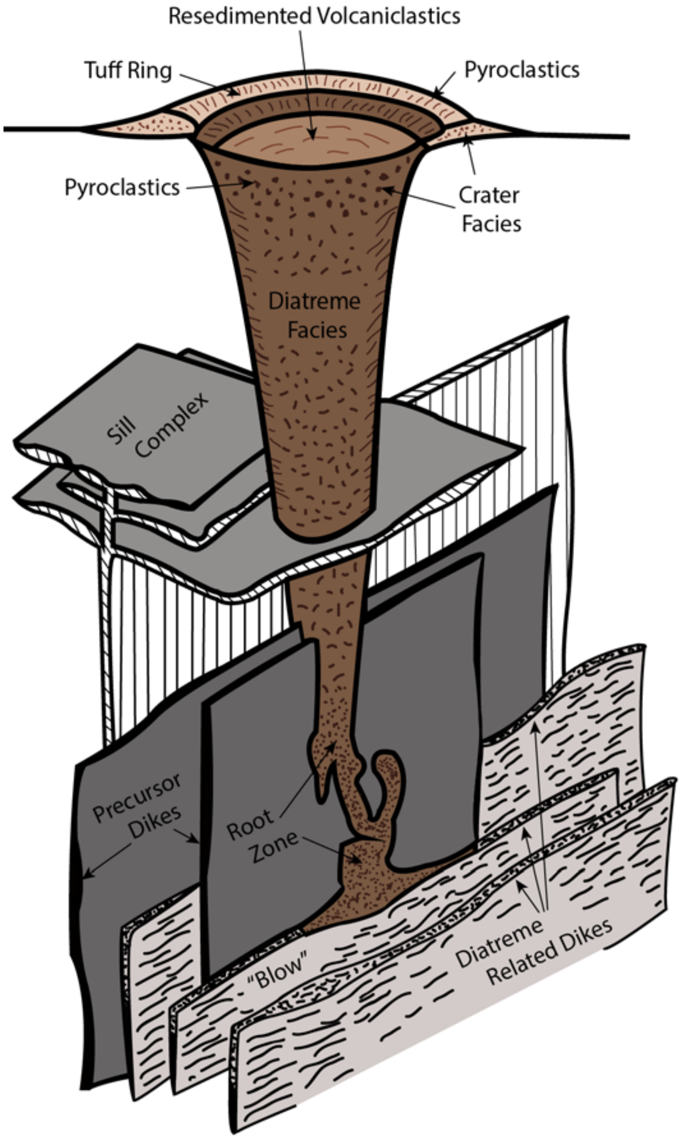

Figure 1.1: A model of a kimberlite showing all the structures including the crater, the diatreme, and the associated sills, dikes, root zone, and blow that host hypabyssal facies of kimberlite (Mitchell, 1986).

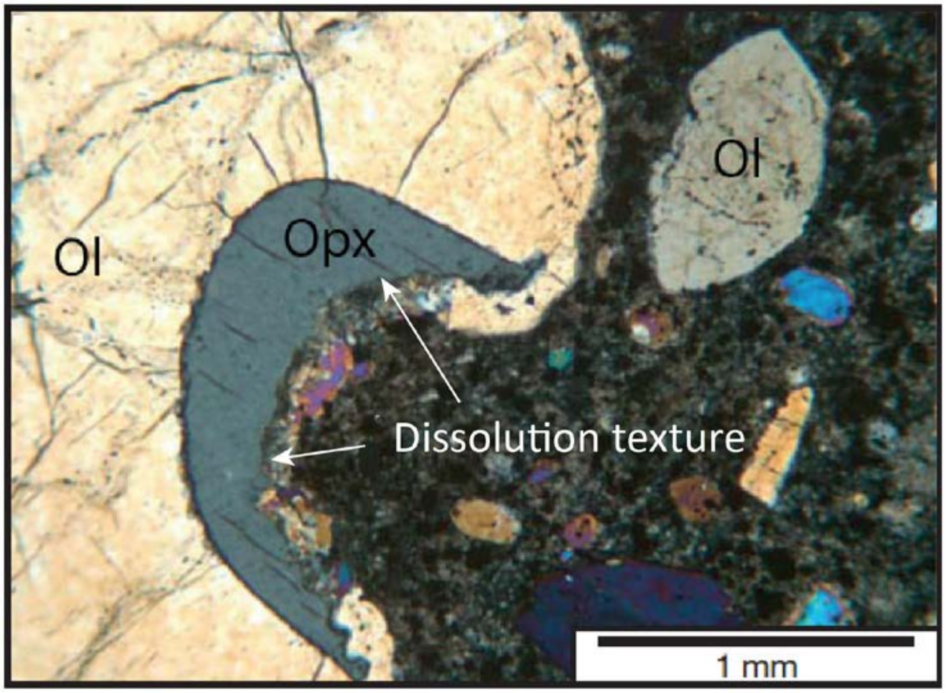

Figure 1.2: An example of a partially preserved orthopyroxene found in a kimberlite sample. The orthopyroxene grain was saved from complete dissolution by the encasing olivine grain. (Russell et al., 2012)

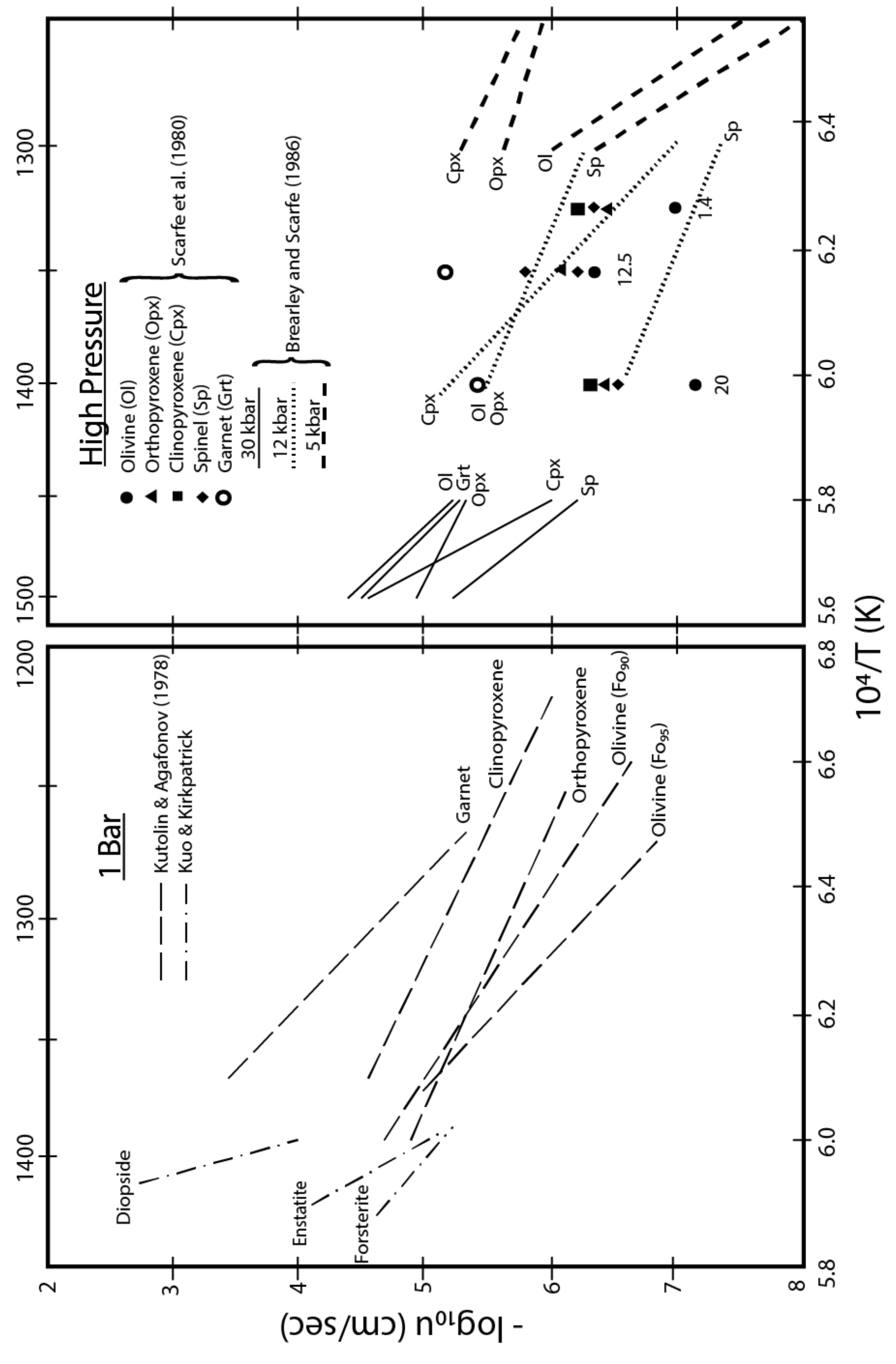

Figure 1.3: The results from the dissolution experiments of Brearley and Scarfe (1986) compared with previous studies at various conditions. These graphs show how the dissolution rates of several mantle minerals such as olivine, garnet, orthopyroxene, clinopyroxene, and spinel change with temperature at pressures of 0.001, 5, 12, and 30 kbar.

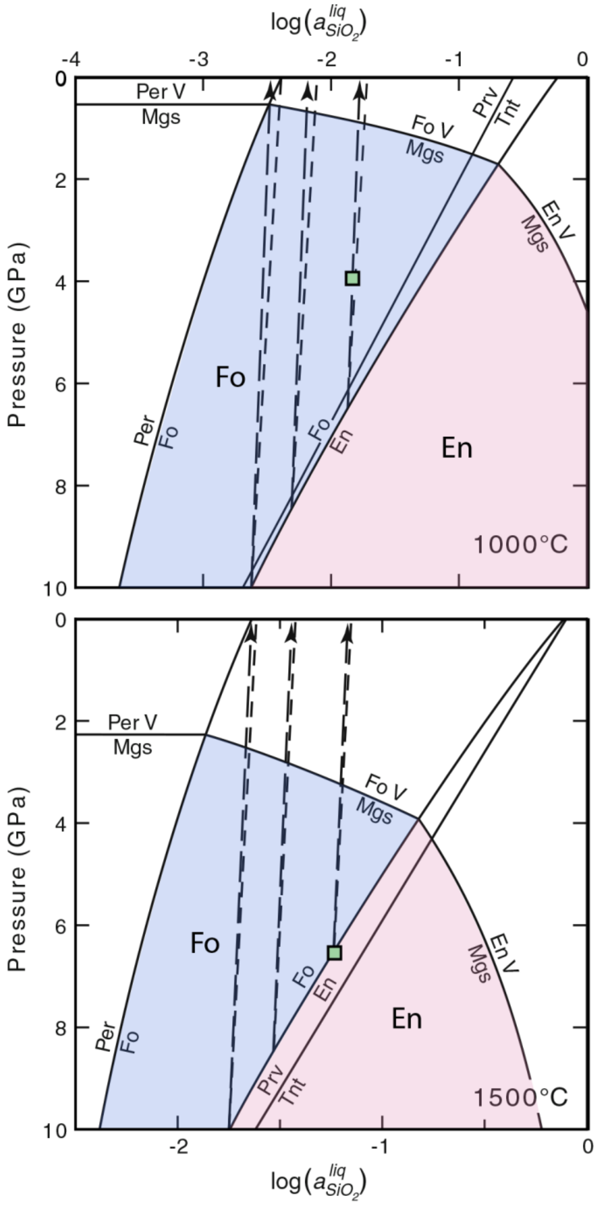

Figure 1.4: Isothermal P – $\log(a^{liq}_{SiO_2})$ plots from Luth (2009) at 1000 and 1500ºC. The near vertical dashed lines (indicating near constant activity of silica with changing pressure) shows the path an unbuffered melt originally in equilibrium with olivine and orthopyroxene (Fo-En reaction line, Eq. 1) during ascent. The two dash lines differ in the $(\bar{V}_{SiO_2} - \bar{V}^0_{SiO_2})$ value; the long dashed lines with arrowheads use a value from Carmichael (2002) and the short dashed lines use a value from Nicholls et al. (1971). Forsterite remains stable between the Fo-En reaction line and the Per-Fo reaction line.

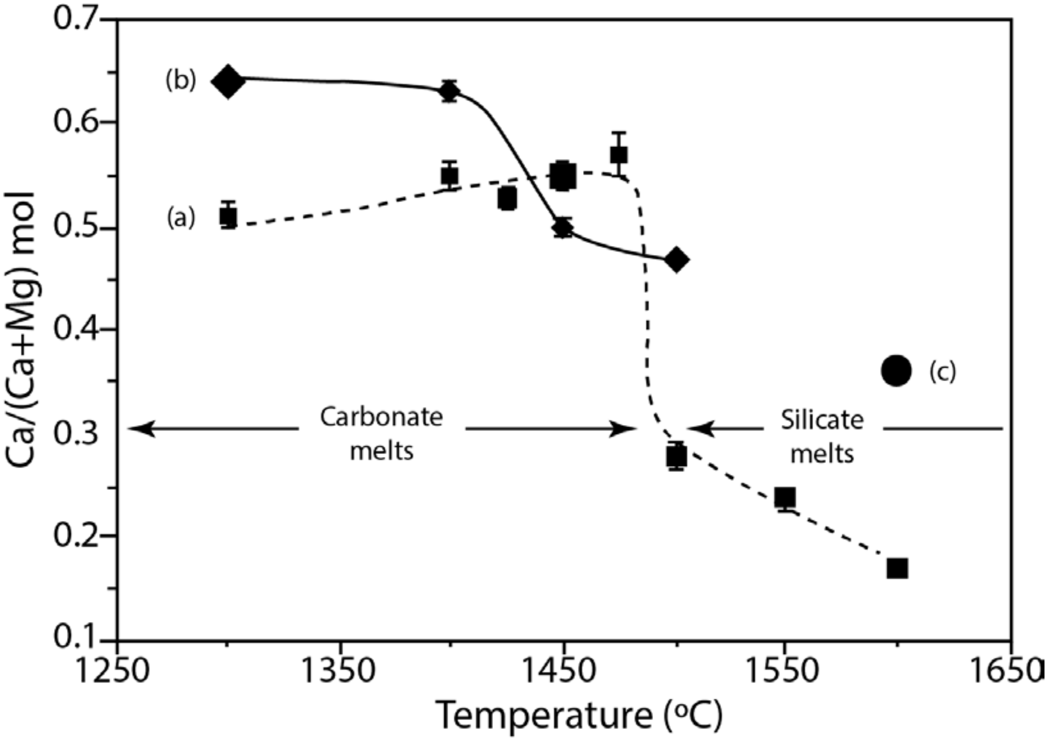

Figure 1.5: Ca/(Ca+Mg) versus temperature plot from Moore and Wood (1998) showing the rapid transition from carbonate to silicate melts with temperature. A, B, and C correspond to starting compositions used in the paper. All error bars represent 3 standard errors. Larger symbols indicate that the melt coexisted with a lherzolite mineral assemblage.

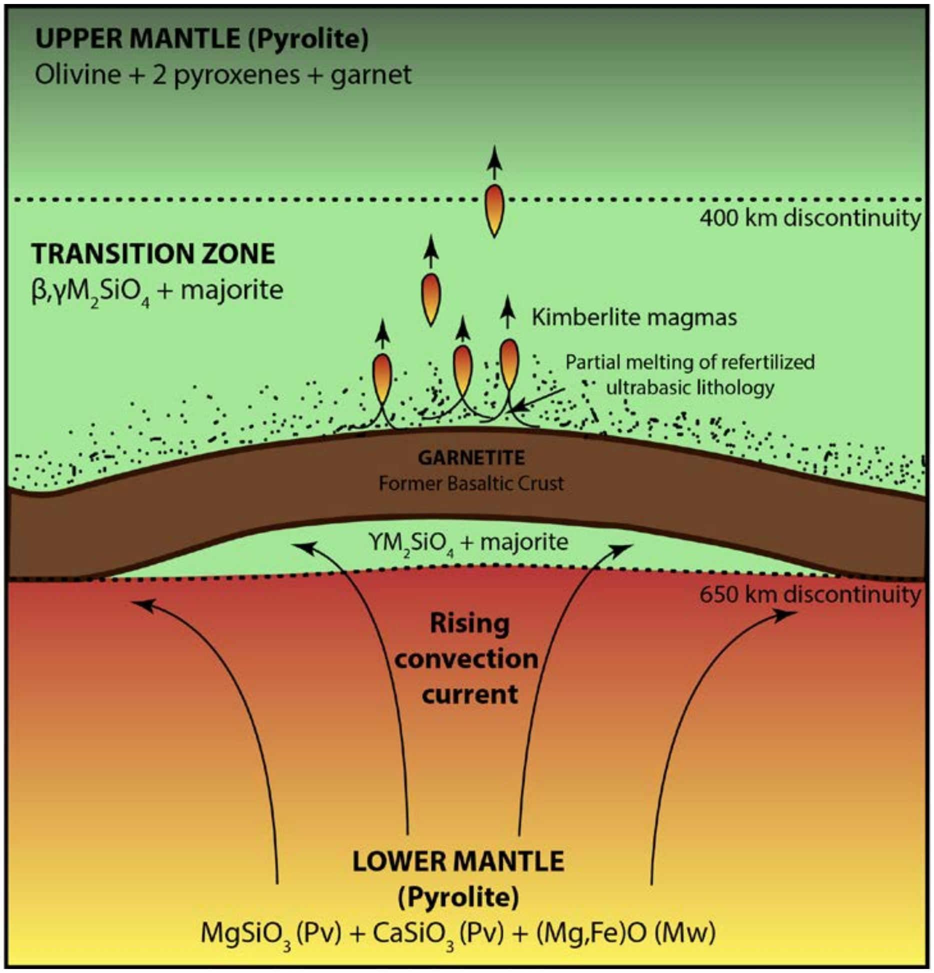

Figure 1.6: An illustration showing upwelling of the mantle causing a garnetite layer to buckle upward, heating the above re-fertilized harzburgite rock which initializes partial melting, creating kimberlitic melt. (Ringwood et al., 1992)

Chapter 1 Tables:

Table 1.1: Proposed kimberlitic/primary kimberlitic melt compositions

Study	Price et al. (2000)	Le Roex et al. (2003)	Harris et al. (2004)	Kopylova et al. (2009)	Kjarsgaard et al. (2009)
SiO_2	20.77 - 32.90	26 - 27	25	26 - 29.5	26.30 - 34.76
FeO*	5.43 - 7.48	8		7	7.32 - 8.92
MgO	16.65 - 34.41	26 - 27	26	25.7 - 28.7	28.79 - 34.38
CaO	7.48 - 25.45	12	15	11.3 - 15	6.90 - 9.56
Al_2O_3	1.61 - 2.06	2.2	2.3		1.87 - 3.42
CO_2	4.91 - 18.82	7	8.6	8.3 - 11.3	5.51 - 12.23
H_2O	5.30 - 7.10	2.3 - 10	5	7.6 - 9.4	8.94 - 12.50

Table 1.2: The composition of the Renard primary kimberlitic magma estimated via xenocrystic olivine and proportional orthopyroxene removal (Patterson, 2009)

Oxide wt%	Avg Renard	Renard[a]	Renard[b]
SiO_2	35.03	27.24	24.33
TiO_2	1.21	2.68	2.91
Al_2O_3	2.44	5.49	5.92
MgO	34.86	16.87	15.15
FeO	8.32	8.58	8.90
MnO	0.15	0.21	0.22
CaO	9.43	20.31	22.23
Na_2O	0.06	0.1	0.10
K_2O	0.79	1.82	1.96
P_2O_5	0.42	0.93	1.03
CO_2	7.28	15.77	17.25

[a] Composition calculated by removal of olivine mineral composition from whole rock data

[b] Composition calculated by removal of equivalent proportion of orthopyroxene

Table 1.3: A summary of the experimental conditions for studies investigating the compositions of melts in equilibrium with carbonated peridotite.

Study	P (GPa)	T (ºC)	System
Gudfinnsson and Presnall (2005)	3.0 - 8.0	1340-1800	$CaO-Al_2O_3-MgO-SiO_2-CO_2$
Brey et al. (2007)	6.0 - 10	1300-1700	$SiO_2-TiO_2-Al_2O_3-Cr_2O_3-FeO-MnO-NiO-MgO-CaO-Na_2O-K_2O-P_2O-CO_2$
Dasgupta and Hirschmann (2009)	6.6 - 8.6	1265-1470	$SiO_2-TiO_2-Al_2O_3-Cr_2O_3-FeO-MnO-MgO-CaO-Na_2O-K_2O-CO_2$
Foley et al (2009)	4.0 - 6.0	1090-1290	$SiO_2-TiO_2-Al_2O_3-FeO-MnO-NiO-MgO-CaO-Na_2O-K_2O-CO_2-H_2O$
Ghosh et al. (2014)	10.0 - 20.0	1600-2100	$SiO_2-TiO_2-Al_2O_3-Cr_2O_3-FeO-MnO-NiO-MgO-CaO-Na_2O-K_2O-P_2O-CO_2$
Keshav and Gudfinnsson (2014)	8.0 - 12.0	1500-1800	$CaO-Al_2O_3-MgO-SiO_2-CO_2$

Chapter 2: Orthopyroxene Dissolution Experiments

2.1 Introduction

As outlined in Chapter 1, the Russell et al. (2012) study performed a number of experiments using Na_2CO_3 as a proxy for a natural carbonatitic melt and crushed natural orthopyroxene to evaluate if assimilation of orthopyroxene in carbonatitic melt could produce a kimberlitic melt. In their experiments, they added increasing amounts of orthopyroxene ranging from 0 to 40 wt.% at atmospheric pressures and temperatures ranging from 1000 to 1100 ºC and measured the amount of CO_2 loss relative to an experiment run at the same conditions without any orthopyroxene added. Their results showed that increasing the amount of orthopyroxene resulted in more CO_2 exsolution, which leveled off when orthopyroxene saturation in the melt had been reached. The mechanism for the orthopyroxene assimilation proposed was that the low activity of SiO_2 in the carbonatitic melt caused the instability of orthopyroxene which incongruently dissolved into the melt, producing olivine. Increasing the SiO_2 content of the melt causes the CO_2 solubility to decrease, leading to the exsolution observed in these experiments which provides a mechanism to explain the rapid ascent of kimberlites to the surface.

This model provides an elegant solution to the primary kimberlitic melt composition problem, an explanation for the paucity of orthopyroxene in the xenocryst assemblage and resultant phenocrystic growth of olivine on xenocrystic grains, and a mechanism to explain the rapid ascent of a kimberlite. However, the pressure at which these experiments were run is much lower than the pressures at which a kimberlitic melt forms and the system used has a much simpler composition than a natural carbonatitic melt. These differences invoke the question of what the effect of higher pressures or more complex composition would be on the interaction between orthopyroxene and carbonatitic melts. The experiments presented in this chapter aim to answer this question, using pressures between 2.5 and 6.0 GPa and carbonatitic melts formed by low degrees partial melting of peridotitic rock at a range of different mantle pressure and temperature conditions chosen from the literature.

2.2 Methods

2.2.1 Starting Materials:

The starting compositions of all the carbonatite melts used for the present experiments are in the CaO – MgO - Al_2O_3 - SiO_2 - CO_2 ± H_2O system. For the CO_2-bearing melts, the starting materials were prepared by mixing and grinding reagent SiO_2 (99.95%), α-Al_2O_3 (99.99%), $CaCO_3$ (99.95%), $MgCO_3$ (Mt. Brussilhof), and MgO (99.95%) in an agate mortar in ethanol for approximately 10 minutes. The CO_2- and H_2O-bearing starting material was prepared using the same set of oxides, except, instead of using $MgCO_3$ and MgO as sources for MgO and/or CO_2, magnesium carbonate hydroxide pentahydrate ($(MgCO_3)_4 \cdot Mg(OH)_2 \cdot 5H_2O$, MCHP), was used as a source of MgO, CO_2, and H_2O. All the oxides, excluding MCHP, were dried at 120ºC for at least 1 hr before further preparation. The silicon, aluminum, and magnesium oxides were fired in a tube furnace for 25 hrs at 1000ºC to further remove any H_2O (Edgar, 1973). The calcium carbonate was dried for 5 hrs at 300ºC. The magnesite used was a natural magnesite from Mt. Brusiloff, British Columbia, Canada. This material was also used in a previous study (Enggist et al., 2012). Those authors hand-picked individual crystals with no visible inclusions that were then ground in an agate mortar. A full chemical analysis of the magnesite is given in Enggist et al. (2012). The MCHP was stored in a desiccator with the rest of the oxides with no further preparation.

The nominal composition of each carbonatitic melt used in the dissolution experiments are listed in Table 2.1. The melts chosen were compositions reported in the literature to be in equilibrium with lherzolite at pressures and temperatures where primary kimberlitic melt could form. DP

(KM14 in the original publication) was a carbonatitic melt in equilibrium with lherzolite at 6.0 GPa and 1380ºC (Dalton and Presnall, 1998b). Compositions C (M322), GP (PR-106), and K (K-10) all were melts in equilibrium with garnet-bearing lherzolite assemblages at 6 GPa, 6.9 GPa, and 10 GPa and 1400ºC, 1460 ºC, and 1500 ºC, respectively (Girnis et al., 2011; Gudfinnsson and Presnall, 2005; Keshav and Gudfinnsson, 2014). The highest pressure carbonatitic melt, G (D025), was in equilibrium with garnet and wadsleyite at 16.5 GPa and 1700ºC (Ghosh et al., 2014). The DP and K melt compositions were from CMAS + CO_2 systems and the G and C melt compositions were recalculated from more complex systems into CMAS + CO_2 and CMAS + CO_2 + H_2O.

The orthopyroxene used in the dissolution experiments was prepared by mixing equimolar amounts of SiO_2 and MgO under ethanol in an agate mortar for 10 minutes. The mixture was dried in an oven for 10 minutes at 120ºC and fired in a tube furnace at 1450ºC for 3 days. Afterwards, the powdered mixture was cooled, re-ground, re-dried, and then fired again at 1450ºC for 4 more days. The run product was analyzed on a Rigaku Geigerflex Powder Diffractometer which confirmed enstatite (both clinoenstatite and protoenstatite) formed. Minor cristobalite and forsterite peaks were also present (See Figure 2.1).

2.2.2 Experimental Setup and Analytical Methods:

For experiments at 2.5 GPa, ~10 mg of starting material was packed into a Pt capsule ~5mm long with an outer diameter of 3mm. The top of the capsule was then cleaned with ethanol, clamped shut using a triple crimp, wrapped in a wet kimwipe to minimize volatilization, and welded shut using a carbon rod arc welder. The capsule was weighed before and after welding in order to detect whether there had been sample loss during welding. Minor weight loss of 0.05 mg was routinely observed and was attributed to Pt volatilization during welding. Any samples where greater than 5% of the sample was lost were discarded and reloaded. In Appendix 1, Table A.1 shows the loading capsule data which includes the weights of the capsule and material added as well as the percent losses for each experiment.

The experiments were run in 12.7 mm talc-Pyrex assemblies in a solid-media, piston cylinder apparatus (Boyd and England, 1960) at the C. M. Scarfe Laboratory for Experimental Petrology, University of Alberta. A $W_{95}Re_5$-$W_{74}Re_{26}$ thermocouple was used to monitor temperature with no correction for pressure effects on emf. The experiment was first pressurized to approximately 80% of the run pressure before heating the sample. The sample was heated at a rate of 120ºC min^{-1} at a constant pressure. Once the run had reached its final temperature, the pressure was brought up to the desired level. Table 2.2 lists the run conditions for the piston cylinder experiments.

For experiments at > 2.5 GPa, capsules were prepared from 5mm long by 1.5mm outer diameter Pt tubing. The capsules contained ~ 2 - 3 mg of starting material. After cleaning the tops with ethanol to remove excess powder, the capsules were closed in a triple crimp, and welded (initially) on a carbon rod arc welder with a wet kimwipe to minimize volatilization of CO_2 or H_2O. As done for the piston cylinder experiments, any capsules that lost greater than 5% of the starting material were discarded. Towards the end of this study, a TIG Puk^{U4} Lampert arc welder was used to weld the capsules allowing for minimal loss of starting material. This welding system was a significant improvement over the carbon arc welder used previously and greatly simplified obtaining high quality welds with minimal heating of the capsules. Once the capsules were loaded they were formed into compact 1.5mm diameter cylinders using a brass metal plate and 1.5 mm diameter rod. The before-run length of the capsules was between ~ 2 – 3 mm.

All experiments at > 2.5 GPa were run in the USSA-2000 multi-anvil apparatus at the University of Alberta. The sample assemblies used were a 18/11 M high-temperature assembly with ZrO_2 sleeves (7 mm OD, 3mm ID) encased in a semi-sintered MgO-5%Cr_2O_3 octahedron as a pressure cell (Walter et al., 1995). A stepped graphite furnace was used, with the sample centered within the assembly using MgO spacers. An MgO sleeve protected the Pt capsule from direct contact with the graphite furnace. The $W_{95}Re_5$-$W_{74}Re_{26}$ thermocouple was inserted to the top of the Pt capsule axially by an Al_2O_3 four-bore thermocouple ceramic. Each assembly was dried at 120ºC for at least 10 minutes before being fired at 1000ºC without the sample capsule for 1 hr in a N_2-H_2 gas mixture to prevent the oxidization of the thermocouples or the graphite furnace. The assemblies were stored at 120ºC until ready for use.

For the run, assemblies were inserted into the cavity in the center of eight 32.5mm edge-length WC cubes with 11 mm triangular truncations. The thermocouples were protected from the cubes by Teflon sleeves. The emf reading was not corrected for pressure. Thick groves were cut into the pyrophyllite above the Teflon sleeves to decrease the likelihood of a thermocouple failure during the experiment. The assemblies were pressurized at room temperature and then heated at a rate of 30 mV (~30ºC/min) or 60 mV (~60ºC/min) per hour. At the completion of the experiment, the samples were quenched by cutting the power to the assembly, followed by the decompression at ~ 30 kbar oil pressure/hr. Table 2.2 lists the run conditions used for each experiment.

After the experiment, the capsule was mounted in epoxy (Petropoxy 154), ground so the length of the capsule was exposed, and then impregnated with a less viscous epoxy (EpoTek 301) to minimize plucking. The mounts were re-impregnated with epoxy between grinding using 240, 320, 400, and 600 size grits. The mounts were impregnated one more time before being polished using 5, 1, and 0.05 μm Al_2O_3 powder on a rotating felt wheel. The mounts were then cleaned with ethanol and stored in a dessicator before being carbon coated for electron microprobe analysis.

The experimental charges were analyzed on a JEOL 8900R electron microprobe (EPMA) at the University of Alberta. Silicates were analyzed using a 15 kV accelerating voltage, a 15 nA current, and a focused beam with 30 seconds counting time on the peak and 15 seconds on the background. Carbonates were usually analyzed using a 10 μm beam; though in some cases the beam had to be focused to 5 μm because of the small grain size. An accelerating voltage of 15 kV was used for the carbonates, and the current was set at 15 or 10 nA. Frank Smith pyrope, Fo93 olivine, diopside, dolomite, spinel, anorthite, and MgO were used as standards. The Phi-Rho-Z program supplied by JEOL was used to correct the raw data. Backscatter and secondary electron images were taken of the experimental run products to document the textural relationships present. All images were captured using a 15 kV voltage, a 15 nA current, and a focused beam.

2.3 Results

2.3.1 Mineralogy and Texture

2.3.1.1 Dalton and Presnall (DP) Experiments:

Figure 2.2 shows backscatter electron images (BSE) of experimental charges PC-DP-RS-001 and DP-RS-002 from the 2.5 GPa experiments using the carbonatitic starting material DP (Table 2.1). The contents of the capsule shown in Figure 2.2a, which had no orthopyroxene added, consists almost entirely of quenched carbonatitic melt which formed a network of dendrites ranging from 10 to 500 μm in length. A few grains of forsterite and spinel were also present, ranging in sizes of 5-15 μm and 1-20 μm, respectively. Figure 2.2b shows the experiment run at the same conditions as PC-DP-RS-001, except with 31 wt.% orthopyroxene in the starting material. The orthopyroxene added to the capsule is completely absent and is inferred to have assimilated into the carbonatitic melt. There is no evidence of the spinel grains observed in the previous experiment. Extensive forsterite is present as grains ranging between 1 and 75 μm in size. Also present are some large poikolitic grains of diopside 20 – 200 μm in size, containing forsterite oikocrysts (Figure 2.3). Some of the diopside grains are euhedral. The carbonatitic melt has once again quenched to a dendritic texture, but this time the dendrites are much finer, only growing to a maximum of ~ 30 μm in length. The experiment also contains vesicles, ranging from 5 to 550 μm in size. The capsule itself also preserves evidence of the exsolution of a gas phase in the bulging of the capsule and the increased amount of void space compared to that of run PC-DP-RS-001.

Figure 2.4 shows two more DP experiments from 4.5 GPa. Figure 2.4a, a backscatter image of run DP-RS-005, a run without any orthopyroxene added, shows that the majority of the capsule is a network of thin long dendrites of quenched carbonatitic melt accompanied by two large grains of forsterite that are ~ 200 and 400 μm in length, and some smaller grains of spinel and periclase averaging around ~ 15 μm in size. Run DPO-RS-004 (Figure 2.4b, secondary electron image and Figure 2.4c, BSE), shows the results with 13 wt.% orthopyroxene in the starting material added. No forsterite, periclase, or spinel is present, instead, the orthopyroxene appears stable in the carbonatitic melt, forming a layer of fine grains approximately 10-30 μm in size at the bottom of the capsule along with few grains of garnet of the same size. The carbonatitic melt once again forms a dendritic texture similar to the one formed in the DP-RS-005 run. There only possible evidence of CO_2 exsolution is two circular holes at the top of the capsule, though it is also possible this may be the result of plucking.

2.3.1.2 Keshav et al. (K) Experiments:

Using starting material K (Table 2.1), experiments K-RS-003 and KO-RS-001 were run at 4.5 GPa and 1600ºC. The backscatter electron images of the completed experiments are shown in Figure 2.5. K-RS-003 (Figure 2.5a), the orthopyroxene-free run, contains quenched carbonatitic melt with a dendritic texture. The dendrites are very coarse grained near the centre of the capsule and reach lengths of ~ 300 μm, but become finer grained closer to the walls of the platinum capsule. Two grains of forsterite (150 – 300 μm) are present at the bottom of the capsule along with three grains of garnet (~ 75 μm). Capsule KO-RS-001, which had 10.6 wt.% orthopyroxene, shows a similar dendritic texture as K-RS-003 in its carbonatitic melt. Forsterite and garnet are once again present, however the abundance and size of the forsterite has increased (the largest grain reaches a size of ~ 500 μm). The presence of magnesite in this experiment which was absent in the orthopyroxene-free experiment, the increase in the amount of forsterite and the relatively small amount of orthopyroxene suggests that there is a reaction taking place that does not result in exsolution of CO_2. Using the program CSpace and inputting forsterite, enstatite, diopside, garnet, dolomite, magnesite, and a melt with the composition of K-RS-003 (Table 2.3) in the CMAS + CO_2 system into the program's matrix analysis wizard shows the reaction melt + en → fo + grt + mag + di is the one reaction that can take place. There is no diopside present in the run, but it is possible that the diopside was not visible in this particular cross section of the capsule or that it was plucked during the grinding or polishing process (Figure 2.5).

2.3.1.3 Ghosh et al. (G) Experiments:

Figure 2.6 shows the backscatter electron images for runs G-RS-006 and GO-RS-003, at 4.5 GPa and 1650ºC, using starting material G (Table 2.1). G-RS-006 (Figure 2.6a), similar to the previous runs, is mainly carbonatitic melt quenched to a fine grained dendritic texture. Unlike the other orthopyroxene-free experiments, not all the carbonate in this run is melt; there is one large grain of magnesite at the bottom of the capsule. The magnesite grows around two grains of orthopyroxene ~ 100 μm in diameter. A grain of garnet ~ 85 μm size is also present at the bottom of the capsule. When orthopyroxene is added (Figure 2.6b), garnet disappears, orthopyroxene continues to be in equilibrium with the carbonatitic melt, and the amount of magnesite apparently decreases, however this may be because of plucking during the mounting process. At the top of the capsule, two round areas of epoxy on either both sides of the inside capsule wall (Figure 2.6b) indicate the possibility that CO_2 exsolution did occur. However, the melt analyses for G-RS-006 and GO-RS-003 (Table 2.3) show no change in CO_2 content, so those features may be because of the grinding and polishing process.

2.3.1.4 Girnis et al. (C) Experiments:

The starting material C differs from the other starting materials because it contains H_2O as well as CO_2 (Table 2.1). Figure 2.7 shows runs C-RS-001, OPX-RS-001, and OPX-RS-002, of which the first two were run at 6 GPa and 1400ºC for 24 hours each. OPX-RS-002 was run at 4 GPa and 1400ºC for 4 hours. Figure 2.7a shows that without orthopyroxene added, the bulk of the capsule shows the same dendritic carbonatitic melt as the other orthopyroxene runs, differing only in the large magnesite and coesite grains present at the end of the capsule. When orthopyroxene is added at the same pressure and temperature conditions (Figure 2.7b), magnesite and coesite are still present and the added orthopyroxene appears to remains stable with the carbonatitic melt similar to the other experiments. When the pressure decreases from 6 GPa to 4 GPa (Figure 2.7c), magnesite and coesite are no longer present, but orthopyroxene remains stable in the carbonatitic melt. Unlike the other experiments where the orthopyroxene formed a collection of grains averaging around ~20 µm in size, the orthopyroxene in these experiments forms one large grain of orthopyroxene the width of the capsule (~ 1050 µm), which may be related to the presence of H_2O in these experiments.

2.3.2 Composition of phases

2.3.2.1 Melts

The analyses of the melts from the orthopyroxene assimilation experiments are provided in Table 2.3. All the melts were dolomitic with the exception of experiments G-RS-006 and GO-RS-003 which were Ca-bearing magnesitic carbonatite melts. The DP experiments produced the most calcitic melts at with a Ca# (CaO/(MgO + CaO)) between 0.63 – 0.71, the C experiments were almost equal parts CaO and MgO with a $Ca^{\#}$ between 0.51 – 0.52, and the K experiments were slightly more MgO rich, with a $Ca^{\#}$ between 0.42 – 0.47.

In the DP experiments the SiO_2 content is very low, around 2 – 3.5 wt.%, except for DPO-RS-002 where the SiO_2 content jumps up to 18.59 wt.% consistent with orthopyroxene assimilation. The CaO and MgO contents are fairly consistent between all the experiments, hovering around 35 wt.% and 16 wt.% respectively. The Al_2O_3 content stays below 1 wt.%. The CO_2 content for the DP experiments is fairly constant at ~ 43 wt.% except, once again, for DPO-RS-002, where the CO_2 content drops to 29.36 wt.%. The CO_2 concentrations between the rest of non-orthopyroxene and orthopyroxene experiments stay relatively the same. The K experiments are higher in SiO_2 content than the DP experiments at ~ 6 wt.% and are more MgO rich and CaO poor, but have a similar CO_2 content. The CO_2 content decreases to ~33-36 wt.% for the G experiments, which were also more SiO_2 rich than the previous two experiments (~ 13 - 14 wt.% SiO_2). These experiments also continue to the trend of becoming more MgO rich reaching concentrations of 41.46 wt.% and CaO poor reaching concentrations as low as 6.72 wt.%. The water-bearing experiments C have a SiO_2 content ranging between 7.74 and 16.10 wt.%, equal amounts of MgO and CaO at ~ 22 wt.% and 23 wt.% respectively, and have a CO_2 content of 33 – 40 wt.%. Comparing each non-orthopyroxene/orthopyroxene experiment pair, it is evident that only DP experiments run at 2.5 GPa show a significant change in CO_2 and SiO_2 content; the other exception being the SiO_2 content for the C composition experiments. The increase of SiO_2 in the C orthopyroxene-bearing experiments can be explained by the destabilization of coesite that appears in the orthopyroxene-free experiment in the subsequent orthopyroxene-bearing experiments because of the presence of orthopyroxene and the lower run pressure of 4 GPa in the OPX-RS-002 experiment. For all the other experiments the compositions are similar.

2.3.2.2 Silicates

The orthopyroxene, olivine, garnet, clinopyroxene, and coesite analyses from all the orthopyroxene assimilation experiments are listed in Tables 2.4 - 2.8. The orthopyroxenes (Table 2.4) in the experiments are almost pure enstatite, but they have reacted with the melts, because they contain 0.23 – 1.15 wt.% CaO and 0.21 to 1.64 wt.% Al_2O_3. Like the orthopyroxene, the olivines (Table 2.5) present in the experiments are nearly pure end-member forsterite, but contains 0.08 – 0.55 wt.% CaO and 0.04 - 0.20 wt.% Al_2O_3. The garnet (Table 2.6) is Ca-bearing pyrope with between 1.93 – 4.45 wt.% CaO and 26.21 – 29.81 wt.% MgO. DPO-RS-002 is the only experiment that contains clinopyroxene (Table 2.7), with sub equal amounts of CaO and MgO and 0.57 wt.% Al_2O_3. Experiments C-RS-001 and OPX-RS-001 both hosted a few grains of coesite (Table 2.8) which was nearly pure.

2.3.2.3 Non-silicates

The experiments also formed a number of non-silicates, including magnesite, spinel, periclase, and dolomite (Table 2.9 – 2.12). The magnesite (Table 2.9) formed in experiments K, G, and C all contain CaO between 0.96 and 3.62 wt.%. The spinel (Table 2.10) contains 0.40 – 1.31 wt.% SiO_2 and 0.15 and 0.27 wt.% CaO (most likely an effect from the surrounding carbonatite), respectively. Experiment DP-RS-005 was the only experiment to contain periclase (Table 2.11) and also had a large dolomite inclusion hosted in a forsterite grain the analysis of which is shown in Table 2.12. The dolomite inclusion leans towards a more calcitic composition with a $Ca^{\#}$ value of 0.61

and includes 1.06 wt.% SiO_2 suggesting that it may be trapped carbonatitic melt rather than crystalline dolomite.

2.4. Discussion

2.4.1 Orthopyroxene Interaction with Carbonatitic Melts

These experiments have shown that at a pressure of 2.5 GPa orthopyroxene is unstable in a carbonatitic melt and completely assimilates forming forsterite and diopside, causing CO_2 exsolution during the process. This is similar to the Russell et al. (2012) model, however the presence of diopside rules out activity of silica being the cause for orthopyroxene instability. If the orthopyroxene assimilation were controlled by the activity of silica, the orthopyroxene should have only formed forsterite and CO_2 as discussed by Luth (2009). Instead, the presence of diopside suggests that the instability of orthopyroxene is controlled by a decarbonation reaction of the form enstatite + melt → forsterite + diopside + CO_2 shown in Figure 2.8. The conditions of the experiment relative to the extrapolated reaction line in P/T space are shown and it is evident that this reaction would commence at a pressure of 2.5 GPa at the same temperature conditions of these experiments at 1450ºC.

In order to directly compare the melts between the non-orthopyroxene-bearing and orthopyroxene-bearing experiments to determine whether any orthopyroxene had been assimilated, each melt composition was recalculated to include any other silicates or non-silicates; excluding orthopyroxene in the case of the orthopyroxene-bearing experiments. This should result in the non-orthopyroxene bearing experiment melts having a composition close to that of the starting material, and if no orthopyroxene assimilation has occurred, the same should hold for the orthopyroxene-bearing experiments as well. The two corresponding melts were then compared using a paired student t-test to see if the analyses were significantly different. Each experiment was also compared to the starting material composition to ensure that no leaking had occurred. The table showing the calculations for the modified melts can be found in Appendix 2 and the t-tests run on each pair of analyses and the comparison between the experiments and the starting materials can be found in Appendix 3. The compositions of the modified melts and the results of the t-tests are summarized in Table 2.13 and Table 2.14. Each pair of experiments is colour coded depending on whether the test showed that the null hypothesis (which was that the two analyses were equal) was not rejected (white), was rejected but yielded a t value less than 2t* (light grey), or was rejected with a value greater than 2t* (grey). For the paired DP experiments at 2.5 GPa SiO_2, Al_2O_3, and CO_2 all were rejected with t values greater that 2t*. MgO and CaO were not rejected, however, and therefore can be interpreted as unchanging values between the two experiments. Therefore the reaction occurring in the orthopyroxene experiment causes CO_2 exsolution and an increase in SiO_2 content, but does not also cause MgO enrichment as previously thought.

Figure 2.9 and Figure 2.10 shows the compositions of the DP starting material, the orthopyroxene-doped DPO-RS-002 experiment melt and bulk composition, and a range of parental kimberlite compositions (Harris et al., 2004; Kjarsgaard et al., 2009; Kopylova et al., 2007; Le Roex et al., 2003; Price et al., 2000; Russell et al., 2012). The dashed arrow on both diagrams shows the evolution of the melt from DPO-RS-002, where orthopyroxene assimilation occurred and the solid line shows the evolution of the bulk composition of DPO-RS-002. The melt evolves towards the field of parental kimberlite compositions, but not enough CO_2 exsolution occurs to evolve the bulk compositions of experiment DPO-RS-002 to kimberlitic compositions. Figure 2.10 shows that the melt evolves away from parental kimberlite compositions in $Ca^{\#}$. This trend is caused by the crystallization of both forsterite and diopside which removes more MgO from the melt than that is being added by orthopyroxene assimilation. However the overall bulk composition of DPO-RS-002 does evolve into the field of parental kimberlite compositions.

At pressure/temperature conditions above the decarbonation reaction, as documented in the other experiments presented in the results section, it is evident that no orthopyroxene assimilation occurs at high pressure and in consequence, no CO_2 exsolution occurs. In fact, the electron microprobe analyses of the orthopyroxene show that the pure synthetic enstatite added to each experiment has interacted with the carbonatitic melt modifying its composition to incorporate CaO and Al_2O_3 (up to 1.52 wt.% CaO and 1.64 wt.% Al_2O_3 respectively), suggesting that the orthopyroxene is in equilibrium with the carbonatitic melt despite low concentration of SiO_2 in the melt.

These experiments demonstrate that these melts do not have to evolve far, or at all, to reach orthopyroxene saturation suggesting that low activity of silica is not what is causing orthopyroxene instability in the melt. It is instead controlled by lower pressure decarbonation reactions where enstatite is a participant. The absence of orthopyroxene from the kimberlitic xenocryst assemblage therefore can be explained by the decarbonation reaction the kimberlite intersects during ascent and the resulting CO_2 exsolution provides a rapid ascent mechanism for the kimberlite from a depth of ~ 150 km.

2.4.2 A Comparison with Other Orthopyroxene Assimilation Experiments from the Literature

After the publication of the Russell et al. (2012) paper, other researchers have investigated orthopyroxene interactions with carbonatitic melts just as this study has. Safonov gave a presentation at the General Meeting of IMA in South Africa in 2014 showing his orthopyroxene assimilation experiments run at 2 GPa and temperatures between 1000 and 1200ºC using the same Na_2CO_3 starting material as used in the Russell et al. (2012) experiments. Their experiments with an 80:20 ratio of Na_2CO_3 to orthopyroxene showed the orthopyroxene reacted with the melt to produce a Na-Mg carbonate melt at 1000ºC as well as forsterite and a Na-Mg silicate (NMS):

$$5\,Mg_2Si_2O_{6_{(en)}} + Na_2CO_{3_{(melt)}} \rightarrow$$

$$\tfrac{1}{2}Na_2Mg(CO_3)_{2_{(melt)}} + \tfrac{5}{4}\,Mg_2SiO_{6_{(fo)}} + \tfrac{1}{4}\,Na_4Mg_8Si_{15}O_{40_{(NMS)}} \qquad (2)$$

but did not result in CO_2 exsolution. As the temperature of the experiments was increased, the NMS started melting to produce an immiscible silicate-carbonate melt alongside the carbonate melt. As the temperature continued to increase the amount of silicate-carbonate melt increased as well. The carbonate melt was still present as globules within the silicate-carbonate glass. The change in composition of the silicate-carbonate melts from the 1000ºC experiment and the 1200ºC was reported to be negligible and no CO_2 exsolution occurred. Instead CO_2 content increased by 2 wt.% with decreasing temperature.

More recently, Kamenetsky and Yaxley (2015) reported on the assimilation of olivine, orthopyroxene, and clinopyroxene with Na_2CO_3 melts and $CaCO_3$-Na_2CO_3 melts at pressures between 2 – 5 GPa and temperatures of 1000 – 1200ºC. Their experiment at 2 GPa and 1000ºC produced a carbonate melt, a silicate melt, olivine, and krinovite ($NaMg_2CrSi_3O_{10}$); a different outcome than the experiment done by Safonov at the same pressure and temperature conditions (Kamenetsky and Yaxley, 2015). This is because the orthopyroxene used in the experiments was natural orthopyroxene from San Carlos, changing the experiments from a simple MgO-Na_2O-CO_2 system to a complex system including major and minor oxides such as TiO_2, Al_2O_3, MnO, FeO, Cr_2O_3, etc. As the temperature and pressure increased, the two immiscible liquids mixed to form one homogeneous silicate-carbonate melt accompanied by aggregates of acicular skeletal Na-Mg silicates and carbonates (see Figure 1a in Kamenetsky and Yaxley, 2015). One experiment of interest at 2 GPa and 1000ºC used a different carbonatitic starting material that was a 1:1 mixture of $CaCO_3$ and Na_2CO_3. The addition of $CaCO_3$ resulted in the experiment no longer producing two immiscible melts, and instead contains a single silicate-carbonate melt with a dendritic quench texture very similar to the quench textures presented in this thesis. Instead of olivine and krinovite forming, diopside forms and the orthopyroxene does not completely assimilate into the melt as it did in all the other experiments. Here it remains as relic grains surrounded by diopside rims (see Figure 2d in Kamenetsky and Yaxley, 2015). As in the Safonov experiments, at no point does CO_2 exsolution occur because of orthopyroxene reaction with the melt.

Both these studies show that unlike the case with the Russell et al. (2012) experiments, orthopyroxene dissolution at the higher pressure and temperature conditions relevant to the shallow upper mantle does not lead to the CO_2 exsolution that was proposed to drive the ascent of a kimberlite. Kamenetsky et al. (2015) used their experiments to instead suggest a new mechanism for CO_2 exsolution via orthopyroxene assimilation in which the immiscible silicate liquid formed by the reacting orthopyroxene and the Na_2CO_3 becomes saturated with CO_2 as the carbonatite ascends and begins to continuously release CO_2. However, their own more complex experiment using a 2:2:1 CaO-Na_2CO_3-Opx starting material undermines this model of kimberlite ascent, because the silicate and carbonate components of the melt are no longer immiscible. The experiment also shows that the addition of CaO increases the stability of orthopyroxene.

Comparing the results from these papers to the experiments in the present study, it becomes clear that it is important to use an appropriate system to study primary kimberlitic melts. The reason why Safanov, Kamenetsky et al. (2015), and Russell et al. (2012) used Na_2CO_3 as a proxy was because it has a lower melting point than dolomitic carbonatites whose high melting temperatures are considered unrealistic for the formation of kimberlites (Kamenetsky and Yaxley, 2015). It also has been shown that sodic dolomitic carbonatitic melts can be produced at a range of mantle conditions (Dasgupta et al., 2004; Litasov et al., 2013; Wallace and Green, 1988). However, when looking at the compositions of the melts produced in carbonatite – peridotite equilibrium experiments, Na_2O concentrations average around 3 - 4 wt.%, reaching at maximum concentration of 21 wt.% (Yaxley and Green, 1996), which is substantially lower than the concentration of Na_2O in a pure Na_2CO_3 melt (58.5 wt.%). By using a melt in a system devoid of important components such as SiO_2, MgO, and CaO, Safonov and Kamenetsky and Yaxley (2015) may have oversimplified the system too much, and potentially missed important reactions. Use of Na_2CO_3 carbonatitic melts in future work should be avoided, but the importance of the impact that Na_2O has on carbonatitic melts should not be underestimated, and should be an essential component in any future carbonatitic melt experiments.

2.4.3 Orthopyroxene Assimilation and Diopside Crystallization

A part of our model for orthopyroxene assimilation that needs to be addressed is the formation of diopside that accompanies the formation of olivine and CO_2. Diopside is not a part of the observed kimberlite phenocryst assemblage, so if this decarbonation reaction is indeed how orthopyroxene assimilation occurs, then there must be a later process that causes the disappearance of the diopside.

As it did with orthopyroxene assimilation, the answer may lie with decarbonation reactions. Using Thermocalc 3.36 (Powell and Holland, 1988) to run a Schreinemakers' analysis for the CMS + CO_2 system at pressures between 0.05 to 20 GPa and temperatures between 50 – 2000ºC, it is evident that one other reaction occurs at a lower pressure than the enstatite-dolomite decarbonation reaction. In the absence of enstatite, diopside reacts with dolomite to form forsterite, calcite, and CO_2 (Figure 2.11).

In our model, the diopside would need to react with a dolomitic melt instead of crystalline dolomite. In order to see if the reaction $\mathrm{dol_{melt}} + \mathrm{di} \rightarrow \mathrm{fo} + \mathrm{cc} + CO_2$ was theoretically plausible, the program CSpace was used to generate mass balance equations for systems involving enstatite, diopside, forsterite, dolomite, calcite, CO_2, and a range of dolomitic liquids. Figure 2.12 shows the resulting Schreinemakers' analysis for two invariant points. This reaction has been also proposed by others and has been previously used to explain why dolomitic carbonatites can evolve to calcitic carbonatites (Harmer and Gittins, 1997; Wyllie and Huang, 1976). This reaction can also be shown to take place at a lower pressure than orthopyroxene assimilation reaction by doing separate Schreinemakers' analyses for two invariant points, one where calcite is absent and another where enstatite is absent (Figure 2.12) using the CMS + CO_2 system where forsterite, diopside, CO_2, melt with the same composition as listed above, and dolomite are also present. The analyses then can be joined by their respective enstatite and calcite absent reactions, placing the orthopyroxene assimilation pressure at a higher pressure than the diopside assimilation reaction as required by the Thermocalc calculation. The diopside assimilation reaction can only happen if the melt has a composition on the opposite side of diopside on the forsterite, calcite, and CO_2 plane (Figure 2.13). In other words, once the melt becomes too SiO_2 rich, this reaction will stop and no more diopside will be assimilated.

Since the dolomitic melt should be present in excess, the reaction would end up resorbing all the diopside formed in the previous reaction, explaining why no phenocrystic diopside is observed at the surface. The production of CO_2 would provide a second burst of volatile exsolution to further drive the rapid ascent of the kimberlite to the surface. The formation of calcite at the expense of dolomite would explain why these carbonatites that are originally dolomitic in composition eventually evolve towards a more calcitic composition, thereby explaining the crystallization of primary calcite as a groundmass mineral (Mitchell, 2008). Finally, once the melt becomes too rich in SiO_2 the diopside assimilating reaction will stop, explaining why some xenocrystic diopside is preserved. Exploring the dissolution of diopside in transitional silicate carbonate melts at pressures below the decarbonation reaction could help support this theory and provide more insight on how kimberlites evolve and ascend through the lithosphere.

2.4.4 Carbonatite versus Kimberlite Formation

If primary kimberlitic melts are originally carbonatitic and evolve to parental kimberlite compositions through interaction with the mantle during ascent, then the question of why not all carbonatites become kimberlites needs to be addressed. Based on their model of orthopyroxene assimilation because of the instability of the mineral in low silica melts, Russell et al. (2012) suggested that carbonatites remain carbonatites when they move through orthopyroxene-poor lithosphere and therefore do not assimilate orthopyroxene to start the evolution to a kimberlite. Another possibility they propose is that the carbonatite is formed at a shallow depth and therefore the melt travels through only a thin layer of orthopyroxene-bearing lithosphere resulting in only a small amount of orthopyroxene assimilation insufficient to evolve to kimberlite.

In our model, orthopyroxene assimilation begins at a specific depth corresponding to a pressure of approximately 2.5 GPa, with clinopyroxene assimilation potentially following at lower pressure. If a carbonatitic melt is formed at pressure lower than the orthopyroxene assimilation reaction it is possible that the melt will not evolve enough to reach kimberlitic compositions or form enough CO_2 to fuel rapid ascent. If the layer between 2.5 GPa to the depth where diopside assimilation begins is orthopyroxene poor, then it is possible that that would also cause the carbonatite to remain a carbonatite. In Chapter 3, it is shown that a range of carbonatitic and transitional melts can evolve to kimberlitic compositions depending on the amount of mantle material assimilated. Transitional melts that are more silica rich would require less mantle contamination than a carbonatite. Therefore the composition of the initial melt in combination with the initial pressure of formation relative to the assimilation reactions would affect whether a kimberlite or a carbonatite is formed.

2.4.5 Comparing Experimental Pressure and Temperature Conditions to Mantle and Plume Adiabats

As was mentioned briefly in one of the previous sections, the temperatures in these experiments are very high and therefore warrant further investigation on why the experimental temperatures may be elevated and whether the temperatures in these experiments are realistic for an ascending kimberlitic melt. Figure 2.14 shows the pressure and temperature conditions of each assimilation experiment as well as the conditions where the corresponding starting materials were formed relative to potential mantle adiabat temperatures modeled by Stixrude and Lithgow-Bertelloni (2007) and a range of plume adiabat temperatures (Ghosh et al., 2014). The pressure and temperature conditions for the DP and C starting materials and the C orthopyroxene assimilation experiments lie to the right of the mantle adiabat, suggesting that they could realistically form under normal mantle conditions. The rest of the starting materials and orthopyroxene experiments lie on the right of the mantle adiabat but left of the plume adiabat suggesting that under special conditions, such as elevated temperatures caused by a nearby rising plume, these melts could from and produce kimberlites.

A reason why some of these experiments are at elevated temperatures could be in part because of the simplified system used. The system CMAS + CO_2 excludes a number of components that have been shown to lower the solidus of both carbonated peridotites and carbonatites. Na_2O, as mentioned previously, has been shown through a number of experimental studies to depress the solidus of carbonated mantle silicates by as much as 400 - 500ºC when present in amounts as small as a few weight percent (Litasov and Ohtani, 2009; Litasov et al., 2013). FeO, more specifically a lower Mg# $\left(\frac{\text{MgO}}{\text{MgO+FeO}^*}\right)$, can also lower the solidus temperature, but not to the same degree as Na_2O (Hirschmann, 2000). Though FeO is a fairly major component in kimberlites, at concentrations between ~ 5.5 – 9 wt.% (Kjarsgaard et al., 2009; Price et al., 2000), it presents challenges in experimental studies because of Fe loss to Pt capsules during the experiment. Finally volatiles, such as CO_2 and H_2O, also have a significant effect on the solidus of carbonated peridotite (Eggler, 1978; Eggler and Wendlandt, 1979b; Kushiro, 1970).

All the orthopyroxene experiments, with exception of the C starting material experiments which had H_2O as well, were in the CMAS + CO_2 system and therefore did not have FeO, Na_2O, or H_2O to decrease the melting temperature of the carbonatite used. This observation applies to the starting materials K and DP as well. The original experimental composition which led to the formation of the G starting material melt had in addition to CMAS + CO_2: Na_2O at 0.5 wt.% and FeO* at 7.60 wt.% (Girnis et al., 2011), however the pressure and temperature conditions at which that composition forms melt does not fall within the region of a mantle adiabat. It is possible that the addition of H_2O could push the solidus for this bulk composition to more reasonable P/T conditions. The C starting material is an example of an experiment that uses all of these solidus depressing oxides and that they then fall within normal mantle pressure conditions. Future experiments studying orthopyroxene assimilation in carbonatitic melts should try to incorporate these more complex systems in order to more accurately simulate the pressure and temperature conditions at which these processes actually take place.

2.4.6 Obstacles in Analyzing Carbonatitic Melts

Looking back at Figure 2.14, it is evident that all of the orthopyroxene assimilation experiments required high temperatures either close to or above their high pressure/temperature counterparts to produce experiments consisting almost solely of carbonatitic melt. This should not typically be the case. A carbonatitic melt in equilibrium with carbonated peridotite should still be melt when the peridotite is removed at the same mantle conditions and continue to be a melt at lower pressures. Instead all the experiments had other minerals in crystalline form accompanying the melt. This brings into question where the carbonatitic liquidus lies in P/T space with respect to these experiments and whether the liquidus has a negative dP/dT slope in P-T space, so that it curves out at lower pressure to higher temperatures resulting in sub-liquidus assemblages.

Initial DP experiments were run at lower pressure but the same temperature conditions as the original starting material, and therefore should have been completely melt, were instead completely crystalline. Each starting material was rechecked against the literature to ensure the compositions were not incorrectly measured but no errors were made. Therefore a discrepancy must lie in the compositions of the starting materials cited in the literature. To test this theory, we copied a carbonated peridotite partial melting experiment that formed a starting composition that was initially used for some of our preliminary experiments, which was a carbonatitic melt in equilibrium with carbonated peridotite at 6.9 GPa and 1460ºC (Gudfinnsson and Presnall, 2005). The compositions of the carbonated peridotite starting material, the carbonatitic melt produced that Gudfinnsson and Presnall (2005) reported, and the carbonatitic melt that we measured from the recreated experiment are listed in Table 2.15 and the backscatter electron image of the experiment is shown in Figure 2.15. The compositions of the two carbonatites (JD-RS-003) which was our experiment and PR-106 which was the melt analyzed by Gudfinnsson and Presnall (2005) were the same according to the paired student t-test with the exception of MgO.

We then took the composition of the melt analyzed in our experiment, made a second starting material and ran it at the same pressure/temperature conditions as the first experiment (MJD-RS-001). This should have produced a run that was completely carbonatitic melt, however the experiment contained carbonatitic melt, forsterite, and diopside (Figure 2.16a). The melt produced in this experiment was analyzed (Table 2.15), and used to make a third starting material which was once again run at the same pressure and temperature conditions as the first two experiments. This experiment resulted in a carbonatitic melt hosting only a few grains of Ca-bearing pyrope (Figure 2.16b). The composition of each subsequent melt became more MgO and SiO_2 poor and CaO rich. T-tests between JD-RS-003, MJD-RS-001, and MMJD-RS-001 show that MJD-RS-001 and MMJD-RS-001 are nearly identical in composition except for CaO and that MJD-RS-001 and JD-RS-003 are similar except in their MgO and CaO values. JD-RS-003 and MMJD-RS-001 are different melts, only sharing statistically equal Al_2O_3 and CO_2 concentrations.

These experiments and the difficulties we have had with producing carbonatitic melts from the analyses published by other experimental petrologists suggests that there is a common error that we are all making when analyzing carbonatitic melts. Techniques have been introduced in order to improve the accuracy of carbonatitic melt analyses such as the modified iterative sandwich experiment (MISE) technique (Dasgupta and Hirschmann, 2007), but can be very time consuming since they require at least four additional experiments to reach the correct composition.

One possibility why these melts are not reproducible is that petrologists are underestimating the amount of CO_2 in the melt. Many of the dendritic textures reported in the literature and in our experiments show holes or gaps that could be from CO_2 exsolution during quenching. This extra CO_2 is therefore not accounted for during analysis. This could be corrected for by adding CO_2 as an additional phase and recalculating a new melt composition by forcing the bulk composition of the experiment to be equal to the original starting material composition. When we apply this recalculation to our melts the amount of CO_2 in the melt increases by up to 5wt.%, which can lower the solidus temperature carbonated peridotite and other melts by 100ºC (Ghosh et al., 2014). Further work exploring underestimations of CO_2 contents could lead to a faster way to recalculate data and deliver more accurate carbonatite analyses.

2.5 Conclusion

Our orthopyroxene experiments show that the assimilation of orthopyroxene is controlled by a decarbonation reaction at a pressure of approximately 2.5 GPa. This reaction explains the absence of orthopyroxene in the xenocryst assemblage and also results in the exsolution of CO_2 that could drive rapid ascent and the formation of diopside. A Schreinemakers' analysis of the CMS + CO_2 system shows that a second lower-pressure decarbonation reaction that would result in the complete assimilation of the diopside formed in the previous reaction causing more CO_2 exsolution and causing the melt to evolve from a dolomitic to a more calcitic composition explaining why calcite, not dolomite, is the main carbonate found in the groundmass of kimberlites. At higher pressures no orthopyroxene assimilation occurs, showing that activity of silica does not have an influence on orthopyroxene assimilation as Russell et al. (2012) suggested. Future work on these potential primary kimberlitic melts should focus on more complex systems involving CaO, MgO, SiO_2, Al_2O_3, Na_2O, FeO, CO_2, and H_2O.

Chapter 2 Figures:

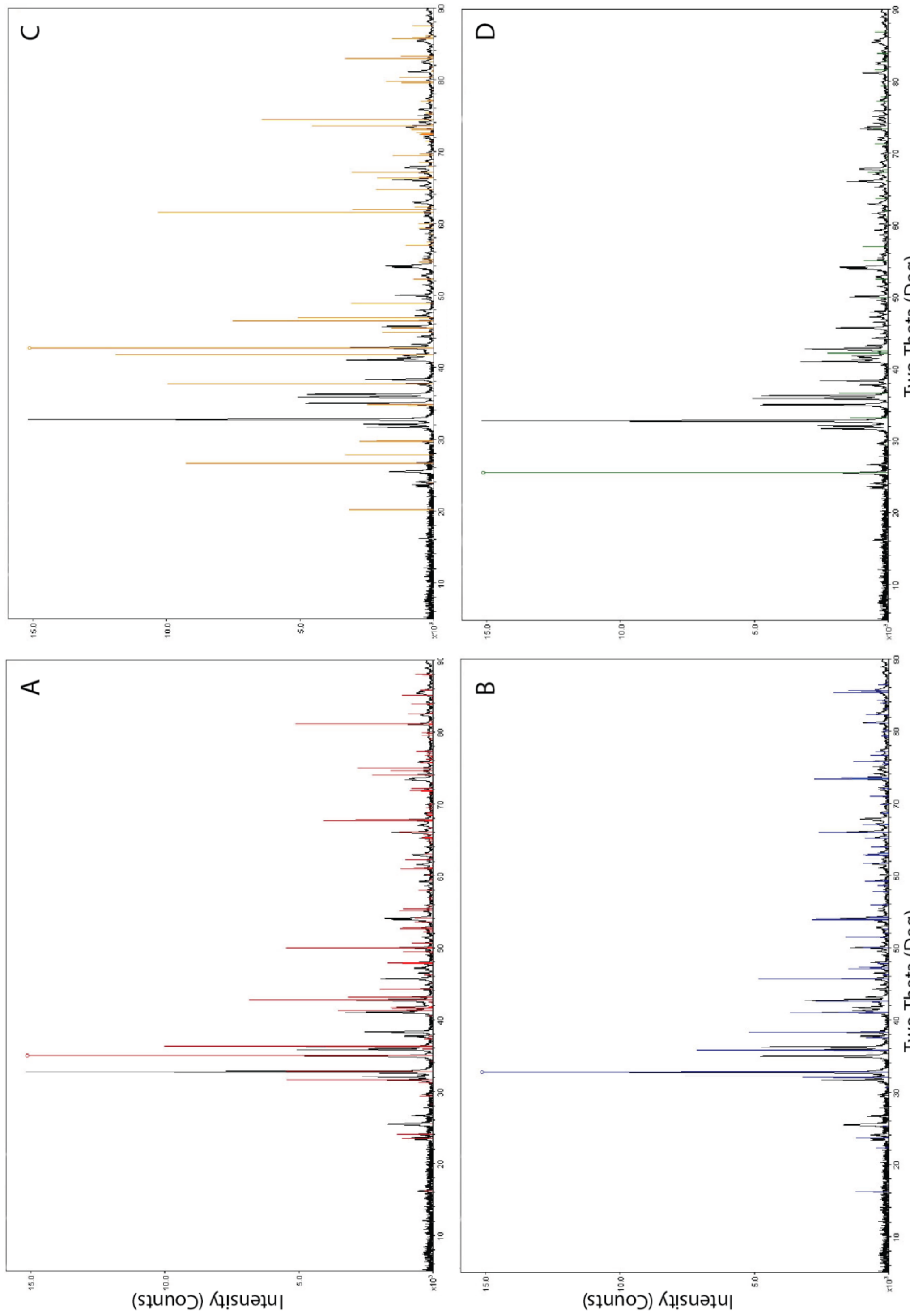

Figure 2.1: The XRD spectra of the synthesized enstatite. A = Clinoenstatite, B = Protoenstatite, C = Forsterite, and D = Cristobalite.

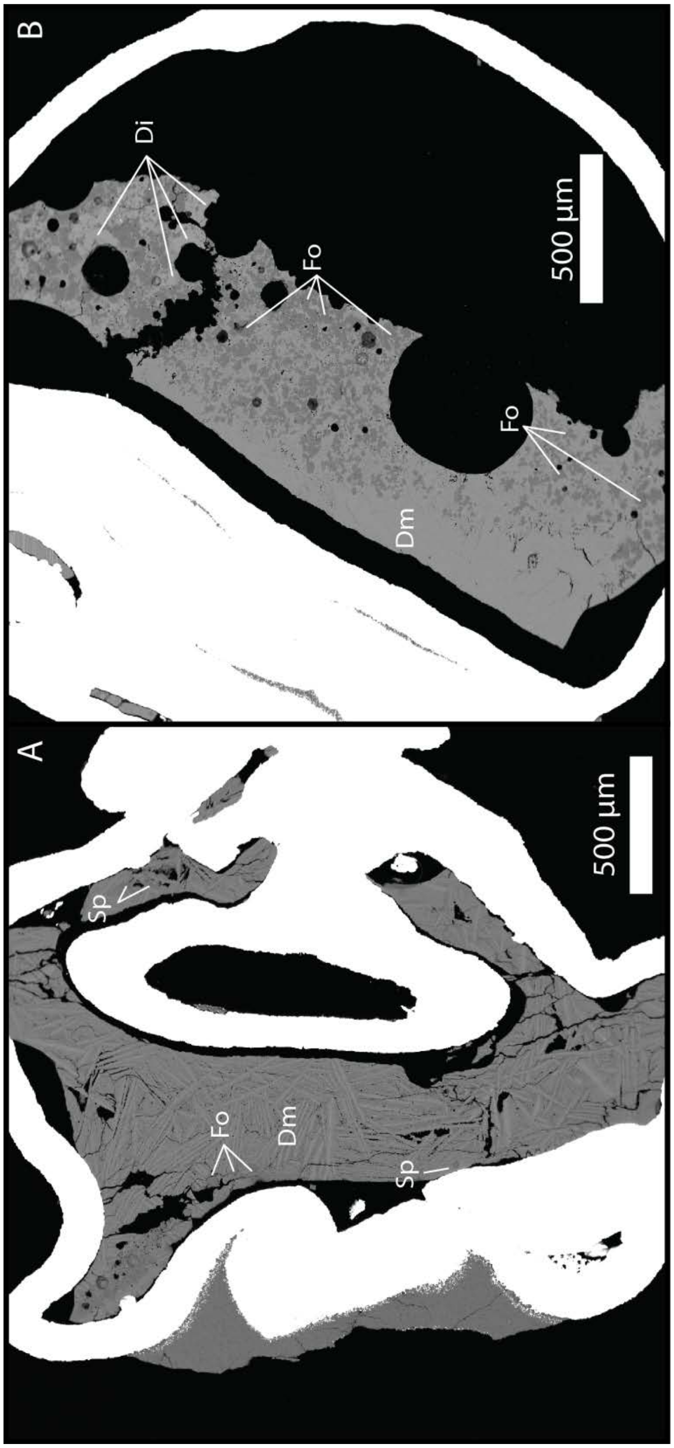

Figure 2.2: Backscatter election images (BSE) of run PC-DP-RS-001 (A) and DPO-RS-002 (B) run at 2.5 GPa and 1450ºC. Fo = forsterite, Sp = spinel, and Dm = dolomitic melt. Dark grey is epoxy.

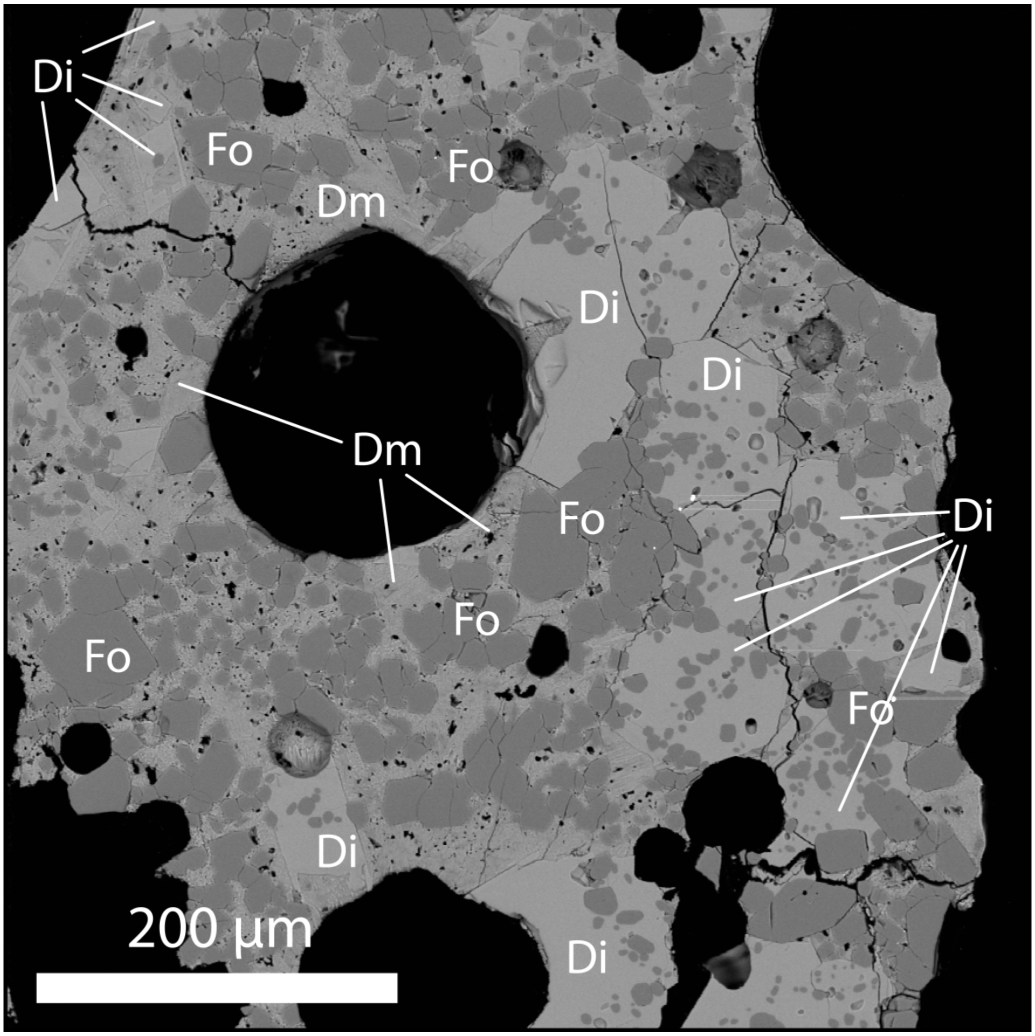

Figure 2.3: A BSE from DPO-RS-002 showing diopside oikocrysts hosting forsterite chadocrysts. The diopside grains are euhedral and in some cases also show a skeletal texture. There is still melt present in this area of the capsule, but is not as abundant here. Di = diopside.

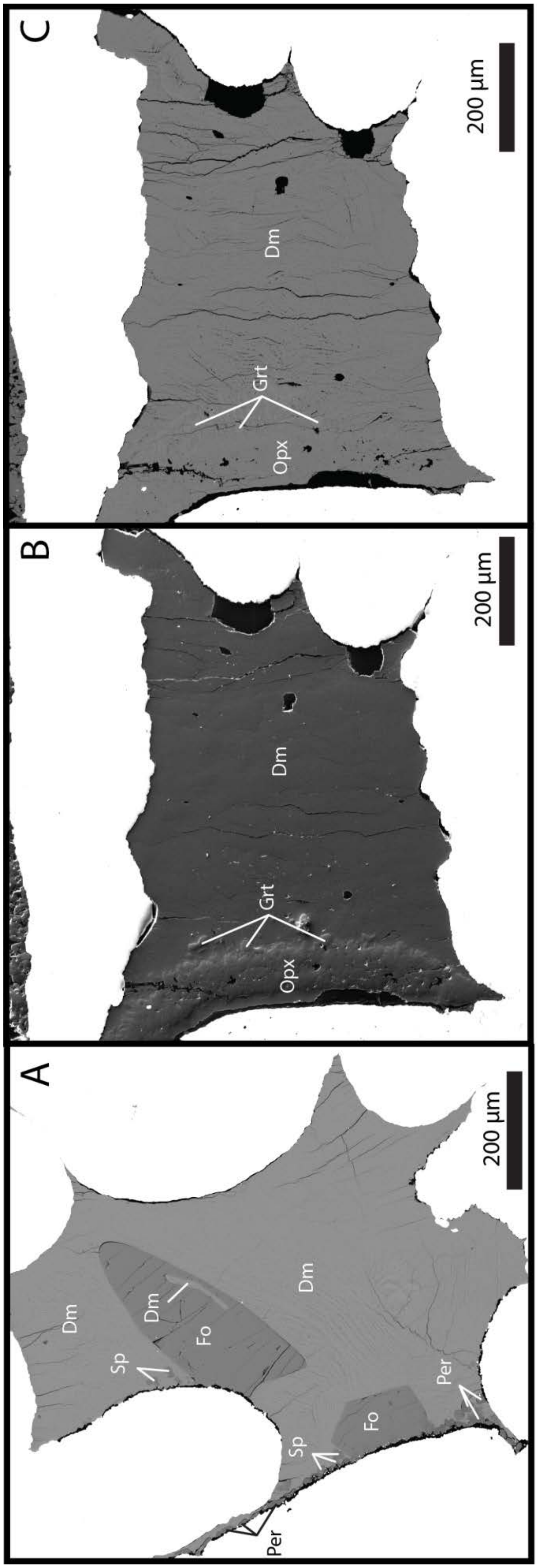

Figure 2.4: A BSE from run DP-RS-005 (A) and a secondary electron (B) /backscatter image (C) pair from run DPO-RS-004. Run at 4.5 GPa and 1500ºC. Per = periclase, Opx = orthopyroxene, and Grt = garnet.

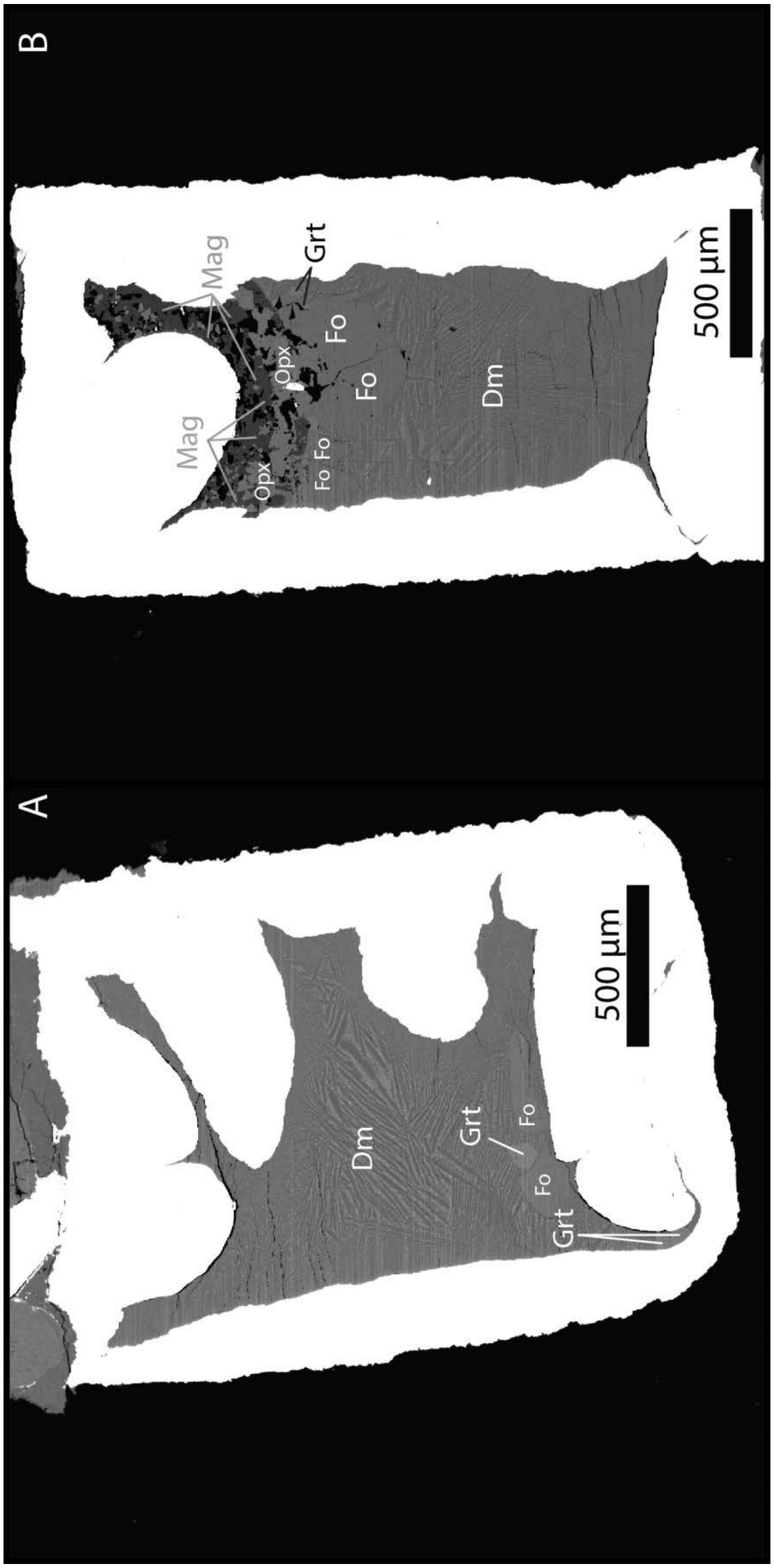

Figure 2.5: BSEs from runs K-RS-003 (A) and KO-RS-001 (B). Mag = magnesite. Run at 4.5 GPa and 1600ºC.

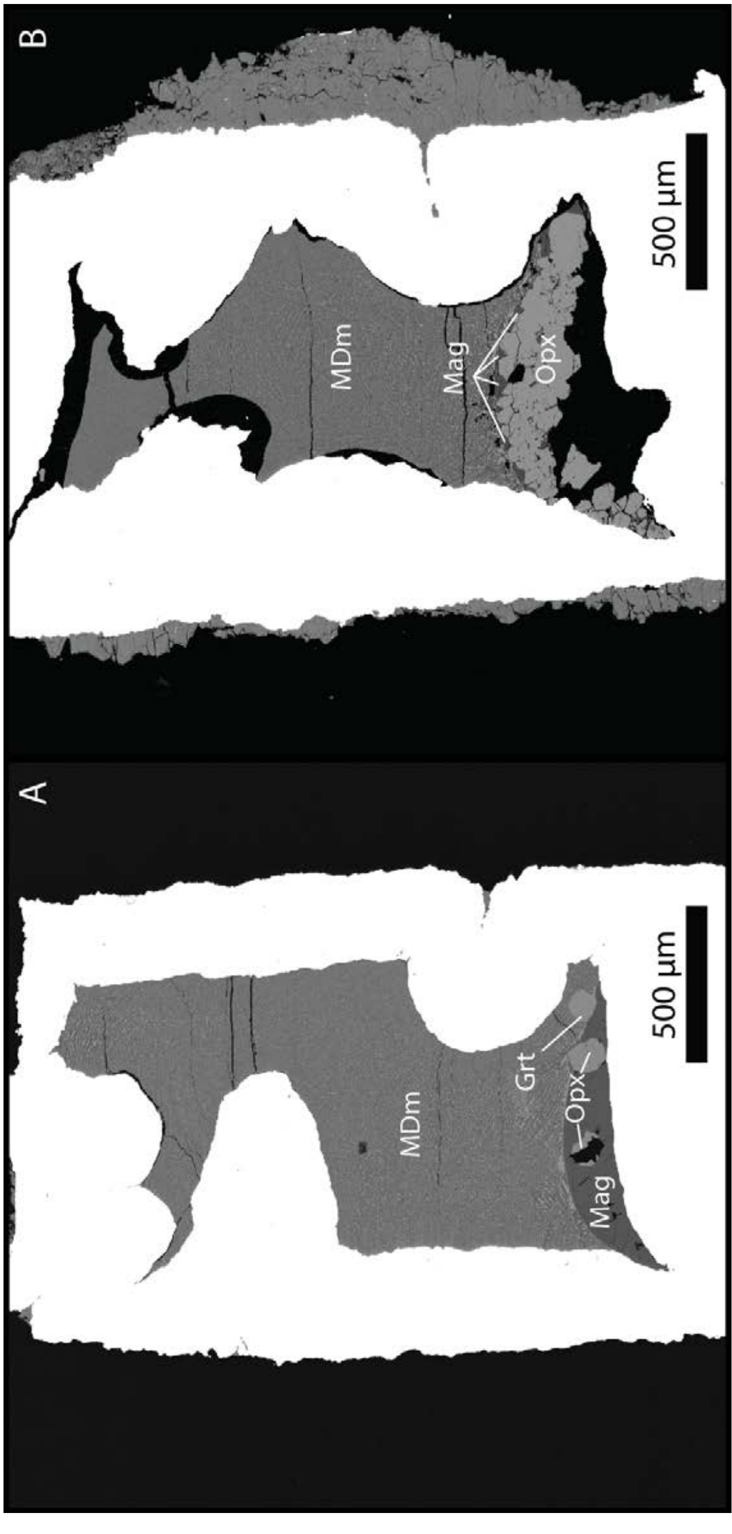

Figure 2.6: BSEs from runs G-RS-006 (A) and GO-RS-003 (B). Run at 4.5 GPa and 1650ºC. MDm = magnesitic dolomitic melt. Plucking is evident at the bottom of slide B.

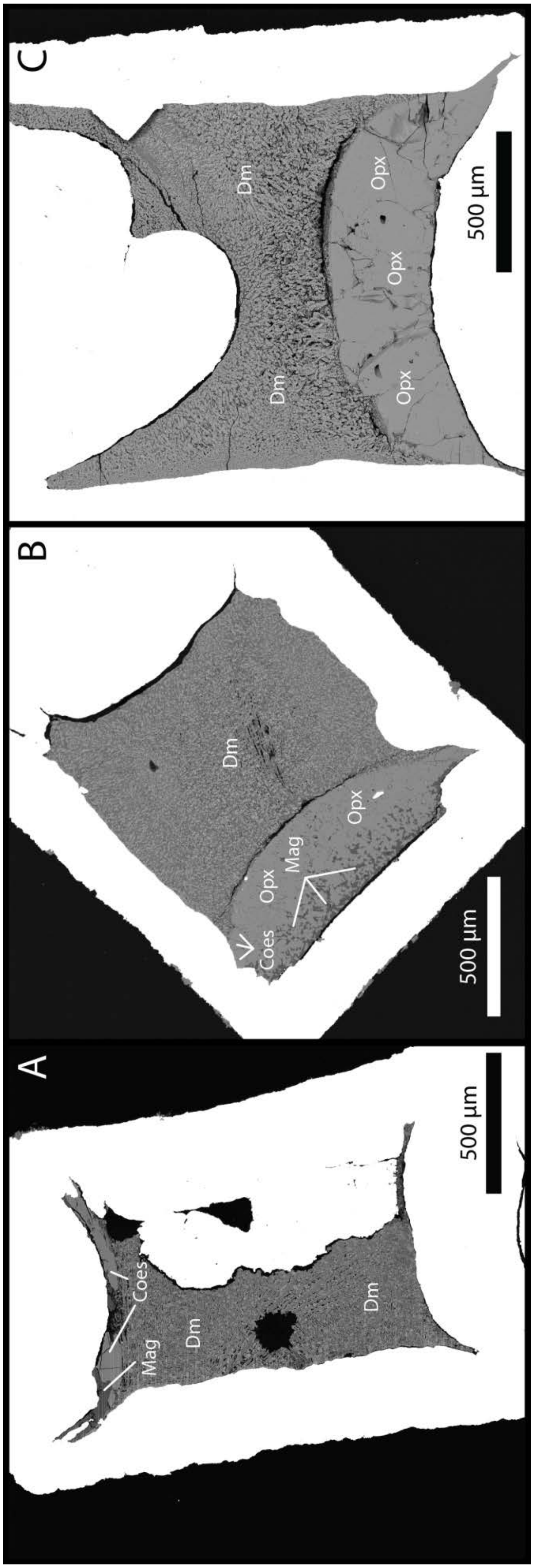

Figure 2.7: BSEs from runs C-RS-001 (A), OPX-RS-001 (B), and OPX-RS-002 (C). C-RS-001 and OPX-RS-001 were run at 6 GPa and 1400ºC. OPX-RS-002 was run at the same temperature but a pressure of 4 GPa. Coes = coesite.

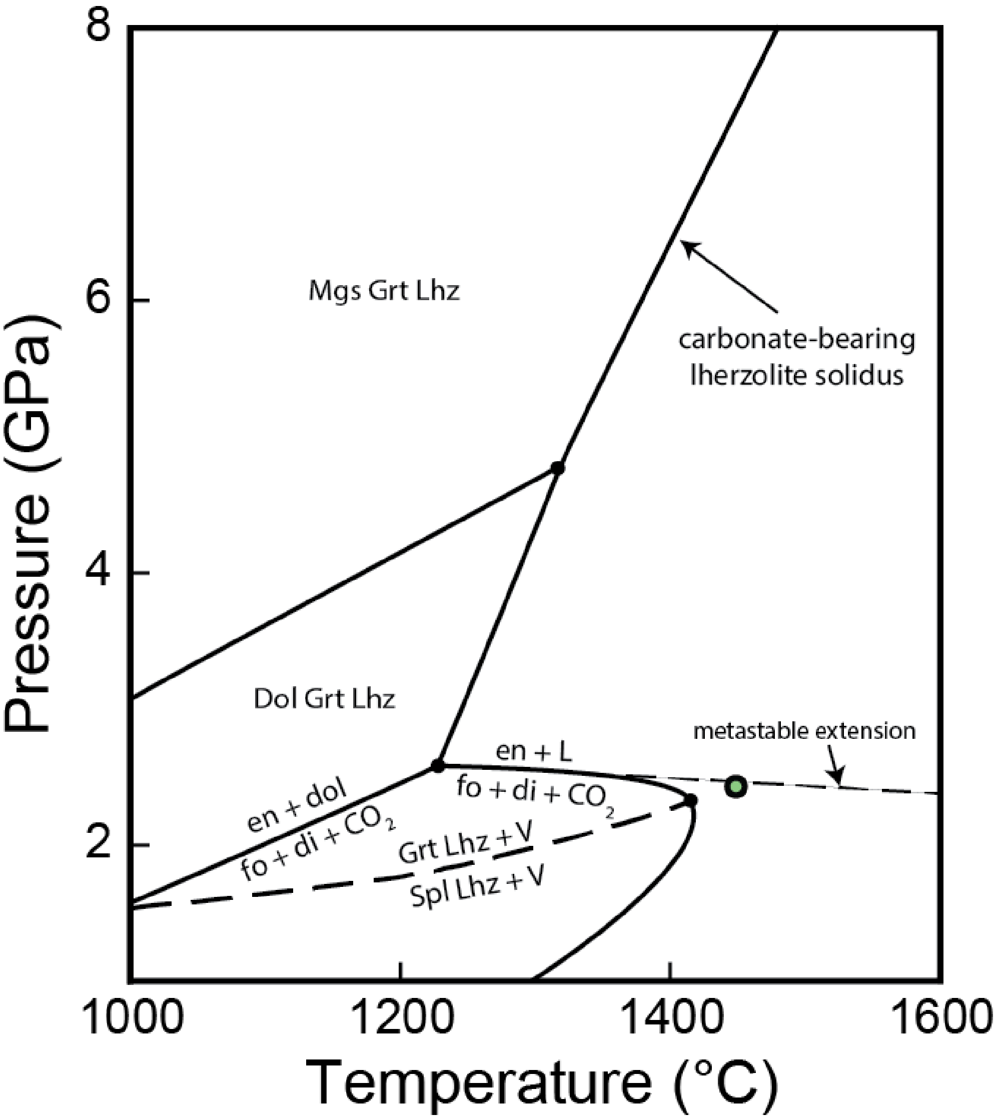

Figure 2.8: A pressure-temperature phase diagram showing the solidus for carbonated peridotite in CMAS + CO_2 system (Dalton and Presnall, 1998a), the stability fields for magnesite garnet, dolomite garnet, garnet, and spinel lherzolite, and the decarbonation reaction en + L = fo + di + CO_2. The green circle shows the pressure temperatures conditions of experiment DPO-RS-002 relative to the decarbonation reaction.

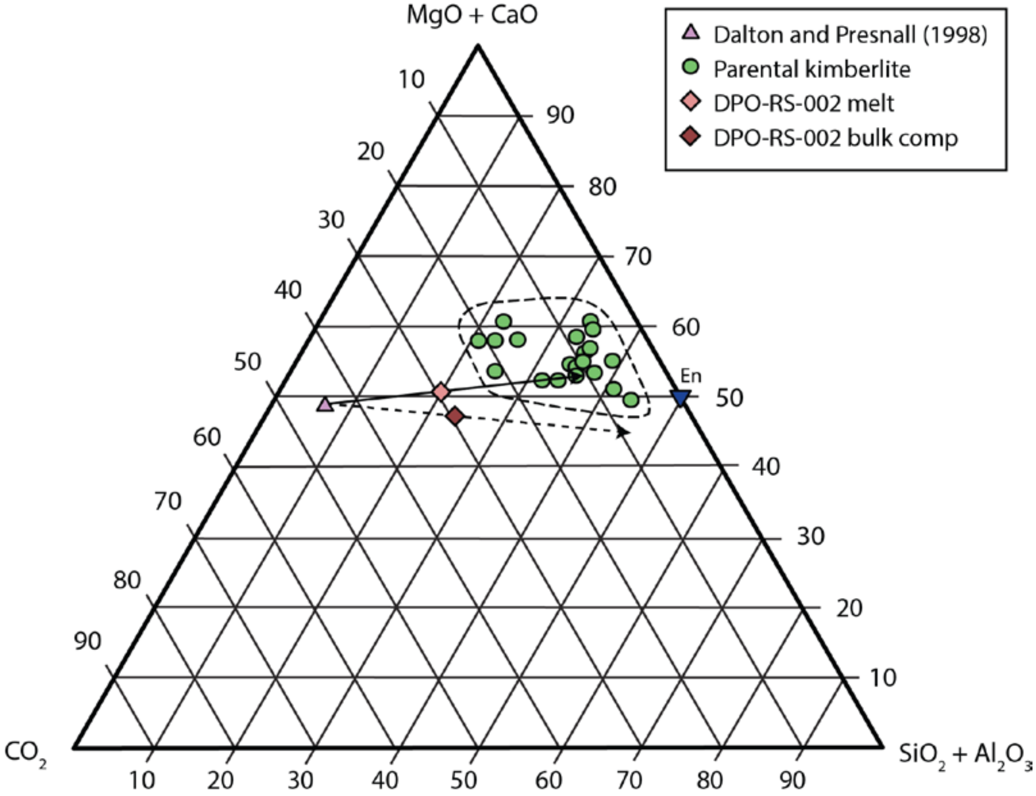

Figure 2.9: A ternary diagram showing the normalized compositions of the DP starting material (Dalton and Presnall, 1998b), the orthopyroxene assimilation experiment DPO-RS-002 melt composition and bulk composition, enstatite, and a field of parental kimberlite compositions (Harris et al., 2004; Kjarsgaard et al., 2009; Kopylova et al., 2007; Le Roex et al., 2003; Price et al., 2000; Russell et al., 2012). The solid line and the dashed line show the evolution trend for the DPO-RS-002 melt and bulk composition, respectively.

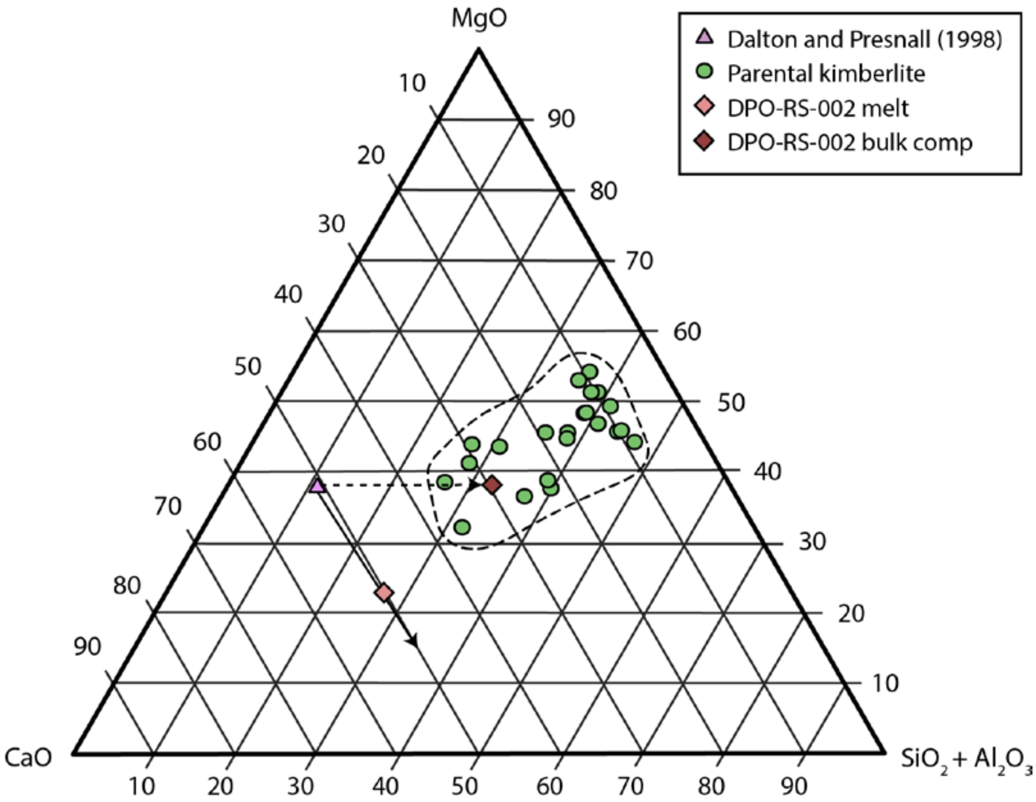

Figure 2.10: A MgO – CaO – SiO_2 + Al_2O_3 ternary diagram showing the normalized compositions of the DPO-RS-002 melt and bulk composition relative to its starting material and the two kimberlitic melt compositions of Igwisi Hills and Kjarsgaard et al. (2009). The solid line shows the evolution of the DPO-RS-002 melt. The dashed line shows the evolution of the bulk composition from the DP starting material to the orthopyroxene assimilation experiment DPO-RS-002.

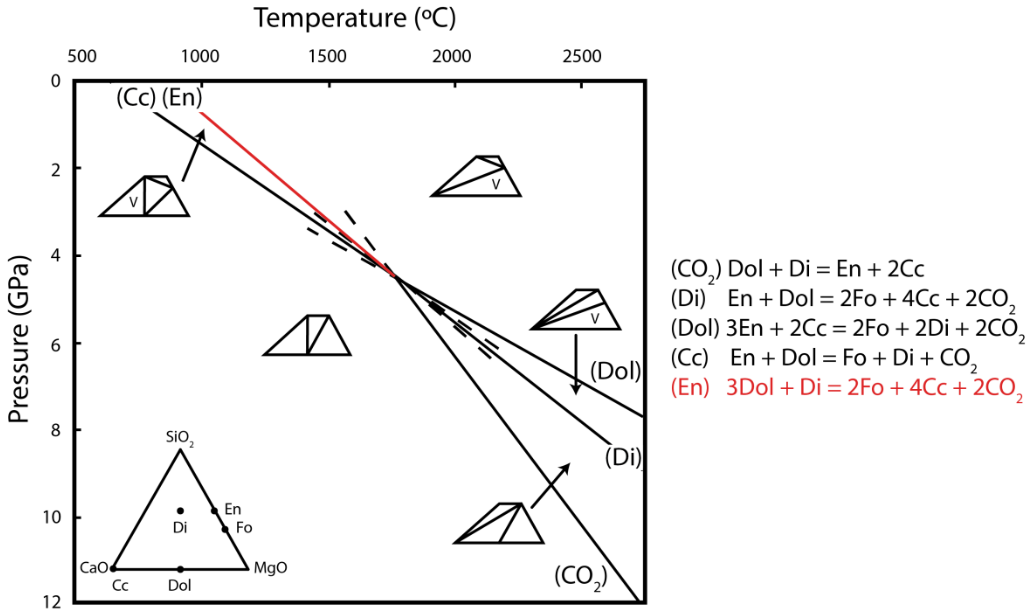

Figure 2.11: The Schreinemakers' analysis for the CMS + CO_2 system run with excess CO_2 as a fluid phase. Solid lines represent the reaction's position in P/T space and the dashed line represents its meta-stable extension. Each reaction is labeled with the "indifferent" phase. The ternary diagrams show the composition of each phase in SiO_2 – MgO – CaO space projected from CO_2 and the tie lines show which phases are stable in each section of PT space. I is the intersection of all four reactions. Reaction (Cc) is where orthopyroxene is assimilated to form diopside, forsterite, and CO_2. Reaction (En) in red just above (Cc) is the decarbonation reaction where diopside reacts with dolomite to form forsterite, calcite, and CO_2.

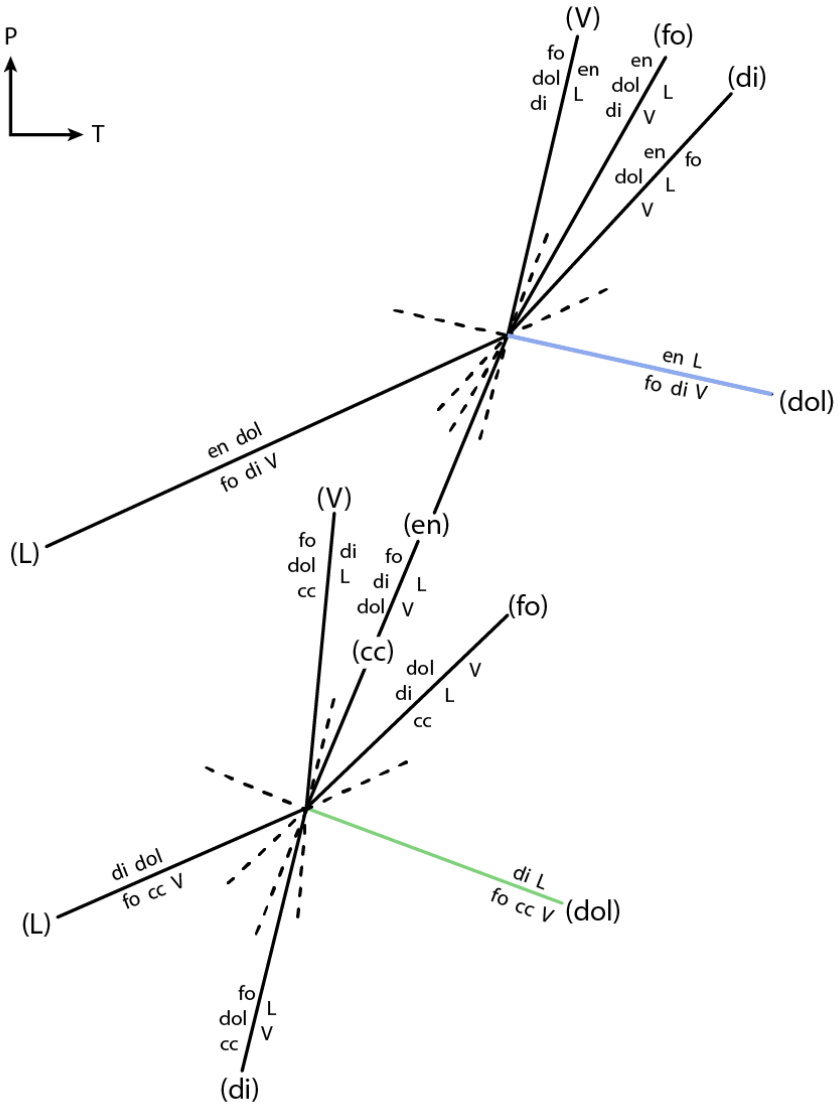

Figure 2.12: The Schreinemakers' analyses for the system CMS + CO_2 around two invariant points, one where calcite is absent (high pressure) and the other where calcite is absent (low pressure). The blue line highlights the orthopyroxene assimilation reaction en + L → fo + di + V. As the kimberlite rises to lower pressures it then intersects the green reaction line where diopside starts to assimilate into the melt via the reaction di + L → fo + cc + V.

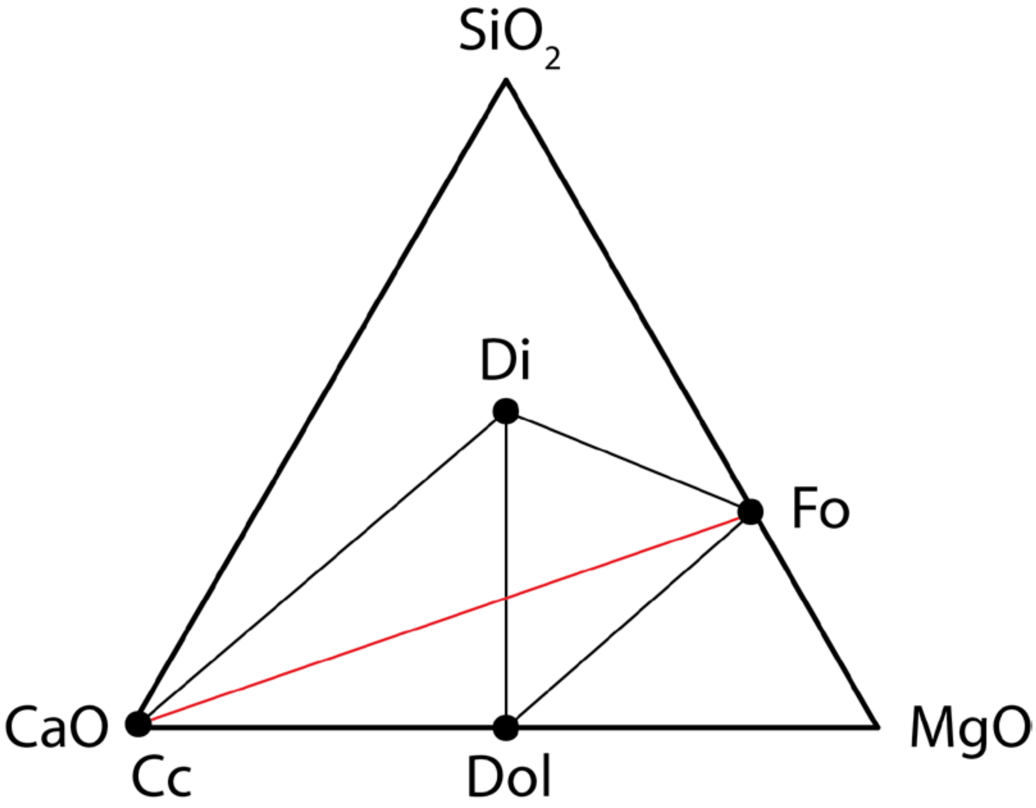

Figure 2.13: A ternary diagram for the CMS + CO_2 system. The diopside breakdown reaction can only happen if the melt has a composition on the opposite side of the calcite – forsterite – CO_2 plane (red line) to diopside. Therefore when the melt becomes too rich in SiO_2 from assimilation of diopside, the diopside reaction will stop, and any remaining xenocrystic diopside will be preserved.

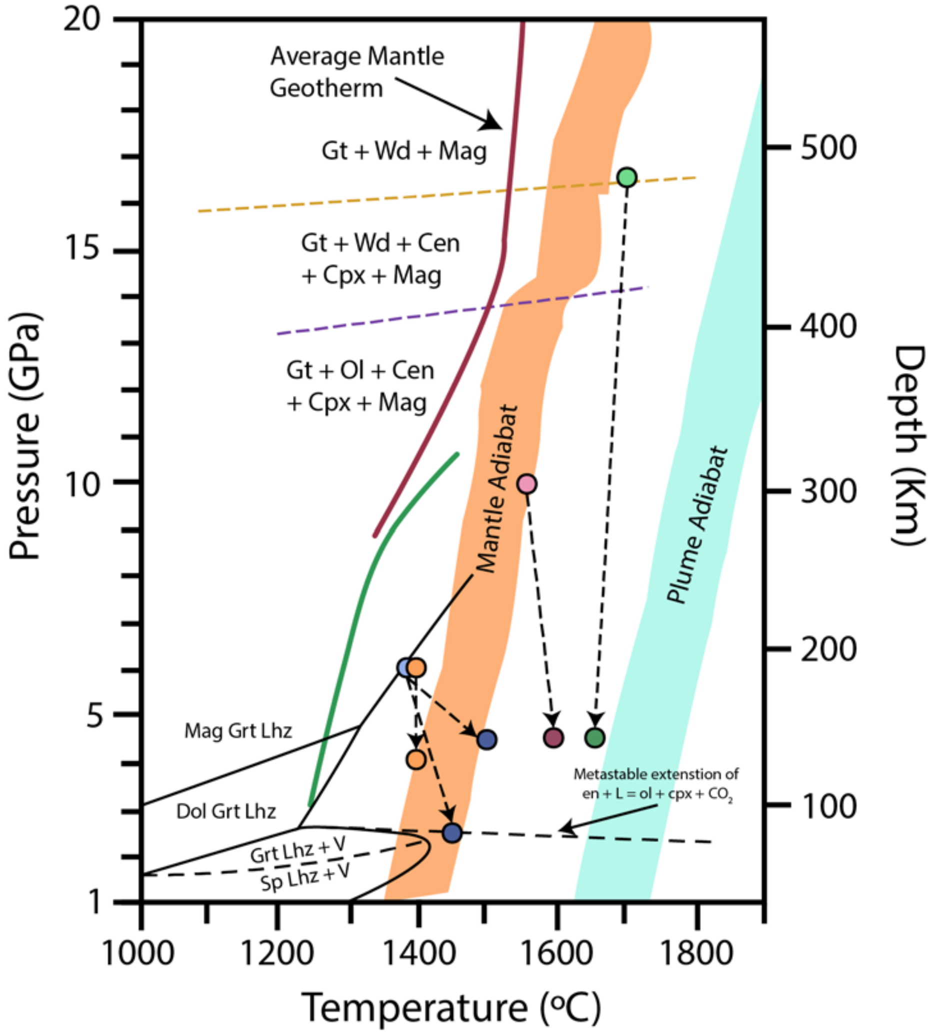

Figure 2.14: The solid red, green, and blue lines show the solidus for alkali-rich carbonated peridotite between 10 -20 GPa (Ghosh et al., 2009), carbonated peridotite in the CMS + CO_2 system between 3 and 12 GPa (Canil and Scarfe, 1990), and carbonated peridotite from the CMAS + CO_2 system (don't know where you pulled in the diagram from). The dashed purple and orange lines show the transition from olivine to wadsleyite and the disappearance of pyroxene respectively. The orange and light blue areas show the adiabats for the mantle and for a plume (Ghosh et al., 2014; Stixrude and Lithgow-Bertelloni, 2007). The orthopyroxene assimilation experiments and starting material pressure and temperature conditions are shown as circles, the lighter coloured circle representing the starting material. Blue is the DP experiments, pink is the K experiments, green is the G experiments, and orange is the C

experiments. There is no lighter coloured circle for the C experiments because OPX-RS-001 and C-RS-001 were run at the same conditions as the starting material.

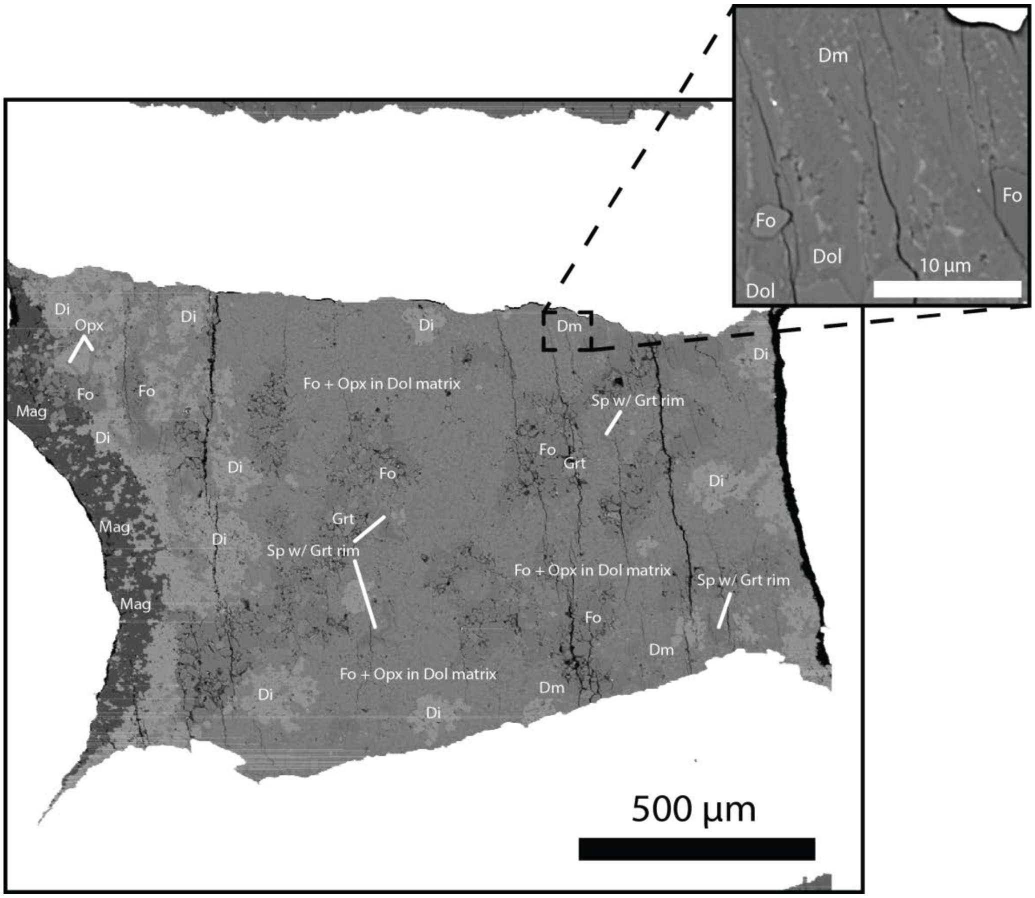

Figure 2.15: A BSE of JD-RS-003 and a close up of an area where melt was present. Run at 7 GPa and 1560ºC.

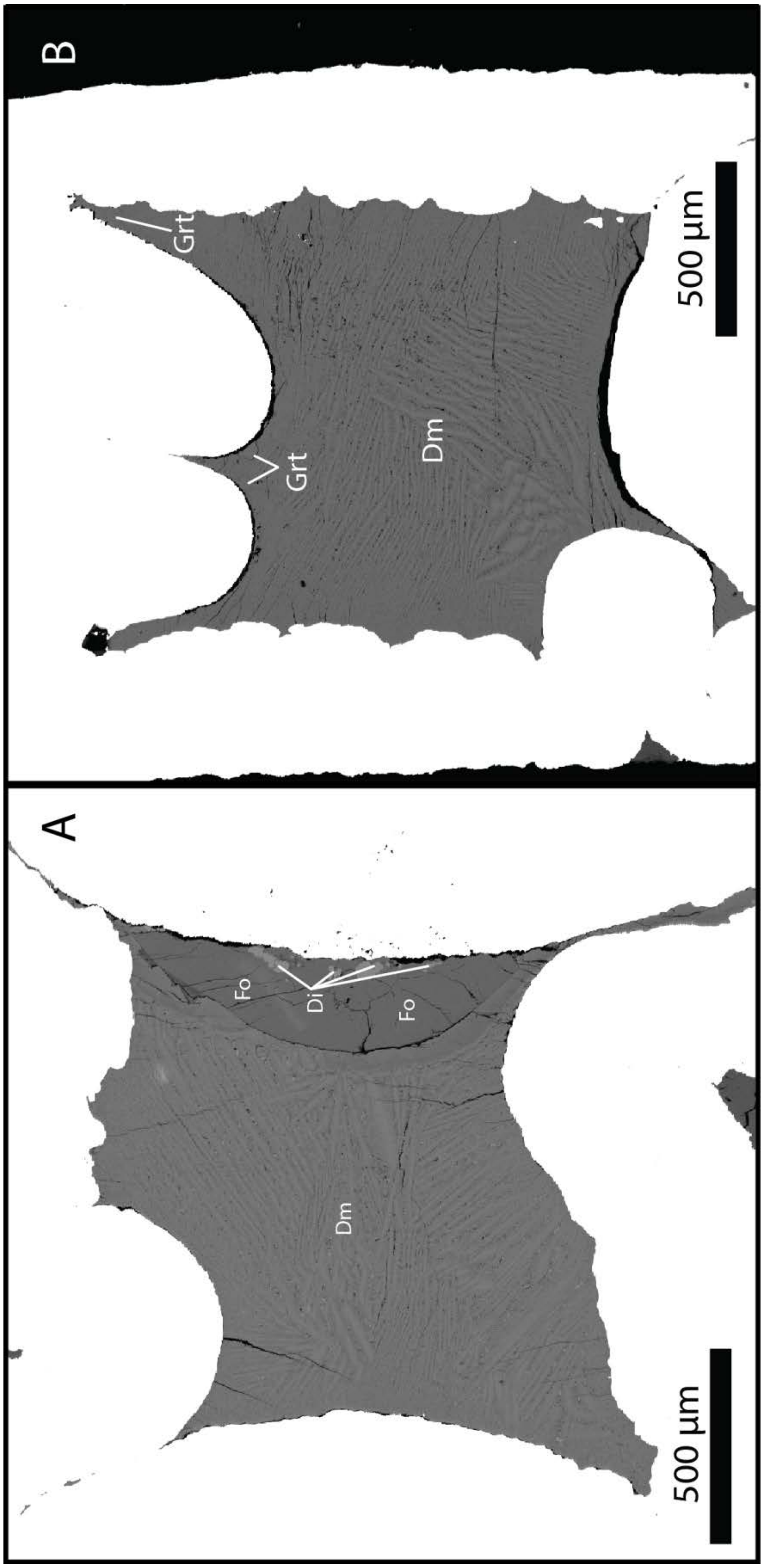

Figure 2.16: BSEs of runs MJD-RS-001 and MMJD-RS-001. Run at 7 GPa and 1560ºC.

Chapter 2 Tables:

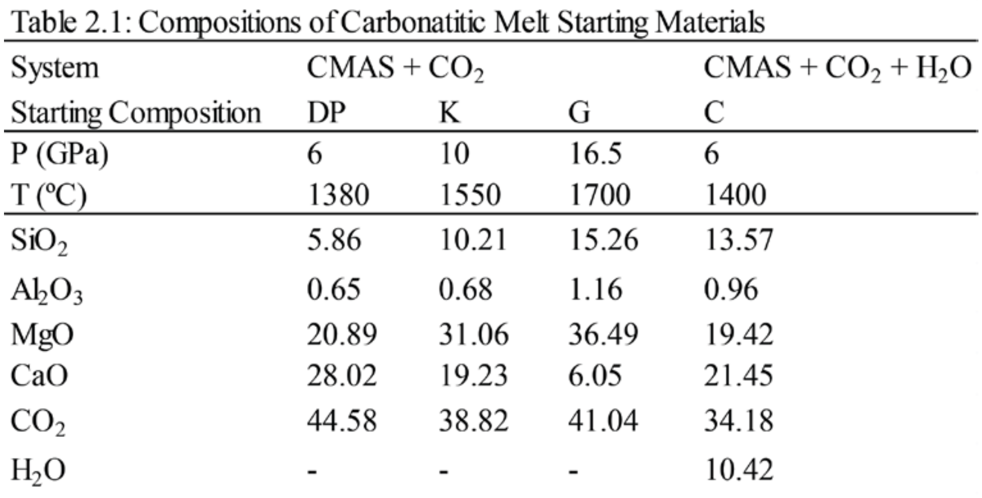

Table 2.1: Compositions of Carbonatitic Melt Starting Materials

System	CMAS + CO_2			CMAS + CO_2 + H_2O
Starting Composition	DP	K	G	C
P (GPa)	6	10	16.5	6
T (ºC)	1380	1550	1700	1400
SiO_2	5.86	10.21	15.26	13.57
Al_2O_3	0.65	0.68	1.16	0.96
MgO	20.89	31.06	36.49	19.42
CaO	28.02	19.23	6.05	21.45
CO_2	44.58	38.82	41.04	34.18
H_2O	-	-	-	10.42

Table 2.2: Experimental Conditions

Run #	Starting Composition	Assembly	Pressure (GPa)	Temp. (ºC)	Duration (hr)	Phases
PC-DP-RS-001	DP melt	12.7mm	2.5	1450	5	fo + sp + melt
DPO-RS-002	DP melt (0.69) + opx (0.31)	12.7mm	2.5	1450	5	fo + di + melt
DP-RS-005	DP melt	18/11M HT	4.5	1500	6	fo + sp + per + melt
DPO-RS-004	DP melt (0.87) + opx (0.13)	18/11M HT	4.5	1500	6	opx + grt + melt
K-RS-003	K melt	18/11M HT	4.5	1600	6	fo + grt + melt
KO-RS-001	K melt (0.89) + opx (0.11)	18/11M HT	4.5	1600	6	mag + opx + grt + fo + melt
G-RS-006	G melt	18/11M HT	4.5	1650	6	opx + grt + mag + melt
GO-RS-002	G melt (0.87) + opx (0.13)	18/11M HT	4.5	1650	6	opx + mag + melt
C-RS-001	C melt	18/11M HT	6	1400	24	coes + mag + melt
OPX-RS-001	C melt (0.64) + opx (0.36)	18/11M HT	6	1400	24	opx + coes + mag + melt
OPX-RS-002	C melt (0.58) + opx (0.42)	18/11M HT	4	1400	4	opx + melt

spinel (sp), garnet (grt), forsterite (fo), coesite (coes), orthopyroxene (opx), periclase (per), diopside (di), magnesite (mag), carbonatitic melt (melt)

Table 2.3: Melt Analyses

Experiment	PC-DP-RS-001	DPO-RS-002	DP-RS-005	DPO-RS-004	K-RS-003	KO-RS-001
No.	13	15	5	10	98	99
SiO_2	3.67 (2.84)^{c}	18.59 (3.33)^{c}	1.75 (0.26)^{b}	3.20 (0.54)^{a}	6.13 (3.85)^{a}	5.64 (2.29)^{a}
Al_2O_3	0.26 (0.16)^{c}	0.96 (0.26)^{c}	0.08 (0.02)^{d}	0.30 (0.04)^{d}	0.54 (0.38)^{d}	0.41 (0.21)^{d}
MgO	18.94 (5.47)^{e}	15.83 (2.43)^{e}	16.06 (0.79)^{e}	19.17 (0.18)^{e}	30.10 (2.20)^{e}	27.18 (1.68)^{e}
CaO	34.96 (5.38)^{e}	35.26 (2.41)^{e}	38.57 (0.77)^{e}	31.95 (0.29)^{e}	21.74 (2.11)^{e}	24.53 (1.23)^{e}
Total	57.83	70.64	56.46	54.62	58.51	57.76
CO_2*	42.17 (3.23)	29.36 (2.85)	43.53 (0.33)	45.37 (0.43)	41.49 (4.25)	42.24 (3.28)
$Ca^{\#}$	0.65	0.69	0.71	0.63	0.42	0.47
O = 6						
Si	0.288	1.105	0.153	0.275	0.431	0.421
Al	0.024	0.067	0.008	0.030	0.045	0.036
Mg	2.249	1.409	2.084	2.459	3.347	3.095
Ca	3.138	2.280	3.599	2.946	1.724	2.009
Total	5.700	4.861	5.843	5.710	5.547	5.561

Table 2.3: Melt Analyses Continued

Experiment	G-RS-006	GO-RS-003	C-RS-001	OPX-RS-001	OPX-RS-002
No.	100	43	14	10	10
SiO_2	12.92 (1.14)^a	14.02 (5.29)^a	7.74 (0.52)^b	18.56 (2.59)^a	16.10 (2.37)^a
Al_2O_3	1.17 (1.02)^d	1.36 (0.36)^a	0.78 (0.09)^d	1.14 (0.09)^d	0.92 (0.24)^d
MgO	38.50 (0.21)^e	41.46 (8.53)^a	25.08 (1.49)^e	21.82 (0.70)^e	22.45 (0.74)^e
CaO	11.41 (2.08)^e	6.72 (2.47)^d	25.98 (1.43)^e	23.74 (0.34)^e	23.05 (0.47)^e
Total	64.00	63.56	59.58	65.26	62.52
CO_2*	36.00 (1.91)	36.44 (2.93)	40.42 (3.56)**	34.74 (0.91)**	37.48 (3.34)**
$Ca^{\#}$	0.23	0.14	0.51	0.52	0.51
O = 6					
Si	0.791	0.841	0.322	1.142	1.045
Al	0.085	0.097	0.039	0.083	0.071
Mg	3.539	3.739	3.068	2.014	2.188
Ca	0.752	0.434	2.229	1.577	1.616
Total	5.167	5.111	5.658	4.817	4.920

All values are presented as wt %. The values in the parantheses are the standard deviation (1σ). The superscript notates the standard used to produce each analyses: a = diopside, b = forsterite (1% Co), c = Frank Smith pyrope, d = spinel, e = dolomite, and f = periclase. This notation will be used in subsequent tables.

* CO_2 was calculated by subtracting the total from 100 wt %.

** Analysis is $H_2O + CO_2$

$Ca^{\#} = CaO/(CaO + MgO)$

Table 2.4: Orthopyroxene Analyses

Experiment	DPO-RS-004	KO-RS-001	G-RS-006	GO-RS-003	OPX-RS-001	OPX-RS-002
No.	5	10	5	10	10	5
SiO_2	59.92 (0.38)[b]	58.26 (0.44)[a]	57.81 (0.90)[a]	59.03 (0.32)[a]	59.79 (0.25)[b]	59.73 (0.23)[b]
Al_2O_3	0.85 (0.55)[d]	1.58 (0.33)[d]	2.72 (0.10)[c]	1.64 (0.13)[c]	0.21 (0.07)[d]	0.35 (0.07)[d]
MgO	37.49 (1.62)[b]	39.92 (0.49)[e]	38.39 (0.43)[c]	38.38 (0.13)[a]	39.10 (0.21)[b]	38.66 (0.19)[b]
CaO	1.52 (1.18)[a]	0.91 (0.20)[e]	0.32 (0.02)[c]	0.23 (0.01)[c]	0.54 (0.14)[a]	1.13 (0.17)[a]
Sum	99.78	100.66	99.25	99.28	99.64	99.87
O = 6						
Si	2.010	1.944	1.929	1.924	2.006	2.003
Al	0.034	0.062	0.012	0.008	0.008	0.014
Mg	1.874	1.986	0.108	0.065	1.956	1.933
Ca	0.055	0.032	1.949	1.985	0.019	0.041
Sum	3.973	4.025	3.997	3.982	3.990	3.990

Table 2.5: Olivine Analyses

Experiment	PC-DP-RS-001	DPO-RS-002	DP-RS-005	K-RS-003	KO-RS-001
No.	5	10	5	5	10
SiO_2	42.07 (0.21)^{b}	42.00 (0.37)	42.60 (0.11)^{b}	42.57 (0.21)^{b}	42.85 (0.20)^{b}
Al_2O_3	0.20 (0.02)^{d}	0.04 (0.03)	0.12 (0.08)^{d}	0.10 (0.01)^{c}	0.08 (0.01)^{c}
MgO	56.99 (0.42)^{b}	57.06 (0.69)	57.43 (0.32)^{b}	56.21 (0.49)^{b}	56.72 (0.27)^{b}
CaO	0.34 (0.04)^{a}	0.55 (0.25)	0.16 (0.03)^{a}	0.09 (0.01)^{a}	0.08 (0.01)^{a}
Sum	99.60	99.65	100.30	98.97	99.466
O = 4					
Si	0.991	0.990	0.995	1.006	1.002
Al	0.006	0.001	0.003	0.003	0.002
Mg	2.001	2.005	2.000	1.981	1.990
Ca	0.009	0.014	0.004	0.002	0.002
Sum	3.006	3.010	3.003	2.992	2.997

Table 2.6: Garnet Analyses

Experiment No.	DPO-RS-004 5	K-RS-003 5	KO-RS-001 5	G-RS-006 5
SiO_2	44.31 (0.47)^c	44.78 (0.44)^c	44.48 (0.42)^a	45.27 (0.23)^a
Al_2O_3	24.02 (0.23)^c	24.04 (0.16)^c	23.49 (0.20)^d	24.18 (0.20)^c
MgO	26.21 (0.28)^c	28.40 (0.48)^c	28.12 (0.31)^a	29.81 (0.12)^c
CaO	4.45 (0.42)^a	1.93 (0.07)^a	3.25 (0.12)^a	0.83 (0.01)^c
Sum	98.99	99.15	99.33	100.10
O = 12				
Si	3.040	3.045	3.035	3.041
Al	1.942	1.927	1.889	1.915
Mg	2.680	2.879	2.860	2.986
Ca	0.327	0.140	0.238	0.060
Sum	7.989	7.991	8.021	8.002

Table 2.7: Clinopyroxene Analyses

Experiment No.	DPO-RS-002 4
SiO_2	55.63 (0.21)^a
Al_2O_3	0.57 (0.11)^d
MgO	21.63 (0.22)^a
CaO	21.42 (0.75)^a
Sum	99.25
O = 6	
Si	1.993
Al	0.024
Mg	1.155
Ca	0.822
Sum	3.995

Table 2.8: Coesite Analyses

Experiment No.	C-RS-001 3	OPX-RS-001 5
SiO_2	98.32 (0.39)^a	100.09 (0.22)^b
Al_2O_3	0.02 (0.01)^d	0.03 (0.01)^d
MgO	0.01 (0.01)^a	0.01 (0.01)^b
CaO	0.02 (0.01)^a	0.02 (0.01)^a
Sum	98.37	100.15
O = 2		
Si	1.000	0.999
Al	0.000	0.000
Mg	0.000	0.000
Ca	0.000	0.000
Sum	1.000	1.000

Table 2.9: Magnesite Analyses

Experiment No.	KO-RS-001 10	G-RS-006 10	GO-RS-003 5	C-RS-001 3	OPX-RS-001 5
SiO_2	0.04 (0.01)^a	0.01 (0.01)^a	0.02 (0.01)^e	0.04 (0.02)^b	0.11 (0.08)^a
Al_2O_3	0.01 (0.01)^d	0.02 (0.01)^a	0.02 (0.01)^f	0.02 (0.01)^d	0.03 (0.03)^d
MgO	44.42 (0.39)^f	47.01 (0.17)^a	46.94 (0.48)^a	45.63 (0.63)^f	44.24 (1.61)^a
CaO	3.62 (0.44)^c	1.23 (0.07)^d	0.96 (0.03)^c	2.95 (0.06)^a	2.72 (0.19)^a
Sum	48.08	48.27	47.94	48.63	47.09
CO_2*	51.92 (0.30)	51.73 (0.18)	52.06 (0.50)	51.37 (0.62)	52.91 (1.70)
$Ca^{\#}$	0.08	0.03	0.02	0.04	0.06
O = 3					
Si	0.002	2.942	2.953	0.001	0.005
Al	0.000	0.055	0.043	0.001	0.001
Mg	2.830	0.001	0.001	2.863	2.863
Ca	0.166	0.001	0.001	0.133	0.126
Sum	2.998	2.999	2.999	2.998	2.995

Table 2.10: Spinel Analyses

Experiment	PC-DP-RS-001	DP-RS-005
No.	3	5
SiO_2	0.40 (0.04)[a]	1.13 (0.25)[b]
Al_2O_3	68.53 (1.62)[d]	68.58 (0.71)[d]
MgO	29.74 (0.53)[d]	29.63 (0.48)[d]
CaO	0.27 (0.13)[a]	0.15 (0.05)[a]
Sum	98.95	99.49
O = 4		
Si	0.010	0.027
Al	1.939	1.927
Mg	1.062	1.053
Ca	0.009	0.004
Sum	3.020	3.010

Table 2.11: Periclase Analysis

Experiment	DP-RS-005
No.	5
SiO_2	0.02 (0.01)[b]
Al_2O_3	0.76 (0.03)[d]
MgO	98.30 (0.93)[f]
CaO	0.12 (0.05)[a]
Sum	99.20
O = 1	
Si	0.000
Al	0.006
Mg	0.990
Ca	0.001
Sum	0.997

Table 2.12: Dolomite melt inclusion analyses

Experiment	DP-RS-005
No.	3
SiO_2	1.06 (0.47)^b
Al_2O_3	0.07 (0.02)^d
MgO	15.10 (0.66)^e
CaO	38.78 (0.88)^e
Sum	55.01
CO_2*	44.99 (0.35)
$Ca^{\#}$	0.61
O = 6	
Si	0.096
Al	0.007
Mg	2.037
Ca	3.761
Sum	5.901

Table 2.13: T-test results for modified melts, non-orthopyroxene experiment versus orthopyroxene-bearing experiment

Experiment	SiO_2	Al_2O_3	MgO	CaO	CO_2
PC-DP-RS-001	4.60	2.93	19.58	33.05	39.85
DPO-RS-002	18.59	0.96	15.83	35.26	29.36
DP-RS-005	4.41	1.20	18.61	35.66	40.13
DPO-RS-004	3.36	0.39	19.20	31.84	45.20
K-RS-003	7.92	0.73	31.14	20.71	39.49
KO-RS-001	10.58	0.35	33.57	18.46	37.03
G-RS-006	12.72	1.24	39.19	10.27	36.58
GO-RS-003	13.26	1.29	41.76	6.42	37.27
C-RS-001	13.80	0.70	24.12	23.33	38.05
OPX-RS-001	18.58	1.09	22.50	22.70	35.14
C-RS-001	13.80	0.70	24.12	23.33	38.05
OPX-RS-002	16.10	0.92	22.45	23.05	37.48

Table 2.14: T-test results for modified melts, experiment versus starting material

Experiment	SiO_2	Al_2O_3	MgO	CaO	CO_2	H_2O
PC-DP-RS-001	4.60	2.93	19.58	33.05	39.85	
DPO-RS-002	18.59	0.96	15.83	35.26	29.36	
DP-RS-005	4.41	1.20	18.61	35.66	40.13	
DPO-RS-004	3.36	0.39	19.20	31.84	45.20	
DP	**5.86**	**0.65**	**20.89**	**28.02**	**44.58**	
K-RS-003	7.92	0.73	31.14	20.71	39.49	
KO-RS-001	10.58	0.35	33.57	18.46	37.03	
K	**10.21**	**0.68**	**31.06**	**19.23**	**38.82**	
G-RS-006	12.72	1.24	39.19	10.27	36.58	
GO-RS-003	13.26	1.29	41.76	6.42	37.27	
G	**15.26**	**1.16**	**36.49**	**6.05**	**41.04**	
C-RS-001	13.80	0.70	24.12	23.33	38.05	
OPX-RS-001	18.58	1.09	22.50	22.70	35.14	
OPX-RS-002	16.10	0.92	22.45	23.05	37.48	
C	**13.57**	**0.96**	**19.42**	**21.45**	**34.18**	**10.42**

Table 2.15: Gudfinnsson and Presnall Melts and Melt Analyses

Experiment	JADSCM-8	PR-106	JD-RS-003	MJD-RS-001	MMJD-RS-001
No.	-	25	5	10	194
SiO_2	46.57	8.48 (4.8)	5.90 (2.34)^a	1.78 (1.44)^a	1.55 (2.22)^a
Al_2O_3	3.31	0.29 (0.20)	0.22 (0.08)^b	0.11 (0.09)^d	0.19 (0.20)^d
MgO	32.76	25.00 (4.29)	21.23 (1.14)^a	15.36 (1.64)^c	14.13 (1.57)^c
CaO	12.48	27.19 (3.10)	29.65 (0.66)^a	37.25 (1.63)^c	38.91 (2.85)^c
Total	95.12	60.96	57.00	54.51	54.78
CO_2*	12.24	39.03 (4.13)	43.00 (2.10)	45.49 (1.56)	45.22 (1.94)
O = 6					
Si	-	-	0.591	0.155	0.130
Al	-	-	0.040	0.011	0.019
Mg	-	-	2.427	2.059	1.908
Ca	-	-	2.332	3.615	3.802
Sum	-	-	5.389	5.840	5.860

All values are presented as wt %. The values in the parantheses are the standard deviation (1σ). The superscript notates the standard used to produce each analyses: a = diopside, b = anorthite, c = dolomite, and d = spinel.

* CO_2 was calculated by subtracting the total from 100 wt%.

Chapter 3: Assimilation Modeling

3.1 Introduction:

The results of the experiments described in Chapter 2 showed that the paucity of orthopyroxene xenocrysts in kimberlites can be explained by a decarbonation reaction that leads to precipitation of olivine and clinopyroxene, exsolution of CO_2, and SiO_2 enrichment in the melt. This explanation differs from the Russell et al. (2012) model in the assimilation mechanism of orthopyroxene and the depth at which orthopyroxene assimilation and CO_2 exsolution occurs. Another aspect of the Russell et al. (2012) model is that primary kimberlitic melts are originally carbonatitic in composition and evolve to kimberlitic melt compositions via mainly orthopyroxene assimilation. They demonstrated this by performing a number of experiments adding increasing amounts of orthopyroxene to a Na_2CO_3 melt and analyzing the resulting melts. They also modeled orthopyroxene assimilation by adding increasing amounts of orthopyroxene to a simple CMAS + CO_2 carbonatite melt and compared the melt compositions to melts from Igwisi Hills, a modern example of kimberlitic-like melts, and found that carbonatites can evolve to similar compositions after assimilating 15-20 wt.% orthopyroxene (Russell et al., 2012).

Our 2.5 GPa orthopyroxene assimilation experiment, however, shows that with 30 wt.% orthopyroxene assimilation the melt composition does evolve towards the Igwisi Hills composition but does not reach it. This result brings into question whether primary kimberlitic melts are originally carbonatitic and if so, whether orthopyroxene assimilation alone can modify the melts to kimberlitic compositions. To test these ideas we performed three sets of assimilation calculations: the first investigates the affect of orthopyroxene assimilation relative to the amount of bulk mantle contamination observed in kimberlites (Model I), the second uses the same conditions as the first model but also evaluates the possible affect of assimilating clinopyroxene and garnet

(Model II), and a final model looks at the affect of orthopyroxene assimilation in isolation (Model III), similar to that of Russell et al. (2012). These models should help us understand orthopyroxene's role in the evolution of kimberlite melts and whether carbonatitic melts are indeed primary kimberlitic melts.

3.2 Methods:

Several carbonatite melts were chosen from the literature as possible primary kimberlite melts (Table 3.1). Most of these melts were used in the orthopyroxene assimilation experiments in Chapter 2 (Dalton and Presnall, 1998b; Ghosh et al., 2014; Girnis et al., 2011; Gudfinnsson and Presnall, 2005; Keshav and Gudfinnsson, 2014), with the exception of a carbonatitic melt from Foley et al. (2009). This latter melt was in equilibrium with potassium-enriched Hawaiian pyrolite with 40 wt.% olivine removed at 5 GPa and 1180ºC (Foley et al., 2009). The melts for compositions from Girnis et al. (2011), Foley et al. (2009), and Ghosh et al. (2014) have been renormalized from their complex systems into CMAS + CO_2 to allow comparison with the other melts.

The composition and mineralogy of the contaminating mantle used in the assimilation calculations is based on a garnet lherzolite xenolith from Bultfontein, South Africa (Table 3.2) (Canil and O'Neill, 1996). In the first model, orthopyroxene assimilation calculations are based on mantle contamination of 10, 20, 30, 40, and 50 wt.%, which in turn is equivalent to 2.46, 4.96, 7.38, 9.84, and 12.30 wt.% assimilation of orthopyroxene, with olivine, clinopyroxene, and garnet being considered as inert xenocrysts that are unreactive with the carbonatitic melt. In the second model, clinopyroxene and garnet also react with the melt leading to the assimilation of 1.37, 2.74, 4.11, 5.48, and 6.85 wt.% clinopyroxene and 1.22, 2.44, 3.66, 4.88, and 6.10 wt.% garnet along with assimilation of orthopyroxene from the first model. The third model again assumes the assimilation of only orthopyroxene, but this time at

10, 20, 30, 40, and 50 wt.% levels. The equations and resulting melt compositions for all the assimilation calculations are in Appendix 4.

Because our experiments showed that orthopyroxene assimilation does indeed lead to CO_2 exsolution, we needed to find a way to incorporate this process into our assimilation models. This was done using the only data currently available, those of Russell et al. (2012). From their assimilation experiments, they derived an equation to correlate CO_2 exsolution to the amount of orthopyroxene assimilation:

$$W_f = W_i(1 - 2.17w_{opx})$$

Where W_f is the final CO_2 content of the melt, W_i is the initial CO_2 content, and w_{opx} is the weight fraction of orthopyroxene assimilated. We used this to model CO_2 exsolution in our assimilation calculations.

Twenty two kimberlitic melts proposed by previous authors to be representative of the composition of the kimberlite when emplaced (parental kimberlite melts) were used to illustrate the target compositional field that the evolving melts should reach (Table 3.3). Eight of these melts are kimberlites from the Lac de Gras area with varying percentages of olivine or peridotite removed from their compositions (Kjarsgaard et al., 2009). Four of the others are the same kimberlitic melts Russell et al. (2012) used for their comparisons, which were melt compositions from the Igwisi Hills kimberlite (Dawson, 1994). Two of the Igwisis Hills compositions have been modified to remove the effect of xenocrystic olivine. The rest of the melts are those from Table 1.1 (Chapter 1).

In these models, we will illustrate the melt evolution trends on (SiO_2 + Al_2O_3) – (MgO + CaO) – CO_2 and (SiO_2 + Al_2O_3) – MgO - CaO ternary diagrams (with compositions plotted in wt.%)

3.3 Results:

The results from the Model I assimilation calculation are shown in Figures 3.1 and 3.2. All the melts except for Girnis et al. (2011) follow a similar melt evolution, becoming more enriched with SiO_2 + Al_2O_3 and MgO + CaO, but becoming more CO_2 depleted as assimilation and degassing continue. The evolution of the Girnis et al. (2011) melt also shows a decrease in CO_2 content and an increase in SiO_2 + Al_2O_3, but decreases in MgO + CaO with increasing mantle contamination. This is partly because the initial CO_2 content of the Girnis et al. (2011) is approximately 30 wt.% lower than other melts, decreasing the effect of CO_2 degassing. The Girnis et al. (2011) melts are the only that reach the kimberlitic composition field at 50 wt.% mantle contamination; all the other melts evolve towards kimberlitic melt compositions but would need an additional 30 - 40 wt.% mantle contamination to reach kimberlitic melt compositions. The (SiO_2 + Al_2O_3)–MgO-CaO ternary diagram (Figure 3.2) shows that all the carbonatitic melts evolve towards the kimberlitic compositions in this space, except for that of Ghosh et al. (2014) which narrowly misses the field. Each trend has a different orientation, but they all point towards the composition of orthopyroxene. Once again, only the Girnis et al. (2011) melt reaches kimberlitic compositions; all the others do not reach the kimberlite field.

The results from the Model II assimilation calculations are shown in Figures 3.3 and 3.4. With the addition of clinopyroxene and garnet to the melt the trajectories all curve further towards the silicate compositions and away from the trajectory for pure CO_2 exsolution, and all evolve further than the previous model, indicating that the effect of exsolution has decreased with the addition of these two minerals to the assimilant. Now all the melts are evolving straight towards the compositions of orthopyroxene and clinopyroxene. The Girnis et al. (2011) melt evolves to compositions right in the middle of the kimberlite field in Figure 3.3, entering it by 10 wt.% mantle contamination. The (SiO_2 + Al_2O_3)–MgO-CaO ternary diagram (Figure 3.4) shows that all the carbonatitic melts intersect and enter the kimberlite field in this space. The Girnis et al. (2011) melt enters the field by approximately 5 wt.% mantle contamination, whereas the other melts enter the field by 30-40 wt.% contamination. The trends of the melts is approximately toward the composition of that of garnet, which is the about the average composition of the three silicates involved.

Model III, which calculates the assimilation of orthopyroxene of 10, 20, 30, 40, and 50 wt.% shows that all the melts evolve towards and intersect the field of kimberlitic compositions in Figure 3.5. Each melt with the exception of Girnis et al. (2011) intersects the kimberlite field by 15 – 25 wt.% orthopyroxene assimilation. Girnis et al. (2011) intersects at 10 wt.% orthopyroxene assimilation. At 50 wt.% assimilation all the melts have left the kimberlitic field and have a CO_2 content of zero. It is evident looking at the trajectories of the melt compositions relative to the trajectories for pure orthopyroxene assimilation and pure CO_2 exsolution that both processes have relatively equal affects on the evolution of the melt. Looking at the (SiO_2 + Al_2O_3) – MgO - CaO ternary diagram (Figure 3.6), it is evident that all the melts except that of Ghosh et al. (2014) intersect the kimberlite field, evolving towards the composition of orthopyroxene.

3.4 Discussion

The results from these calculations are consistent with two scenarios by which carbonatitic melts can evolve to kimberlitic melts via assimilation. The Model I calculations show that carbonatitic melts cannot evolve to kimberlitic melts by orthopyroxene assimilation in the amounts implied by the extent of mantle contamination observed in kimberlites. The Model II assimilation calculations demonstrate that carbonatitic melts with a composition similar to that of the Girnis et al. (2011) melt can evolve to kimberlitic compositions by assimilation of orthopyroxene, clinopyroxene, and garnet by 15 wt.% mantle contamination. The Model III calculations provide a second possibility whereby carbonatitic melts of a variety of compositions evolve to parental kimberlitic melts by orthopyroxene assimilation in amounts higher than one would expect based on the xenolith/xenocryst assemblage, consistent with the Russell et al. (2012) calculations. By 15 – 25 wt.% assimilation, all the melts evolve to kimberlitic melt compositions in (SiO_2 + Al_2O_3) – (MgO + CaO) – CO_2 compositional space. The (SiO_2 + Al_2O_3) – MgO – CaO ternary diagram shows that the Ghosh et al. (2014) melt composition is too MgO rich to evolve into the field of kimberlitic melt compositions. This result may suggest a depth bound to the source region for the primary kimberlite melt, because this melt was generated at 16.5 GPa, higher than the other melt compositions.

It is possible that either any of the three models outlined above could allow carbonatites evolve to kimberlites depending on the composition of the initial carbonatitic melt and the amount of different minerals that assimilated into the melt during ascent. If the first model applies, then the range of primary kimberlite melt compositions are restricted to being near the field of kimberlite compositions and to having a relatively low CO_2 concentration like that of the Girnis et al. (2011) melt, otherwise the carbonatite will evolve past the kimberlite field like the other carbonatitic melts (see Figure 3.3). It will also be vital to understand exactly what role clinopyroxene and garnet play as possible important secondary minerals in future assimilation experiments. The stability of clinopyroxene and garnet in carbonatitic to transitional melts has not been evaluated experimentally, nor has the effect of the formation of kelyphite rims in garnets on the chemistry of the melt been evaluated.

If the second model is correct, with garnet and clinopyroxene assimilating along with orthopyroxene, then primary kimberlitic melts could form at a large range of pressures and temperatures leading to a range in compositions. In this case, we must conclude that either the estimates of the amount of mantle contamination are incorrect or it is not possible to calculate the amount of the orthopyroxene, clinopyroxene, and garnet assimilated based on the estimated amount of xenocrystic olivine in the kimberlite. The estimates of the amount of mantle contamination could be incorrect if the amount of xenocrystic olivine has been underestimated because of the difficulty in unequivocally distinguishing xenocrystic from phenocrystic olivine. The rounded nature of a large portion of the olivine assemblage suggests that it is also possible that olivine could be assimilating into the kimberlitic melt despite its high stability relative to the other mantle minerals. If so, the amount of xenocrystic olivine in the kimberlite would be underestimated. This would also have an effect on the evolving melt; pushing it towards more SiO_2 and MgO rich compositions therefore tilting the melt trajectories towards the SiO_2 + Al_2O_3 vertex in the (SiO_2 + Al_2O_3) – (MgO + CaO) – CO_2 ternary diagram. However, it is also possible that the rounding of the olivine grains is because of mechanical milling during ascent, in which case it is possible that the olivine is not assimilating into the melt (Brett et al., 2015).

The crystallization of olivine that could accompany orthopyroxene and clinopyroxene assimilation would have the exact opposite effect to the assimilation of olivine outlined above. Estimating olivine assimilation or crystallization from the kimberlite xenolith/xenocryst assemblage alone is impossible, but experiments at high pressure and temperature could help with modeling dissolution rates and create a starting point for modeling of olivine assimilation and/or crystallization.

These models also do not take into account other, olivine-free lithologies that are found as xenoliths in kimberlites, such as websterite or eclogite. Either of these rock types would provide additional amounts of orthopyroxene and/or clinopyroxene contamination, but it is hard to constrain their contribution because their abundance in the mantle are not well constrained. Chepurov et al. (2013) attribute this in part to their lack of preservation because of their instability (Chepurov et al., 2013). Another possible way to add orthopyroxene and clinopyroxene without olivine is through reactions with the surrounding wall rock during ascent, but again, this is hard to estimate and may only have a minor effect depending on dissolution rates of various mantle minerals and the ascent rate of the ascending kimberlite melt.

Another aspect of the calculations that needs to be refined in the future is the CO_2 exsolution modeling, which was based on the experiments of Russell et al. (2012) on orthopyroxene assimilation at atmospheric pressure. It is possible that the amount of CO_2 exsolution that occurs because of orthopyroxene assimilation may change at higher pressures, which would significantly change the trajectory of the melt evolution for each individual carbonatite, at least in $(SiO_2 + Al_2O_3) - (MgO + CaO) - CO_2$ space. It is therefore very important that future high-pressure experiments constrain how CO_2 exsolution changes with increasing orthopyroxene assimilation. As discussed in Chapter 2, it is also possible that clinopyroxene could also be contributing to the exsolution of CO_2, though to a lesser extent than orthopyroxene. Clinopyroxene assimilation experiments may show this to be the case, and if so, this should also be included in CO_2 exsolution modeling along with orthopyroxene.

Additional assimilation experiments studying the behavior of olivine, garnet, and clinopyroxene in addition to orthopyroxene in carbonatitic to transitional melts would greatly improve our understanding of assimilation and how kimberlites evolve. Our current models show that with additional CO_2 exsolution and very extensive orthopyroxene ± clinopyroxene assimilation it is indeed possible that carbonatitic and transitional melts from a range of mantle pressure and temperature could evolve to kimberlitic compositions.

3.5 Conclusion

The assimilation models presented in this chapter show that carbonatitic to transitional melts can potentially evolve to kimberlitic melts compositions either by the assimilation of xenoliths via mantle contamination to a transitional melt or by the extensive assimilation of orthopyroxene into carbonatitic melt. Orthopyroxene has a strong effect on primary kimberlite melt evolution, but CO_2 exsolution and clinopyroxenes and garnet assimilation may also play a large role.

Using a different perspective to attempt to constrain these models, Appendix 5 explores the relationship between SiO_2 content of various kimberlites around the world were compared with the orthopyroxene content of the underlying lithosphere. The results from the exercise are consistent with the above conclusions. Future experimental work studying the assimilation of these minerals in a range of silicate-carbonate melt compositions focusing on melt evolution and CO_2 exsolution will be needed to further understand the formation of kimberlites.

Chapter 3 Figures:

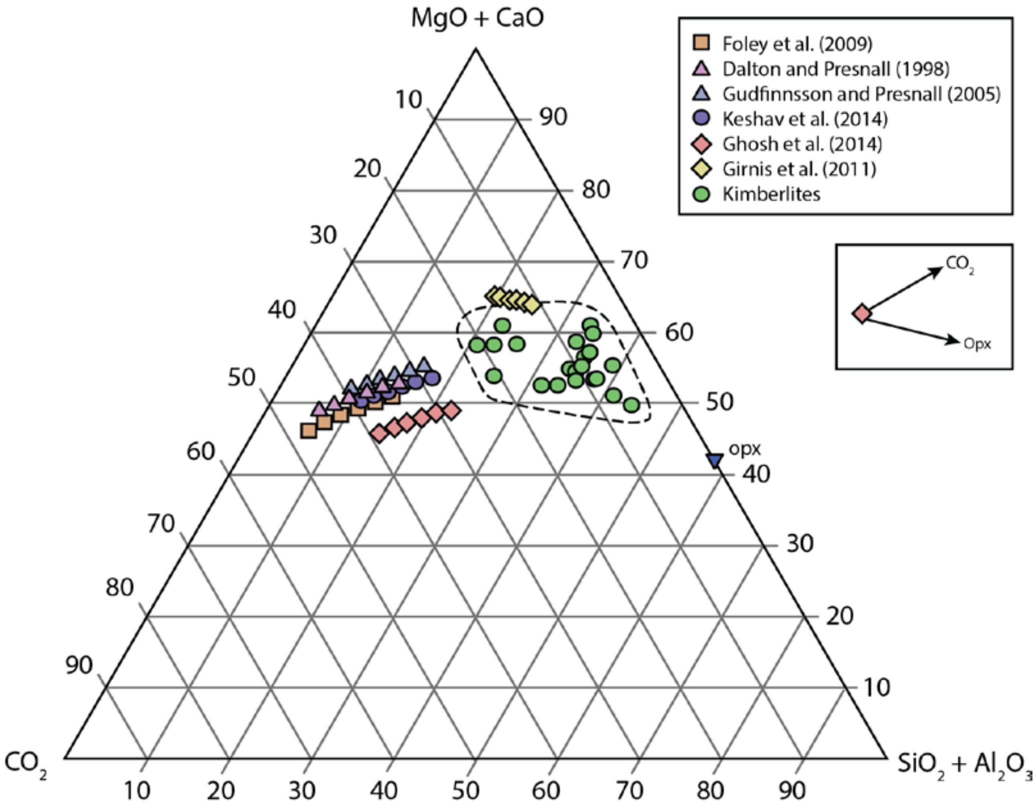

Figure 3.1: The Model I assimilation calculation showing the assimilation of orthopyroxene via 0, 10, 20, 30, 40, and 50 wt.% mantle contamination of a xenolith with 25% orthopyroxene in (MgO + CaO) – (SiO_2 + Al_2O_3) - CO_2 compositional space. The composition of orthopyroxene, clinopyroxene, and garnet are shown in addition to the evolution melts using inverted blue, green, and red triangles respectively. The assimilation trajectories for each mineral and the trajectory for CO_2 exsolution are shown below the legend. These symbols will be used for all following assimilation diagrams. The dashed line indicates the kimberlite melt composition field.

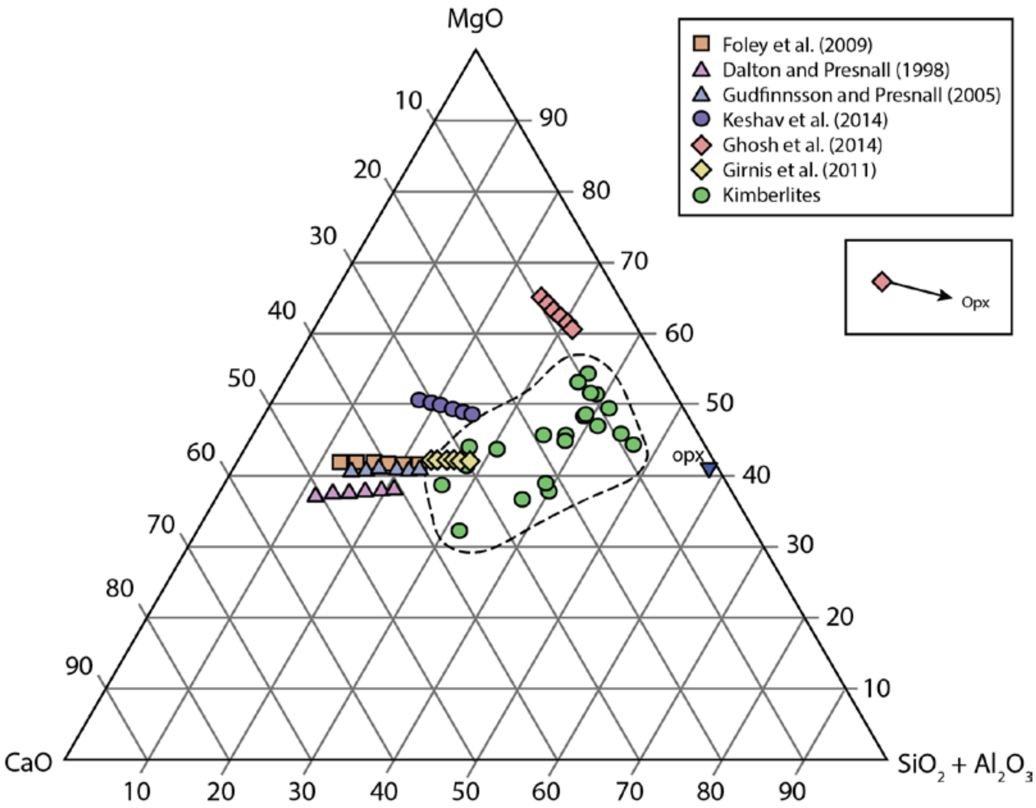

Figure 3.2: The Model I assimilation calculation showing the assimilation of orthopyroxene via 0, 10, 20, 30, 40, and 50 wt.% mantle contamination of a xenolith with 25% orthopyroxene plotted in MgO - CaO - (SiO_2 + Al_2O_3) compositional space. The assimilation trajectories for each mineral are shown below the legend.

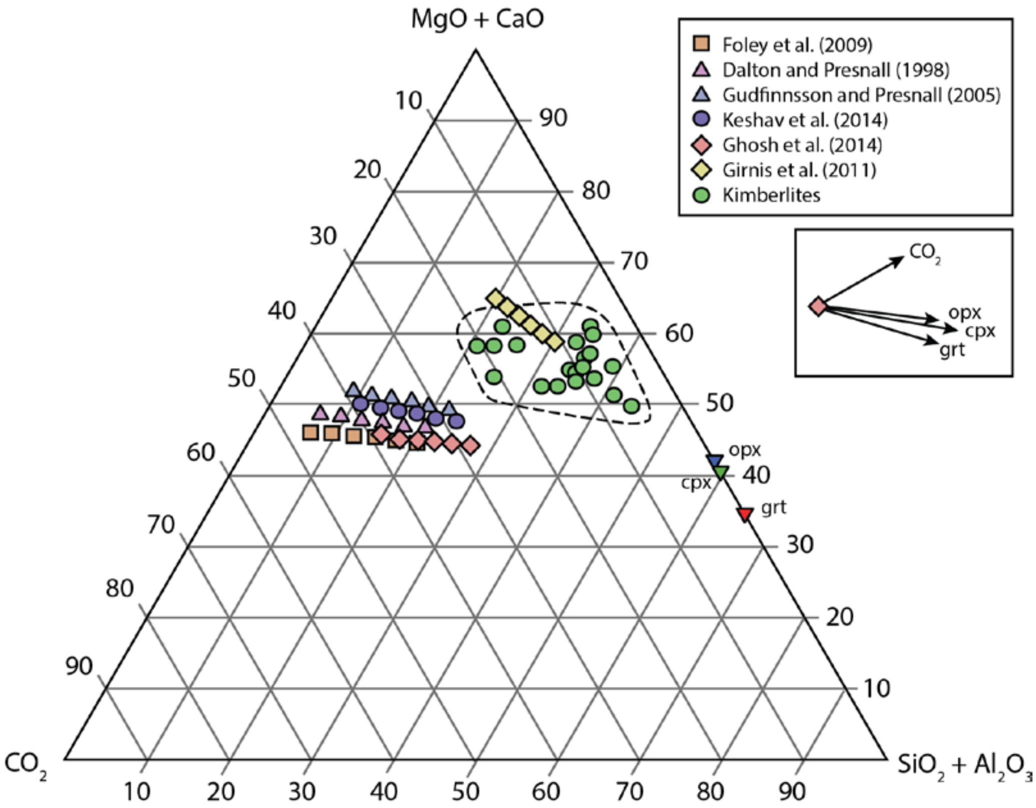

Figure 3.3: The results of the Model II calculation, showing the assimilation of orthopyroxene, clinopyroxene, and garnet via 0, 10, 20, 30, 40, and 50 wt.% mantle contamination of a xenolith with 25% orthopyroxene, 14% clinopyroxene, and 12% garnet plotted in (MgO + CaO) – ($SiO_2 + Al_2O_3$) - CO_2 composition space.

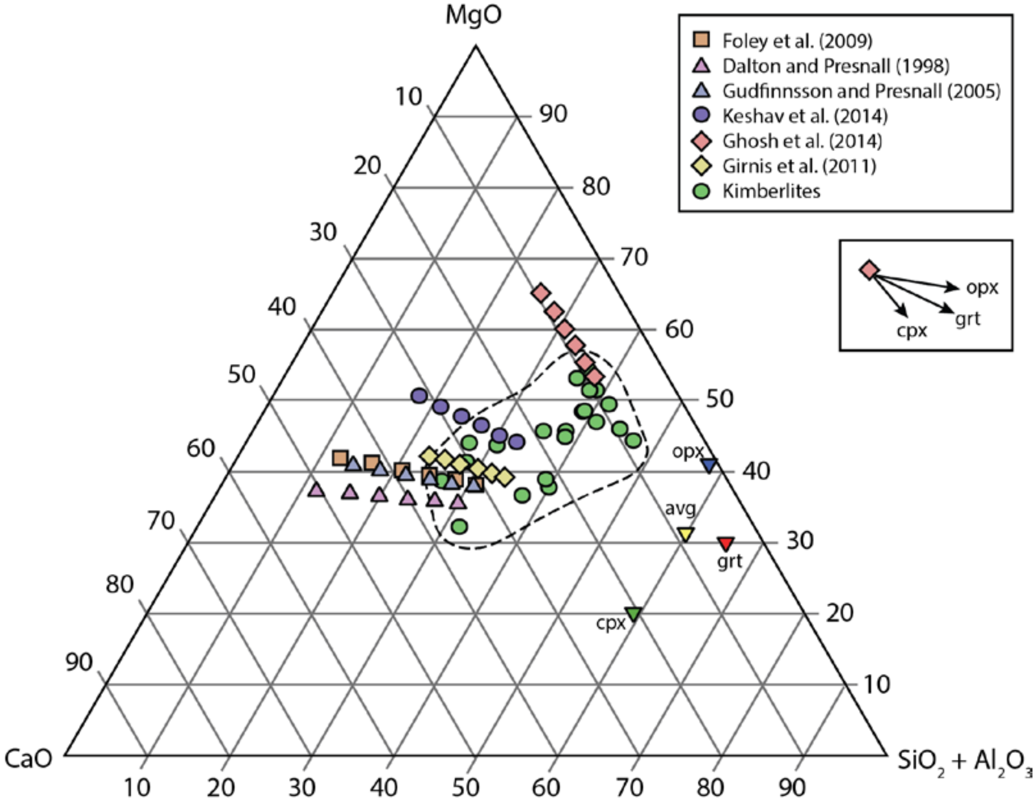

Figure 3.4: The results of the Model II assimilation calculations, showing the assimilation of orthopyroxene, clinopyroxene, and garnet via 0, 10, 20, 30, 40, and 50 wt.% mantle contamination of a xenolith with 25% orthopyroxene, 14% clinopyroxene, and 12% garnet plotted in (MgO) - (CaO) - (SiO_2 + Al_2O_3) compositional space. The yellow inverted triangle represents the weighted average composition of the xenolith.

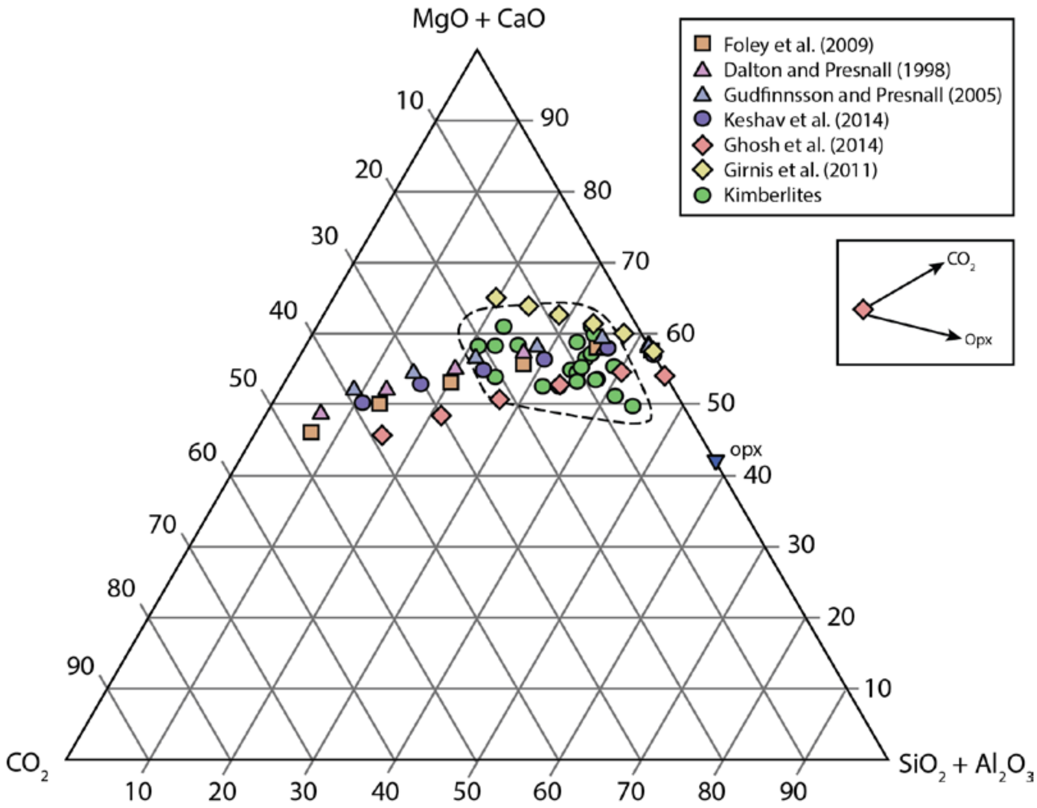

Figure 3.5: Results of Model III assimilation calculations, showing the assimilation of 0, 10, 20, 30, 40, and 50 wt.% orthopyroxene in (MgO + CaO) – (SiO$_2$ + Al$_2$O$_3$) - CO$_2$ compositional space.

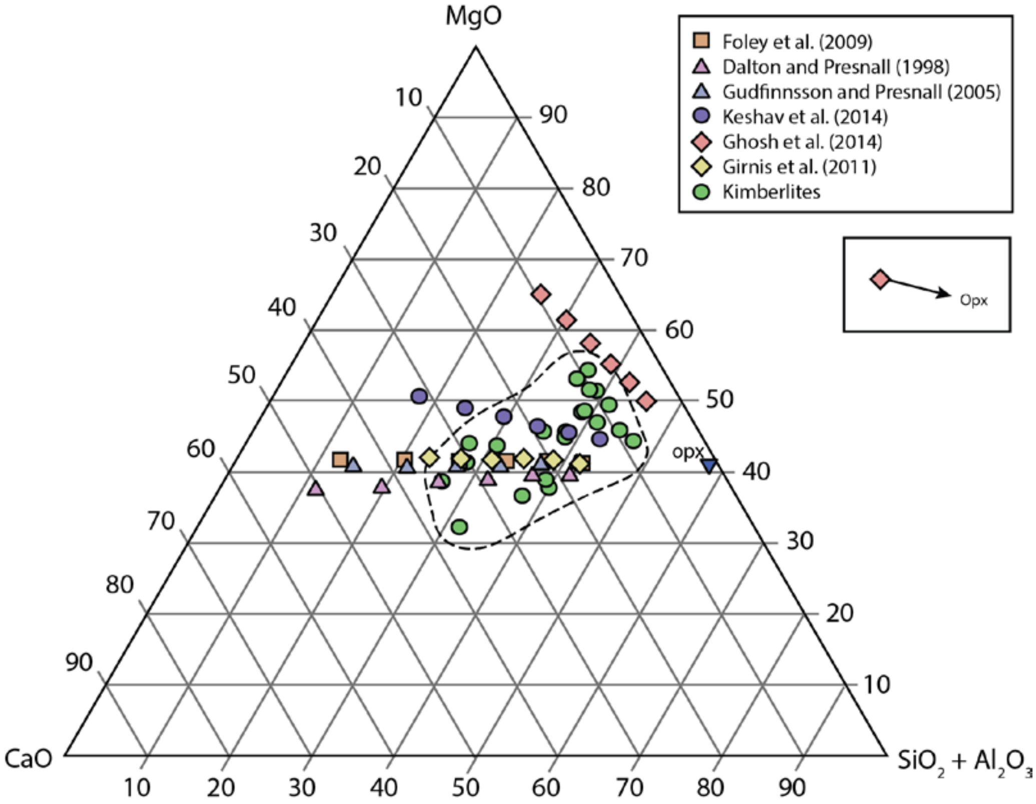

Figure 3.6: Results of Model III assimilation calculations, showing the assimilation of 0, 10, 20, 30, 40, and 50 wt.% orthopyroxene in (MgO) – (CaO) – ($SiO_2 + Al_2O_3$) compositional space.

Chapter 3 Tables:

Table 3.1: Carbonatitic Melt Compositions

Reference	SiO_2	Al_2O_3	MgO*	CaO	Total	CO_2**	$Ca^{\#}$
Foley et al. (2009)	5.23	1.44	22.17	24.04	52.88	47.11	0.52
Dalton and Presnall (1998)	5.86	0.65	20.89	28.02	55.42	44.58	0.57
Gudfinnsson et al. (2005)	8.60	0.34	24.96	27.13	61.03	38.97	0.52
Keshav et al. (2014)	10.21	0.68	31.06	19.23	61.18	38.82	0.38
Ghosh et al. (2014)	14.40	1.12	40.04	5.72	61.28	38.72	0.13
Girnis et al. (2011)	18.46	0.92	18.59	20.53	58.50	10.62	0.52

MgO* = MgO + FeO

** CO_2 was calculated by subtracting the total from 100

Table 3.2: Xenolith Mineralogy and Composition

Garnet lherzolite	Opx	Cpx	Ol	Grt
Mode (%)	24.6	13.7	49.0	12.2
SiO_2	57.35	56.73	41.50	43.26
Al_2O_3	0.73	2.74	-	22.15
MgO*	41.17	19.95	58.73	29.87
CaO	0.76	20.58	-	4.72

MgO* = MgO + FeO

Table 3.3: "Parental" Kimberlite Compositions

Reference	Kimberlite		SiO_2	Al_2O_3	MgO*	CaO	CO_2	$Ca^{\#}$
Kjarsgaard et al. (2009)	Lac de Gras	HL 12-3 (minus 37.6% olivine)	40.09	3.94	41.65	7.96	6.36	0.16
		HL 12-3 (minus 47% peridotite)	37.52	3.71	42.40	8.80	7.57	0.17
		HL10-1B (minus 25.2% olivine)	33.67	3.99	42.77	10.82	8.76	0.20
		HL10-1B (minus 31.5% peridotite)	31.19	3.88	43.71	11.56	9.65	0.21
		HL10-1A (minus 24.0% olivine)	33.94	3.92	42.95	10.61	8.58	0.20
		HL10-1A (minus 30.0% peridotite)	31.51	3.80	43.99	11.29	9.40	0.20
		Leslie B-1 (minus 26.9% olivine)	32.90	2.42	47.73	9.45	7.51	0.17
		Leslie B-1 (minus 33.6% peridotite)	30.76	2.12	48.72	10.09	8.31	0.17
Price et al. (2000)	Jericho	JD51	23.10	2.02	25.63	28.31	20.93	0.52
		JD69	30.16	1.49	31.08	21.63	15.65	0.41
		JD82	31.91	1.83	33.67	18.90	13.68	0.36
		LGS07	36.86	2.31	46.94	8.39	5.50	0.15
	Wesselton		29.60	3.83	43.36	17.69	5.52	0.29
	Leslie		33.05	1.28	51.39	8.44	5.83	0.14
	Dutoitspan		33.34	1.63	46.29	8.39	10.35	0.15
Kopylova et al. (2009)	Jericho	Subsurface	32.23	1.81	40.24	14.57	11.16	0.27
Le Roex et al. (2003)	Kimberley		32.24	2.68	41.97	14.60	8.52	0.26
Harris et al. (2004)	Uintjiesberg		32.51	2.99	33.81	19.51	11.18	0.37
Russell et al. (2012)	Igwisi Hills	BD864*	22.20	3.60	37.20	21.10	15.90	0.36
		BD853*	19.60	3.20	36.90	24.00	16.30	0.39
		BD864**	16.32	4.70	30.73	27.53	20.72	0.47
		BD864***	18.80	4.20	33.70	24.70	18.60	0.42

MgO* = MgO + FeO

* matrix rich magma that has not been modified

** removed 21 wt% mantle olivine from BD864

*** removed 21 wt% mantle olivine and added 10 wt% phenocrystic olivine to BD864

Chapter 4: Conclusions and Future Work

The results from this study show that orthopyroxene assimilation is an integral part of kimberlite formation. The paucity of this mineral in kimberlites can be explained by a decarbonation reaction that results in the crystallization of olivine and diopside and the exsolution of CO_2 which in turn drives the ascent of the kimberlite. At pressures above this decarbonation reaction (> 2.5 GPa), orthopyroxene does not react with the melt. The formation of phenocrystic clinopyroxene in the decarbonation reaction, but its absence in kimberlites at the surface, can be reconciled by a second decarbonation reaction that occurs at lower pressure where clinopyroxene reacts with the melt to produce olivine, calcite, and CO_2. This also provides an explanation why the groundmass carbonate in kimberlite is primarily calcite and not dolomite despite the dolomitic nature of the initial carbonatitic liquids. Xenocrystic clinopyroxene would also take part in this reaction, potentially making it an important secondary mineral in modifying melt composition. Our results differ from the Russell et al. (2012) model in that orthopyroxene assimilation does not commence at greater depths. Immediately after the primary melts leave the source area. Rather, orthopyroxene breakdown and incorporation into the carbonatitic melt does not occur until the orthopyroxene decarbonation reaction at pressure of ~ 2.5 GPa. In addition, their mechanism of orthopyroxene assimilation is different: they proposed that orthopyroxene was assimilated because of the low activity of silica of the melt whereas ours attributes it to a decarbonation reaction involving orthopyroxene as a reactant.

Modeling orthopyroxene and xenolith assimilation models showed that carbonatites and transitional melts cannot evolve to kimberlitic compositions by orthopyroxene assimilation at mantle contamination levels alone. It is possible that more SiO_2-rich carbonatites called transitional melts could evolve to kimberlite compositions by assimilating orthopyroxene, clinopyroxene, garnet via mantle contamination or that carbonatitic melts evolve to kimberlite melts via extensive orthopyroxene assimilation through mantle contamination and wallrock reactions.

The impact of orthopyroxene on the formation of kimberlites was further tested by comparing the SiO_2 content of kimberlites to the amount of orthopyroxene in the surrounding lithosphere using on a number of different scales. The comparisons provide limited support for the hypothesis that orthopyroxene plays an integral role in primary kimberlite melt evolution.

Future work should investigate the effect of using more complex systems in orthopyroxene assimilation experiments by adding components such as H_2O, Na_2O, and FeO that could potentially change the position of the solidus of carbonatite and transitional melts in pressure-temperature space or potentially the behaviour of orthopyroxene in these melts. In addition to orthopyroxene experiments, clinopyroxene reactions with the melt should also be studied to confirm the existence of the decarbonation reaction at lower pressure and to study the amount of CO_2 exsolution that orthopyroxene and diopside assimilation causes in order to model kimberlite melt evolution better. The contributions of garnet and olivine to kimberlite melt formation could also be important and should be studied as well. Further experiments looking at orthopyroxene assimilation at higher pressures and temperatures with various carbonatite and transitional melt compositions could lead to the discovery of other decarbonation reactions that would help with fuelling the ascent of kimberlites at deeper mantle conditions and help further constrain the composition of primary kimberlitic melts.

Appendix:

Appendix 1: Loading Capsules

Table A.1: Loading Capules

Sample #	Capsule	Loaded	Sample	Welded	Loss	Loss in volatiles	% of Starting Material	Opx (g)	Carb	Opx Normalized (%)	Carb
PC-DP-RS-001	0.11064	0.11982	0.00918	0.11954	0.00028	0.00023	2.51				
DPO-RS-002	0.15944	0.17000	0.01056	0.17008	0.00000	0.00000	0.00	0.00329	0.00726	31.16	68.84
DP-RS-005	0.05880	0.06022	0.00142	0.06008	0.00014	0.00007	4.93				
DPO-RS-004	0.05735	0.05945	0.00210	0.05944	0.00001	0.00000	0.00	0.00028	0.00182	13.33	86.67
GP-RS-001	0.05894	0.06095	0.00201	0.06080	0.00015	0.00010	4.98				
K-RS-003	0.05607	0.05864	0.00257	0.05861	0.00003	0.00003	1.17				
KO-RS-001	0.06019	0.06369	0.00350	0.06370	0.00000	0.00000	0.00	0.00037	0.00313	10.57	89.43
G-RS-004	0.06018	0.06328	0.00310	0.06330	0.00000	0.00000	0.00				
GO-RS-002	0.05603	0.06047	0.00444	0.06042	0.00005	0.00005	1.13	0.00057	0.00387	12.84	87.16
G-RS-006	0.06406	0.06783	0.00377	0.06786	0.00000	0.00000	0.00				
GO-RS-003	0.06171	0.06522	0.00351	0.06521	0.00001	0.00001	0.28	0.00026	0.00325	7.41	92.59
C-RS-001	0.05843	0.06020	0.00177	0.06012	0.00008	0.00003	1.69				
OPX-RS-001	0.06260	0.06609	0.00349	0.06601	0.00008	0.00003	0.86	0.00124	0.00225	35.53	64.47
OPX-RS-002	0.05765	0.06095	0.00330	0.06064	0.00031	0.00026	7.88	0.00138	0.00192	41.82	58.18
JD-RS-003	0.05933	0.06147	0.00214	0.06134	0.00013	0.00008	3.74				
MJD-RS-001	0.05512	0.05619	0.00107	0.05616	0.00003	0.00000	0.00				
MMJD-RS-001	0.05822	0.06027	0.00205	0.06028	0.00000	0.00000	0.00				

Appendix 2: Modified Carbonatitic Melts

In order to determine whether orthopyroxene had assimilated into the melt the compositions of the melt for each experiment were compared to that of the starting material. In many cases the starting material did not only form melt, but also a number of other silicates and non-silicate minerals. In these cases, in order to more accurately determine the behaviour of orthopyroxene in the experiment the melt composition was modified for the comparison. The experiments where no additional orthopyroxene was added were modified to include any other silicate or non-silicate minerals present in the melt. The experiments where orthopyroxene was added in addition to carbonatite, all minerals except for orthopyroxene were added to the melt composition. The modes for the melt and minerals were calculated using the program ImageJ and then the modified melts were calculated using the equation:

$$\mathrm{m} = \mathrm{xa} + \mathrm{yb} + \mathrm{zc} \ldots \tag{3}$$

where x, y, and c are the modes of the melt and any additional minerals, while a, b, and c are the concentrations of the component for the melt and the additional minerals. The new modified melts were then re-normalized and the results of which can be found in Table A.2.

The t-tests which will be discussed in Appendix 3 required standard deviations for all the modified melt compositions and therefore the propagated error had to be calculated. This was done using the following equation:

$$\sigma = \sqrt{(\mathrm{xa})^2 + (\mathrm{yb})^2 + (\mathrm{zc})^2 \ldots} \tag{4}$$

where x, y, and z are the modes of the melt and additional minerals and a, b, and c where the standard deviations of each component analysis for the melt and additional minerals. The resulting standard deviations are listed in Table A.2.

Table A.2: Modified Melt Compositions

Experiment		Melt		Forsterite		Garnet		Magnesite		Spinel		Orthopyroxene		Periclase		Coesite		Modified Melt		
		wt%	σ	wt%	σ	wt%	σ	wt%	σ	wt%	σ	wt%	σ	wt%	σ	wt%	σ	wt%	Norm	σ
C-RS-001	mode	0.89		-		-		0.04		-		-		-		0.07				
	SiO_2	7.74	0.52	-	-	-	-	0.04	0.02	-	-	-	-	-	-	98.32	0.39	13.78	13.80	0.46
	Al_2O_3	0.78	0.09	-	-	-	-	0.02	0.01	-	-	-	-	-	-	0.02	0.01	0.70	0.70	0.08
	MgO	25.08	1.49	-	-	-	-	45.63	0.63	-	-	-	-	-	-	0.01	0.01	24.09	24.12	1.33
	CaO	25.98	1.43	-	-	-	-	2.95	0.06	-	-	-	-	-	-	0.02	0.01	23.30	23.33	1.28
	Total	100.00		-	-	-	-	100.01		-	-	-	-	-	-	98.37		99.89	100.00	
	CO_2	40.42	0.91	-	-	-	-	51.37	0.62	-	-	-	-	-	-		0.00	38.01	38.05	0.82
OPX-RS-001	mode	0.95		-		-		0.04	σ	-		-		-		0.01				
	SiO_2	18.56	2.59	-	-	-	-	0.11	0.08	-	-	-	-	-	-	100.09	0.22	18.58	18.58	2.47
	Al_2O_3	1.14	0.09	-	-	-	-	0.03	0.03	-	-	-	-	-	-	0.03	0.01	1.09	1.09	0.08
	MgO	21.82	0.70	-	-	-	-	44.24	1.61	-	-	-	-	-	-	0.01	0.01	22.50	22.50	0.67
	CaO	23.74	0.34	-	-	-	-	2.72	0.19	-	-	-	-	-	-	0.02	0.01	22.70	22.70	0.32
	Total	65.26		-		-	-	47.09		-	-	-	-	-	-	100.15		100.00	100.00	
	CO_2	34.74	3.56	-	-	-	-	52.91	1.70	-	-	-	-	-	-			35.14	35.14	3.38
PC-DP-RS-00	mode	0.97		0.03		-		-		0.001		-		-		-				
	SiO_2	3.67	2.84	42.07	0.21	-	-	-	-	0.40	0.04	-	-	-	-	-	-	4.63	4.63	2.77
	Al_2O_3	0.26	0.16	0.20	0.02	-	-	-	-	68.53	1.62	-	-	-	-	-	-	0.30	0.30	0.16
	MgO	18.94	5.47	56.99	0.42	-	-	-	-	29.74	0.53	-	-	-	-	-	-	19.90	19.90	5.33
	CaO	34.96	5.38	0.34	0.04	-	-	-	-	0.27	0.13	-	-	-	-	-	-	34.07	34.08	5.25
	Total	57.83		99.60		-	-	-	-	98.95		-	-	-	-	-	-	99.99	100.00	
	CO_2	42.17	3.23	0.00		-	-	-	-	0.00		-	-	-	-	-	-	41.09	41.09	3.15
DP-RS-005	mode	0.94		0.05		-		-		0.004		-		0.01		-				
	SiO_2	1.75	0.26	42.60	0.11	-	-	-	-	1.13	0.25	-	-	0.02	0.01	-	-	4.89	4.41	0.25
	Al_2O_3	0.08	0.02	0.12	0.08	-	-	-	-	68.58	0.71	-	-	0.76	0.03	-	-	1.33	1.20	0.02
	MgO	16.06	0.79	57.43	0.32	-	-	-	-	29.63	0.48	-	-	98.30	0.93	-	-	20.63	18.61	0.75
	CaO	38.57	0.77	0.16	0.03	-	-	-	-	0.15	0.05	-	-	0.12	0.05	-	-	39.52	35.66	0.72
	Total	56.47		100.30		-	-	-	-	99.49		-	-	99.20		-	-	110.83	100.00	
	CO_2	43.53	0.33	0.00		-	-	-	-	0.00		-	-	0.00		-	-	44.47	40.13	0.31

Table A.2 Continued: Modified Melt Compositions

Experiment		Melt		Forsterite		Garnet		Magnesite		Spinel		Orthopyroxene		Periclase		Coesite		Modified Melt		
		wt%	σ	wt%	σ	wt%	σ	wt%	σ	wt%	σ	wt%	σ	wt%	σ	wt%	σ	wt%	Norm	σ
DPO-RS-004	mode	1.00		-		0.00		-		-		-		-		-				
	SiO_2	3.20	0.54	-	-	44.31	0.47	-	-	-	-	-	-	-	-	-	-	3.36	3.36	0.54
	Al_2O_3	0.30	0.04	-	-	24.02	0.23	-	-	-	-	-	-	-	-	-	-	0.39	0.39	0.04
	MgO	19.17	0.18	-	-	26.21	0.28	-	-	-	-	-	-	-	-	-	-	19.20	19.20	0.18
	CaO	31.95	0.29	-	-	4.45	0.42	-	-	-	-	-	-	-	-	-	-	31.84	31.84	0.29
	Total	54.63		-	-	98.99		-	-	-	-	-	-	-	-	-	-	99.99	99.99	
	CO_2	45.37	0.43	-	-	0.00		-	-	-	-	-	-	-	-	-	-	45.20	45.20	0.43
K-RS-003	mode	0.95		0.04		0.01		-		-		-		-		-				
	SiO_2	6.13	3.85	42.57	0.21	44.78	0.45	-	-	-	-	-	-	-	-	-	-	7.92	7.92	3.66
	Al_2O_3	0.54	0.38	0.10	0.01	24.04	0.16	-	-	-	-	-	-	-	-	-	-	0.73	0.73	0.36
	MgO	30.10	2.20	56.21	0.49	28.40	0.48	-	-	-	-	-	-	-	-	-	-	31.12	31.14	2.09
	CaO	21.74	2.11	0.09	0.01	1.93	0.07	-	-	-	-	-	-	-	-	-	-	20.70	20.71	2.01
	Total	58.51		98.97		99.15		-	-	-	-	-	-	-	-	-	-	99.95	100.00	
	CO_2	41.49	4.25					-	-	-	-	-	-	-	-	-	-	39.47	39.49	4.05
KO-RS-001	mode	0.73		0.15		0.00		0.12		-		-		-		-				
	SiO_2	5.64	2.29	42.85	0.20	44.48	0.42	0.04	0.01	-	-	-	-	-	-	-	-	10.58	10.58	1.68
	Al_2O_3	0.41	0.21	0.08	0.01	23.49	0.20	0.01	0.01	-	-	-	-	-	-	-	-	0.35	0.35	0.15
	MgO	27.18	1.68	56.72	0.27	28.12	0.31	44.42	0.39	-	-	-	-	-	-	-	-	33.55	33.57	1.23
	CaO	24.53	1.23	0.08	0.01	3.25	0.12	3.62	0.44	-	-	-	-	-	-	-	-	18.46	18.46	0.91
	Total	57.76		99.47		99.33		48.08		-	-	-	-	-	-	-	-	99.96	100.00	
	CO_2	42.24	3.28					51.92	0.30	-	-	-	-	-	-	-	-	37.02	37.03	2.41
G-RS-006	mode	0.89		-		0.01		0.09		-		0.02		-		-				
	SiO_2	12.92	1.14	-	-	45.27	0.12	0.01	0.17	-	-	57.81	0.43	-	-	-	-	12.71	12.72	1.86
	Al_2O_3	1.17	1.02	-	-	24.18	0.01	0.02	0.07	-	-	2.72	0.02	-	-	-	-	1.24	1.24	0.19
	MgO	38.50	0.21	-	-	29.81	0.20	47.01	0.01	-	-	38.39	0.10	-	-	-	-	39.19	39.19	1.01
	CaO	11.41	2.08	-	-	0.83	0.23	1.23	0.01	-	-	0.32	0.90	-	-	-	-	10.27	10.27	0.91
	Total	64.00		-	-	100.10		48.27		-	-	99.25		-	-	-	-	99.99	100.00	
	CO_2	36.00	1.91	-	-			51.73	0.18	-	-			-	-	-	-	36.57	36.58	1.70
GO-RS-003	mode	0.95		-		-		0.05		-		-		-		-				
	SiO_2	14.02	8.53	-	-	-	-	0.01	0.48	-	-	-	-	-	-	-	-	13.26	13.26	5.01
	Al_2O_3	1.36	2.47	-	-	-	-	0.02	0.03	-	-	-	-	-	-	-	-	1.29	1.29	0.34
	MgO	41.46	0.36	-	-	-	-	47.01	0.01	-	-	-	-	-	-	-	-	41.76	41.76	8.07
	CaO	6.72	5.29	-	-	-	-	1.23	0.01	-	-	-	-	-	-	-	-	6.42	6.42	2.34
	Total	63.56		-	-	-	-	48.27		-	-	-	-	-	-	-	-	100.00	100.00	
	CO_2	36.44	2.93	-	-	-	-	51.73	0.50	-	-	-	-	-	-	-	-	37.27	37.27	2.77

Appendix 3: T-tests

The melts from each non-orthopyroxene and orthopyroxene experiment were compared to each other (Table A.3) and then compared to the original starting material composition (Table A.4) using an independent sample t-test. The null hypothesis was that the melts compositions were the same:

$$H_0: \mu_1 = \mu_2 \tag{5}$$

and the alternate hypothesis was that the melts compositions were not equal to each other:

$$H_1: \mu_1 \neq \mu_2 \tag{6}$$

The test statistic used for SiO_2, Al_2O_3, MgO, and CaO was:

$$t^* = \frac{\mu_1 - \mu_2}{\sqrt{\frac{\sigma_1^2}{n_1} + \frac{\sigma_2^2}{n_2}}} \tag{7}$$

And the degrees of freedom (d.f.) was the smaller of $n_1 - 1$ and $n_2 - 1$.

Because the standard deviation for the starting material CO_2 was not reported in the literature the test statistic:

$$t^* = \frac{\mu_1 - \mu_2}{\frac{\sigma_1}{\sqrt{n_1}}} \tag{8}$$

had to be used instead using a d.f. of $n_1 - 1$.

A confidence level of 99% and an α value of 0.01 was used, therefore $t_{0.005}$ (See reference (2015)) was used to determine whether the H_0 was rejected.

Table A.3: One Sample t test α = 0.01, non-orthopyroxene bearing experiment versus

Experiment	PC-DP-RS-001			DPO-RS-002			t*	f (n-1)	$t_{0.005}$	t* > $t_{0.005}$
	n_1	μ_1	σ_1	n_2	μ_2	σ_2				
SiO_2	13	4.63	2.77	15	18.59	3.33	12.111	12	3.055	9.056
Al_2O_3	13	0.30	0.16	15	0.96	0.26	8.124	12	3.055	5.069
MgO	13	19.90	5.33	15	15.83	2.43	2.537	12	3.055	-0.518
CaO	13	34.08	5.25	15	35.26	2.41	0.744	12	3.055	-2.311
CO_2	13	41.09	3.15	15	29.36	2.85	10.276	12	3.055	7.221
Experiment	DP-RS-005			DPO-RS-004						
SiO_2	5	4.41	0.25	20	5.86	0.93	6.159	4	4.604	1.555
Al_2O_3	5	1.20	0.02	20	0.65	0.66	3.714	4	4.604	-0.890
MgO	5	18.61	0.75	20	20.89	1.25	5.235	4	4.604	0.631
CaO	5	35.66	0.72	20	28.02	0.89	20.210	4	4.604	15.606
CO_2	5	40.13	0.31	20	44.58		32.639	4	4.604	28.035
Experiment	K-RS-003			KO-RS-001						
SiO_2	98	7.92	3.66	99	10.58	1.68	6.539	97	2.627	3.913
Al_2O_3	98	0.73	0.36	99	0.35	0.15	9.451	97	2.627	6.824
MgO	98	31.14	2.09	99	33.57	1.23	9.914	97	2.627	7.287
CaO	98	20.71	2.01	99	18.46	0.91	10.113	97	2.627	7.486
CO_2	98	39.49	4.05	99	37.03	2.41	5.182	97	2.627	2.555
Experiment	G-RS-006			GO-RS-003						
SiO_2	100	12.72	1.86	43	13.26	5.01	0.695	42	2.698	-2.003
Al_2O_3	100	1.24	0.19	43	1.29	0.34	0.832	42	2.698	-1.866
MgO	100	39.19	1.01	43	41.76	8.07	2.079	42	2.698	-0.619
CaO	100	10.27	0.91	43	6.42	2.34	10.473	42	2.698	7.775
CO_2	100	36.58	1.70	43	37.27	2.77	1.518	42	2.698	-1.180
Experiment	C-RS-001			OPX-RS-001						
SiO_2	14	13.80	0.46	10	18.58	2.47	6.050	9	3.250	2.800
Al_2O_3	14	0.70	0.08	10	1.09	0.08	11.058	9	3.250	7.808
MgO	14	24.12	1.33	10	22.50	0.67	3.901	9	3.250	0.652
CaO	14	23.33	1.28	10	22.70	0.32	1.773	9	3.250	-1.477
CO_2	14	38.05	0.82	10	35.14	3.38	2.669	9	3.250	-0.580
Experiment	C-RS-001			OPX-RS-002						
SiO_2	14	13.80	0.46	10	16.10	2.37	3.019	9	3.250	-0.231
Al_2O_3	14	0.70	0.08	10	0.92	0.24	2.866	9	3.250	-0.384
MgO	14	24.12	1.33	10	22.45	0.74	3.924	9	3.250	0.674
CaO	14	23.33	1.28	10	23.05	0.47	0.750	9	3.250	-2.500
CO_2	14	38.05	0.82	10	37.48	3.34	0.530	9	3.250	-2.720

Red values reject the null hypothesis

Table A.4: Paired Sample T-tests ($\alpha = 0.01$), experiment versus starting material composition

Experiment		This study			Original Study			t*	d.f.	$t_{0.005}$	$t^* > t_{0.005}$
		n_1	μ_1	σ_1	n_2	μ_2	σ_2				
PC-DP-RS-001	SiO_2	13	4.63	2.77	20	5.86	0.93	1.546	12	3.4284	-1.882
n = 13	Al_2O_3	13	0.30	0.16	20	0.65	0.66	2.282	12	3.4284	-1.147
	MgO	13	19.90	5.33	20	20.89	1.25	0.658	12	3.4284	-2.770
	CaO	13	34.08	5.25	20	28.02	0.89	4.125	12	3.4284	0.697
	CO_2	13	41.09	3.15		44.58		3.994	12	3.4284	0.565
DPO-RS-002	SiO_2	15	18.59	3.33	20	5.86	0.93	14.397	14	3.3257	11.071
	Al_2O_3	15	0.96	0.26	20	0.65	0.66	1.895	14	3.3257	-1.431
	MgO	15	15.83	2.43	20	20.89	1.25	7.366	14	3.3257	4.040
	CaO	15	35.26	2.41	20	28.02	0.89	11.074	14	3.3257	7.749
	CO_2	15	29.36	2.85		44.58		20.681	14	3.3257	17.355
DP-RS-005	SiO_2	5	4.41	0.25	20	5.86	0.93	6.159	4	5.5976	0.561
	Al_2O_3	5	1.20	0.02	20	0.65	0.66	3.714	4	5.5976	-1.883
	MgO	5	18.61	0.75	20	20.89	1.25	5.235	4	5.5976	-0.362
	CaO	5	35.66	0.72	20	28.02	0.89	20.210	4	5.5976	14.613
	CO_2	5	40.13	0.31		44.58		32.639	4	5.5976	27.042
DPO-RS-004	SiO_2	10	3.36	0.54	20	5.86	0.93	9.279	9	3.6896	5.589
	Al_2O_3	10	0.39	0.04	20	0.65	0.66	1.733	9	3.6896	-1.957
	MgO	10	19.20	0.18	20	20.89	1.25	5.935	9	3.6896	2.245
	CaO	10	31.84	0.29	20	28.02	0.89	17.428	9	3.6896	13.738
	CO_2	10	45.20	0.43		44.58		4.557	9	3.6896	0.867
K-RS-003	SiO_2	98	7.92	3.66	35	10.21	2.99	3.650	34	3.0019	0.648
	Al_2O_3	98	0.73	0.36	35	0.68	0.3	0.790	34	3.0019	-2.212
	MgO	98	31.14	2.09	35	31.06	4.01	0.111	34	3.0019	-2.890
	CaO	98	20.71	2.01	35	19.23	2.22	3.480	34	3.0019	0.478
	CO_2	98	39.49	4.05		38.82		1.647	97	2.6275	-0.980
KO-RS-001	SiO_2	99	10.58	1.68	35	10.21	2.99	0.704	34	2.6264	-1.923
	Al_2O_3	99	0.35	0.15	35	0.68	0.3	6.154	34	2.6264	3.528
	MgO	99	33.57	1.23	35	31.06	4.01	3.637	34	2.6264	1.011
	CaO	99	18.46	0.91	35	19.23	2.22	1.983	34	2.6264	-0.643
	CO_2	99	37.03	2.41		38.82		7.387	98	2.6264	4.761
G-RS-006	SiO_2	100	12.72	1.86	7	15.26	2.99	2.221	6	4.3168	-2.095
	Al_2O_3	100	1.24	0.19	7	1.16	0.3	0.709	6	4.3168	-3.607
	MgO	100	39.19	1.01	7	36.49	4.01	1.779	6	4.3168	-2.538
	CaO	100	10.27	0.91	7	6.05	2.22	5.005	6	4.3168	0.688
	CO_2	100	36.58	1.70		41.04		26.193	99	2.6264	23.566
GO-RS-003	SiO_2	43	13.26	5.01	7	15.26	2.99	1.465	6	2.6951	-1.230
	Al_2O_3	43	1.29	0.34	7	1.16	0.3	1.022	6	2.6951	-1.673
	MgO	43	41.76	8.07	7	36.49	4.01	2.699	6	2.6951	0.004
	CaO	43	6.42	2.34	7	6.05	2.22	0.409	6	2.6951	-2.286
	CO_2	43	37.27	2.77		41.04		8.919	42	2.6951	6.224

Table A.4 Continued: Paired Sample T-tests ($\alpha = 0.01$)

Experiment		This study			Original Study			t*	d.f.	$t_{0.005}$	t* > $t_{0.005}$
		n_1	μ_1	σ_1	n_2	μ_2	σ_2				
C-RS-001	SiO_2	14	13.80	0.46	30	13.57	1.1	0.973	13	3.0123	-2.039
	Al_2O_3	14	0.70	0.08	30	0.96	0.1	8.936	13	3.0123	5.923
	MgO	14	24.12	1.33	30	19.42	1.2	11.258	13	3.0123	8.246
	CaO	14	23.33	1.28	30	21.45	0.9	4.956	13	3.0123	1.944
	CO_2	14	38.05	0.82		34.18		17.731	13	3.0123	14.718
OPX-RS-001	SiO_2	10	18.58	2.47	30	13.57	1.1	6.218	9	3.2498	2.968
	Al_2O_3	10	1.09	0.08	30	0.96	0.1	3.912	9	3.2498	0.663
	MgO	10	22.50	0.67	30	19.42	1.2	10.108	9	3.2498	6.858
	CaO	10	22.70	0.32	30	21.45	0.9	6.444	9	3.2498	3.194
	CO_2	10	35.14	3.38		34.18		0.894	9	3.2498	-2.355
OPX-RS-002	SiO_2	10	16.10	2.37	30	13.57	1.1	3.252	9	3.2498	0.002
	Al_2O_3	10	0.92	0.24	30	0.96	0.1	0.461	9	3.2498	-2.789
	MgO	10	22.45	0.74	30	19.42	1.2	9.461	9	3.2498	6.212
	CaO	10	23.05	0.47	30	21.45	0.9	7.198	9	3.2498	3.948
	CO_2	10	37.48	3.34		34.18		3.128	9	3.2498	-0.121

Appendix 4: Orthopyroxene and Xenolith Assimilation Models

The SiO_2, Al_2O_3, MgO, and CaO components of the carbonatitic melts simulated in the orthopyroxene assimilation calculations in Model I were calculated using the following equation:

$$m_x = m * (1 - xy) + x(yo) \tag{9}$$

where m_x is modeled melt composition, m is the original melt composition, x is the percentage of mantle contamination occurring, y is the percentage of orthopyroxene in the xenolith being assimilated, and o is the composition of the orthopyroxene in weight percent in the xenolith.

For xenolith assimilation calculations (Model II), the equation was expanded to:

$$m_x = m * (1 - x(y + c + w)) + x(yo + zc + wg) \tag{10}$$

where z and w are the amounts of clinopyroxene and garnet in the xenolith being assimilated and c and g are the compositions of those minerals in the xenolith respectively.

Orthopyroxene assimilation without the constraint of mantle contamination was calculated using the equation:

$$\mathrm{m_x = m * (1 - y) + yo} \tag{11}$$

where y is the percentage of orthopyroxene being assimilated into the melt.

CO_2 exsolution was modeled using the same equation as Russell et al. (2012) did for their orthopyroxene assimilation equations:

$$W_f = W_i(1 - 2.17w_{opx}) \tag{12}$$

where W_f is the volatile content are after CO_2 exsolution has occurred, W_i is the original CO_2 starting material, and w_{opx} is the weight fraction of orthopyroxene being assimilated.

Once both the orthopyroxene assimilation and the CO_2 exsolution were calculated SiO_2, Al_2O_3, MgO*, and CaO were renormalized to a total of 100 – W_f. The resulting melt compositions from these models can be found in Tables A.5 – A.7.

Table A.5: Orthopyroxene Assimilation based off the Mantle Contamination Observed in Kimberlites

Mantle Contamination		0	10	20	30	40	50
Opx Assimilation		0	2.46	4.92	7.38	9.84	12.30
Foley et al. (2009)	SiO_2	5.23	6.68	8.18	9.73	11.34	12.99
	Al_2O_3	1.44	1.46	1.48	1.49	1.50	1.51
	MgO*	22.17	23.20	24.24	25.27	26.31	27.34
	CaO	24.04	24.06	24.02	23.94	23.80	23.63
	CO_2	47.11	44.60	42.08	39.57	37.05	34.54
Girnis et al. (2011)	SiO_2	18.46	19.51	20.58	21.65	22.73	23.82
	Al_2O_3	1.31	1.30	1.29	1.29	1.28	1.27
	MgO*	35.90	36.22	36.53	36.84	37.16	37.47
	CaO	29.22	28.66	28.10	27.53	26.95	26.36
	CO_2	15.11	14.31	13.50	12.69	11.89	11.08
Dalton and Presnall (1998)	SiO_2	5.86	7.29	8.77	10.29	11.86	13.48
	Al_2O_3	0.65	0.67	0.68	0.70	0.71	0.73
	MgO*	20.89	21.87	22.86	23.85	24.85	25.85
	CaO	28.02	27.97	27.87	27.71	27.51	27.26
	CO_2	44.58	42.20	39.82	37.44	35.06	32.68
Gudfinnson and Presnall (2005)	SiO_2	8.60	9.98	11.39	12.84	14.32	15.84
	Al_2O_3	0.34	0.36	0.37	0.39	0.40	0.42
	MgO*	24.96	25.82	26.68	27.53	28.39	29.25
	CaO	27.13	26.96	26.75	26.51	26.23	25.92
	CO_2	38.97	36.89	34.81	32.73	30.65	28.57
Keshav et al. (2014)	SiO_2	10.21	11.57	12.97	14.41	15.87	17.36
	Al_2O_3	0.68	0.69	0.71	0.72	0.73	0.74
	MgO*	31.06	31.87	32.68	33.47	34.26	35.04
	CaO	19.23	19.11	18.97	18.80	18.61	18.39
	CO_2	38.82	36.75	34.68	32.60	30.53	28.46
Ghosh et al. (2014)	SiO_2	14.40	15.74	17.10	18.49	19.91	21.35
	Al_2O_3	1.12	1.13	1.14	1.15	1.15	1.16
	MgO*	40.04	40.78	41.51	42.21	42.90	43.57
	CaO	5.72	5.70	5.67	5.63	5.59	5.54
	CO_2	38.72	36.65	34.59	32.52	30.45	28.38

MgO* = MgO + FeO

Table A.6: Orthopyroxene, Clinopyroxene, and Garnet Assimilation based of the Mantle Contamination Observed in Kimberlites

Mantle Contamination		0	10	20	30	40	50
Opx Assimilation		0	2.46	4.92	7.38	9.84	12.30
Cpx Assimilation		0	1.37	2.74	4.11	5.48	6.85
Grt Assimilation		0	1.22	2.44	3.55	4.88	6.10
Foley et al. (2009)	SiO_2	5.23	7.70	10.18	12.67	15.17	17.67
	Al_2O_3	1.44	1.70	1.96	2.21	2.47	2.73
	MgO*	22.17	22.76	23.34	23.92	24.50	25.08
	CaO	24.04	23.25	22.44	21.62	20.80	19.97
	CO_2	47.11	44.60	42.08	39.57	37.05	34.54
Girnis et al. (2011)	SiO_2	18.46	20.25	22.05	23.84	25.64	27.44
	Al_2O_3	1.31	1.57	1.83	2.09	2.35	2.61
	MgO*	35.90	35.76	35.61	35.47	35.32	35.18
	CaO	29.22	28.11	27.01	25.90	24.80	23.69
	CO_2	15.11	14.31	13.50	12.69	11.89	11.08
Dalton and Presnall (1998)	SiO_2	5.86	8.30	10.75	13.20	15.66	18.13
	Al_2O_3	0.65	0.94	1.24	1.54	1.84	2.13
	MgO*	20.89	21.53	22.18	22.82	23.46	24.10
	CaO	28.02	27.02	26.02	25.00	23.98	22.95
	CO_2	44.58	42.20	39.82	37.44	35.06	32.68
Gudfinnson and Presnall (2005)	SiO_2	8.60	10.90	13.21	15.52	17.84	20.17
	Al_2O_3	0.34	0.65	0.96	1.27	1.58	1.90
	MgO*	24.96	25.40	25.83	26.26	26.69	27.12
	CaO	27.13	26.16	25.19	24.22	23.23	22.25
	CO_2	38.97	36.89	34.81	32.73	30.65	28.57
Keshav et al. (2014)	SiO_2	10.21	12.43	14.66	16.89	19.13	21.38
	Al_2O_3	0.68	0.97	1.27	1.56	1.86	2.15
	MgO*	31.06	31.20	31.33	31.46	31.59	31.72
	CaO	19.23	18.65	18.07	17.48	16.89	16.29
	CO_2	38.82	36.75	34.68	32.60	30.53	28.46
Ghosh et al. (2014)	SiO_2	14.40	16.42	18.44	20.47	22.50	24.54
	Al_2O_3	1.12	1.39	1.66	1.94	2.21	2.48
	MgO*	40.04	39.74	39.43	39.12	38.80	38.48
	CaO	5.72	5.80	5.88	5.96	6.04	6.12
	CO_2	38.72	36.65	34.59	32.52	30.45	28.38

MgO* = MgO + FeO

Table A.7: Extensive Orthopyroxene Assimiation Calculations

Opx Assimilation		0	10	20	30	40	50
Foley et al. (2009)	SiO_2	5.23	11.44	18.43	26.02	34.09	40.93
	Al_2O_3	1.44	1.50	1.53	1.53	1.51	1.42
	MgO*	22.17	26.37	30.56	34.75	38.92	41.43
	CaO	24.04	23.79	22.82	21.27	19.26	16.22
	CO_2	47.11	36.89	26.67	16.44	6.22	0.00
Girnis et al. (2011)	SiO_2	18.46	22.80	27.29	31.91	36.66	41.00
	Al_2O_3	1.31	1.28	1.24	1.20	1.16	1.10
	MgO*	35.90	37.18	38.44	39.71	40.97	41.69
	CaO	29.22	26.91	24.47	21.90	19.22	16.21
	CO_2	15.11	11.83	8.55	5.27	1.99	0.00
Dalton and Presnall (1998)	SiO_2	5.86	11.97	18.78	26.15	33.99	40.67
	Al_2O_3	0.65	0.71	0.77	0.83	0.87	0.89
	MgO*	20.89	24.91	28.99	33.11	37.26	39.93
	CaO	28.02	27.50	26.23	24.35	21.99	18.51
	CO_2	44.58	34.91	25.23	15.56	5.88	0.00
Gudfinnson and Presnall (2005)	SiO_2	8.60	14.42	20.78	27.59	34.79	40.95
	Al_2O_3	0.34	0.41	0.47	0.54	0.61	0.66
	MgO*	24.96	28.45	31.94	35.43	38.93	41.07
	CaO	27.13	26.21	24.75	22.83	20.53	17.32
	CO_2	38.97	30.51	22.06	13.60	5.14	0.00
Keshav et al. (2014)	SiO_2	10.21	15.97	22.23	28.91	35.95	41.92
	Al_2O_3	0.68	0.73	0.78	0.82	0.86	0.87
	MgO*	31.06	34.31	37.44	40.47	43.42	44.81
	CaO	19.23	18.60	17.58	16.25	14.64	12.40
	CO_2	38.82	30.40	21.97	13.55	5.12	0.00
Ghosh et al. (2014)	SiO_2	14.40	20.00	26.01	32.37	39.04	44.49
	Al_2O_3	1.12	1.15	1.18	1.19	1.19	1.14
	MgO*	40.04	42.94	45.55	47.91	50.05	50.35
	CaO	5.72	5.59	5.35	5.02	4.62	4.02
	CO_2	38.72	30.32	21.91	13.51	5.11	0.00

MgO* = MgO + FeO

Appendix 5: The Relationship between Kimberlite Whole Rock Chemistry and Craton Petrology

A.5.1 Introduction

In conjunction with the modeling exercises in Chapter 3, we also looked into the relationship between the SiO_2 content of kimberlites and the petrology of the craton hosting the kimberlite to test the hypothesis that orthopyroxene assimilation has a major effect on the SiO_2 content in kimberlites. The amount of orthopyroxene in the mantle varies from craton to craton, with the North American craton (Greenland) having the lowest (0 - 15 wt.%) (Bernstein et al., 2006; Bizzarro and Stevenson, 2003; Wittig et al., 2008) and the Kaapvaal (Southern Africa) and Sino-Korean (China) cratons having the highest, approximately 20 - 35 wt.% (Maier et al., 2012; Simon et al., 2007; Zheng et al., 2006). If orthopyroxene assimilation has a large impact on primary kimberlite melt evolution then there should be a relationship between the SiO_2 content of the kimberlite and the amount of orthopyroxene in the underlying mantle. This analysis should help further understand the role orthopyroxene plays in kimberlite melt evolution.

A.5.2 Methods:

Professor Graham Pearson provided the same kimberlite database that was used by Kjarsgaard et al. (2009). The database was updated with additional data that was not originally included in the 2009 study or that were published subsequently for kimberlites from the Greenland from studies in the literature (Emeleus and Andrews, 1975; Gaffney et al., 2007; Larsen and Rex, 1992; Tappe et al., 2011; Thy et al., 1987).

Any crustal contamination will strongly affect SiO_2 and therefore the data had to be assessed for this possibility before the relationships with the cratonic mantle could be evaluated. The kimberlites were filtered using the same techniques as Kjarsgaard et al. (2009), who used ln(Mg/Yb) versus ln(Si/Al), Al_2O_3 versus Yb plots, and C.C.I. versus ln(Si/Al) plots for screening for crustal contamination. The abundance of Yb and Al_2O_3 are much higher in the crust than in the mantle, therefore kimberlites that are crustally contaminated should show elevated Yb and Al_2O_3 concentrations relative to those that are not contaminated. The Clement Contamination Index is used to filter rocks without relying on petrological evidence of crustal contamination. Traditionally, any C.C.I. value above 1 is considered contaminated, but this rule should be treated with caution because in some cases uncontaminated kimberlites can have C.C.I. value as high as 1.5 (Clement, 1982; Kjarsgaard et al., 2009). However when no Yb data is available for a kimberlite, it was necessary to use this screen. When dealing with compositional data, using logarithms of ratios minimized the effects of closure, which are significant with major element data (Kjarsgaard et al., 2009).

The data was first filtered using the ln(Mg/Yb) versus ln(Si/Al) because it showed the clearest bimodality between the contaminated and uncontaminated kimberlites, with the contaminated having the lower values. The Al_2O_3 vs Yb plot as used as a secondary filter to help further discern the contamination for more ubiquitous plot points. In case where no Yb data was available, the C.C.I. versus ln(Si/Al) plot was used to filter the data.

Once the data was filtered, the kimberlite SiO_2 contents were then plotted against the ln(MgO/SiO_2) for the corresponding xenoliths from a database also provided by Professor Pearson, compiled from numerous different studies (Table A.8) (Bizzarro and Stevenson, 2003; Boyd et al., 2004; Boyd et al., 1997; Ionov et al., 2010; Irvine et al., 2003; Janney et al., 2010; Kopylova et al., 1999; Maier et al., 2012; Nixon et al., 1981; Pearson et al., 2004; Schmidberger and Francis, 1999; Simon et al., 2007; Wittig et al., 2008; Zheng et al., 2007). The ratio of MgO/SiO_2 acts as a measure of how much orthopyroxene is in the xenolith assemblage. The ratio of MgO to SiO_2 is 1:1

for enstatite and 2:1 for forsterite; therefore the lower the ratio (the more SiO_2 rich) the more orthopyroxene is present. Clinopyroxene and garnet can also affect the MgO/SiO_2 ratio. Pyropic garnet, which has the same ratio of MgO/SiO_2 as orthopyroxene would have the same affect. Diopside has a lower ratio of MgO/SiO_2 of 1:2 would cause the bulk rock ratio to decrease even further. To explore the relationship between three plots were made: one comparing the average kimberlite SiO_2 content to the average xenolith $\ln(MgO/SiO_2)$ for each craton, another comparing the average xenolith $\ln(MgO/SiO_2)$ to each individual kimberlite SiO_2 content for each craton in order to show the range of SiO_2 contents in the data, and finally, a comparison of the average SiO_2 content for kimberlites in a single locality (e.g. Jagersfontein, Premier, Jericho etc.) to an average xenolith $\ln(MgO/SiO_2)$ found in the same area.

A.5.3 Results

A.5.3.1 Filters to screen out crustal contamination

Figures A.1 – A.15 show the filtered data for kimberlites from the Lac de Gras field on the Slave craton and the Somerset Island kimberlites on the Rae craton in Canada (Figures A.1 – A.3), the Kaapvaal craton (Figures A.4 – A.6) and kimberlites adjacent to the Kaapvaal (Figures A.7 – A.9) in southern Africa, kimberlites on the North American craton in Greenland (Figures A.10 – A.12), and kimberlites from China (Sino-Korean craton) and Russia (Udachnaya) (Figures A.13- A.15). The bimodality between the contaminated and uncontaminated kimberlite groups showed up the clearest on the ln(Mg/Yb) versus ln(Si/Al) plots (Figures A.2, A.5, A.8, A.11, and A.14), with uncontaminated kimberlites plotting at higher ln(Mg/Yb) values (indicating elevated concentrations of Yb) than the uncontaminated kimberlites and equal or higher values of ln(Si/Al). The division between contaminated and uncontaminated kimberlites was not as definitive on the Al_2O_3 versus Yb and

C.C.I. versus ln(Si/Al) plots. Though uncontaminated kimberlites usually have a higher ln(Si/Al) values than contaminated values, there was an significant overlap between the two groups (Figures A.1, A.4, A.7, A.10, and A.13). The contaminated kimberlites ranged from Yb poor and Al_2O_3 rich to Yb rich and Al_2O_3 rich to Yb rich and Al_2O_3 poor on the Al_2O_3 versus Yb plots (Figures A.3, A.6, A.9, A.12, and A.15). Some data points that were easily distinguishable as contaminated or uncontaminated on the ln(Mg/Yb) versus ln(Si/Al) plot cause some overlap between the two groups on the Al_2O_3 versus Yb plot. All the localities except for the North American Craton (Greenland) had contaminated kimberlites.

A.5.3.2 Kimberlite – Craton Comparison

Figures A.16 to A.18 show the comparisons between kimberlite SiO_2 content and craton orthopyroxene content as represented by the ln(MgO/SiO_2) proxy. Figure A.16, a comparison of overall averages for both values for each craton (Table A.8) shows that there is a moderate correlation, with an R^2 value of 0.587. The Sino-Korean craton (China) has the highest ln(MgO/SiO_2) value and SiO_2 kimberlite content (~ 33.3 wt.%) whereas Greenland has the lowest ln(MgO/SiO_2) and SiO_2 content (~ 27.5 wt.%). The rest of the cratons cluster around the center of the point between the China and Greenland craton data points, with Slave having the highest SiO_2 kimberlite content followed by S.A., Udachnaya, off S.A., and finally Somerset Island. The Kaapvaal craton and off Kaapvaal average xenolith ln(MgO/SiO_2) is below 0 (more orthopyroxene rich) and Slave, S.I., and Udachnaya have average xenolith ln(MgO/SiO_2) above 0 (more orthopyroxene poor).

Figure A.17 shows the same data set as Figure A.16, but with each individual kimberlite analyses plotted. This reveals the large variation of SiO_2 content for each craton, the largest of which is for the Kaapvaal craton (~ 22 – 37 wt.%) and the lowest is for the Sino-Korean craton (~ 29 – 35.5 wt.%).

Figure A.18 focuses on local correlations between kimberlite SiO_2 and xenolith ln(MgO/SiO_2); the locations and their respective cratons are listed in Table A.9. The relationship between xenolith ln(MgO/SiO_2) and kimberlite SiO_2 concentration is still weakly present, but the R^2 value has dropped to 0.2238. The kimberlites from the North American craton (Greenland) have the lowest kimberlite SiO_2 contents and the highest ln(MgO/SiO_2) values (low orthopyroxene content), same as in the previous two diagrams. The data from Kaapvaal is more spread out ranging from 28 - 35 SiO_2 (wt.%) and ln(MgO/SiO_2 values) of approximately 0.5 to -0.18. The kimberlites from the off the Kaapvaal craton ranging widely in kimberlite SiO_2 composition (26 – 33.5 wt.%), but have a fairly constant ln(MgO/SiO_2) (-0.5 to 0). The two values representing kimberlites from the Sino-Korean craton also show varying SiO_2 content despite a fairly similar ln(Mg/SiO_2) values. Only one data point was available for each of the Slave, Rae, and Russian cratons; the plotted values were similar to those seen in Figure A.16. The amount of data is smaller than the previous graphs because matching xenolith and kimberlite data sets are not abundant.

A.5.4 Discussion and Conclusion:

The comparison at two different scales, craton and kimberlite field, has shown that orthopyroxene assimilation does play a part in the evolution of kimberlite melts during ascent, but the comparisons between xenoliths and kimberlite content at the kimberlite field level demonstrates that orthopyroxene assimilation is not the only process affecting primary kimberlite melt evolution. There are a couple of reasons why the correlation between kimberlite SiO_2 and the orthopyroxene content in the mantle is not stronger. One is that the ln(MgO/SiO_2) is also affected by the amount of clinopyroxene and garnet. Another is that as found in Chapter 3, the starting composition of the primary kimberlite melt can range in composition. Therefore two kimberlites in the same area being contaminated with the same amount of orthopyroxene can yield different SiO_2 values, explaining the data variance in Figure A.17. It is also possible that clinopyroxene and olivine are assimilating increasing the SiO_2 content of the melt. Therefore orthopyroxene assimilation is one of many influences on kimberlite melt compositions, but is an important influence nonetheless. Despite these variations, these comparisons are consistent with orthopyroxene having an effect on the evolution of the primary kimberlite melt composition during ascent.

A.5 Figures**:**

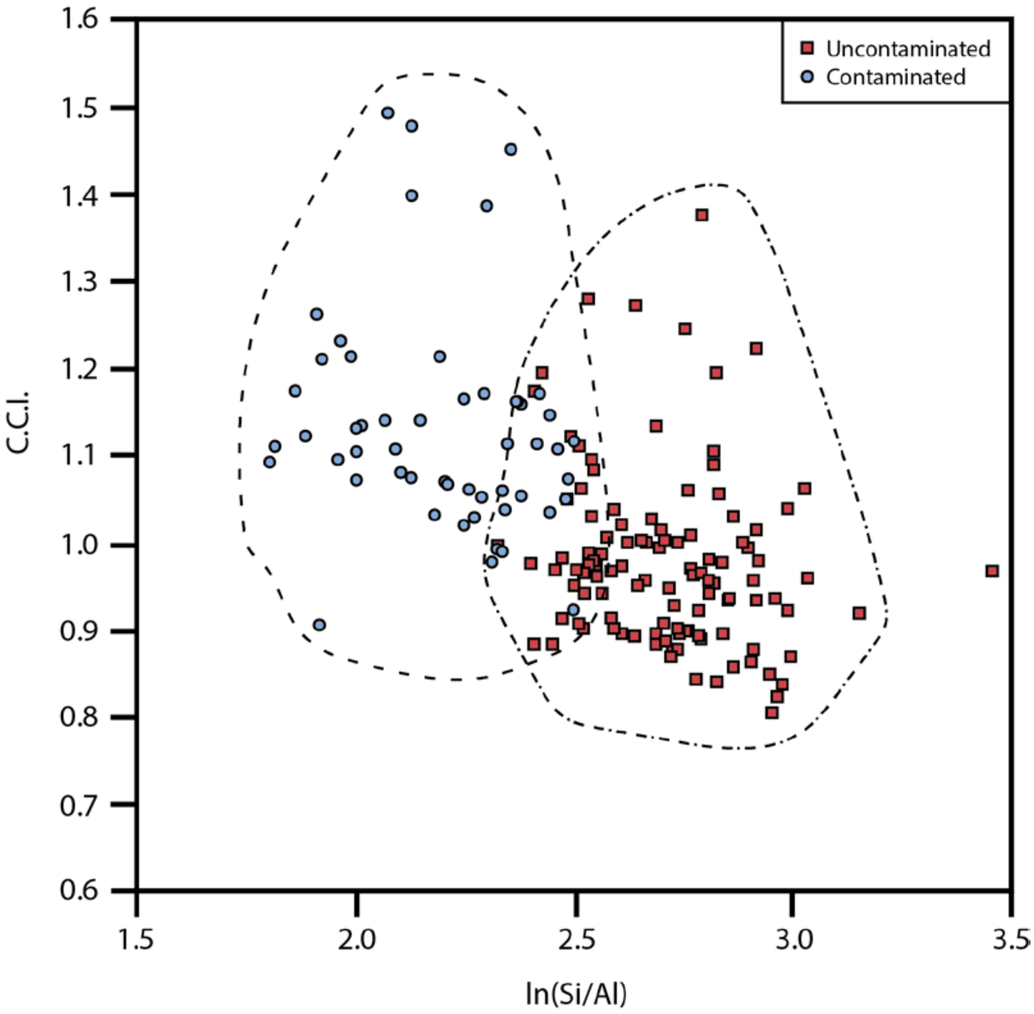

Figure A.1: Data from the Rae and Slave cratons filtered using the Clement Contamination Index and the natural log of Si/Al. C.C.I. values above 1 are usually considered contaminated.

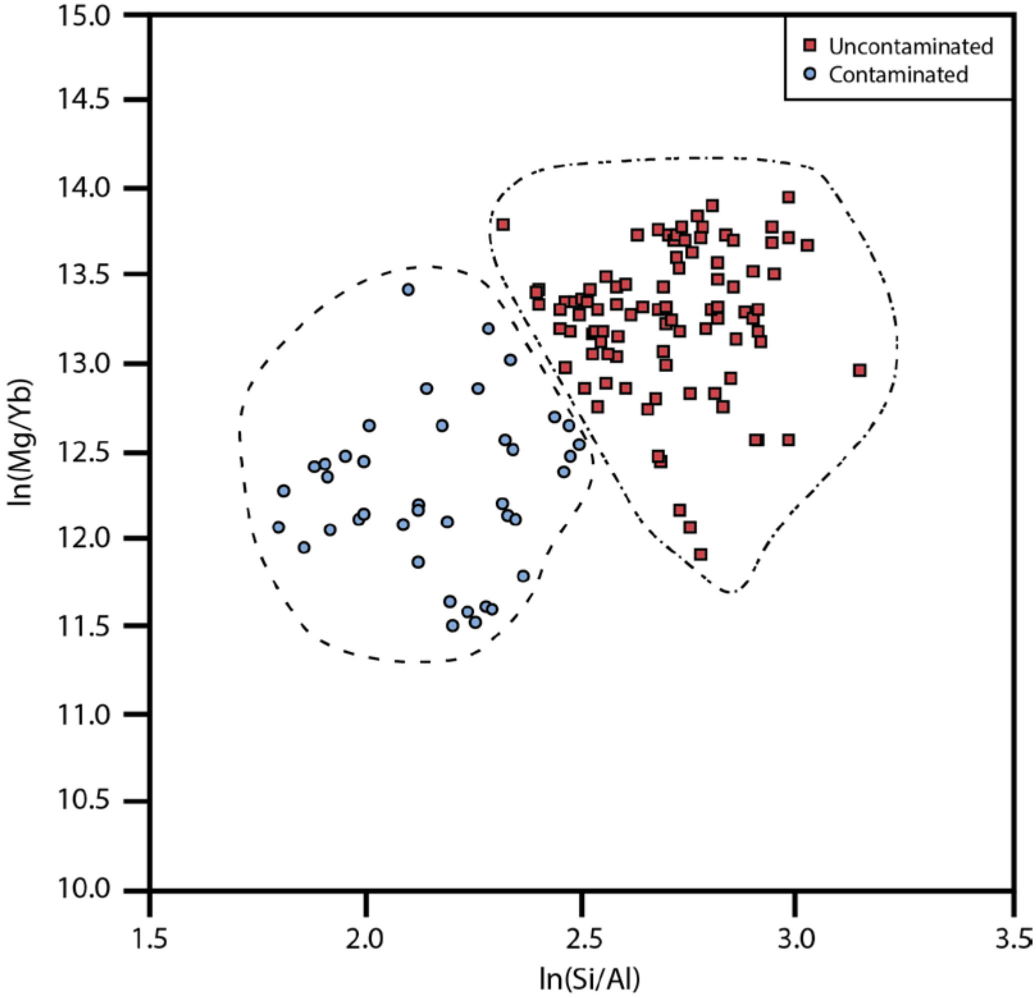

Figure A.2: A contamination filter using ln(Mg/Yb) versus ln(Si/Al) to separate contaminated and uncontaminated kimberlites for the Slave and Rae cratons.

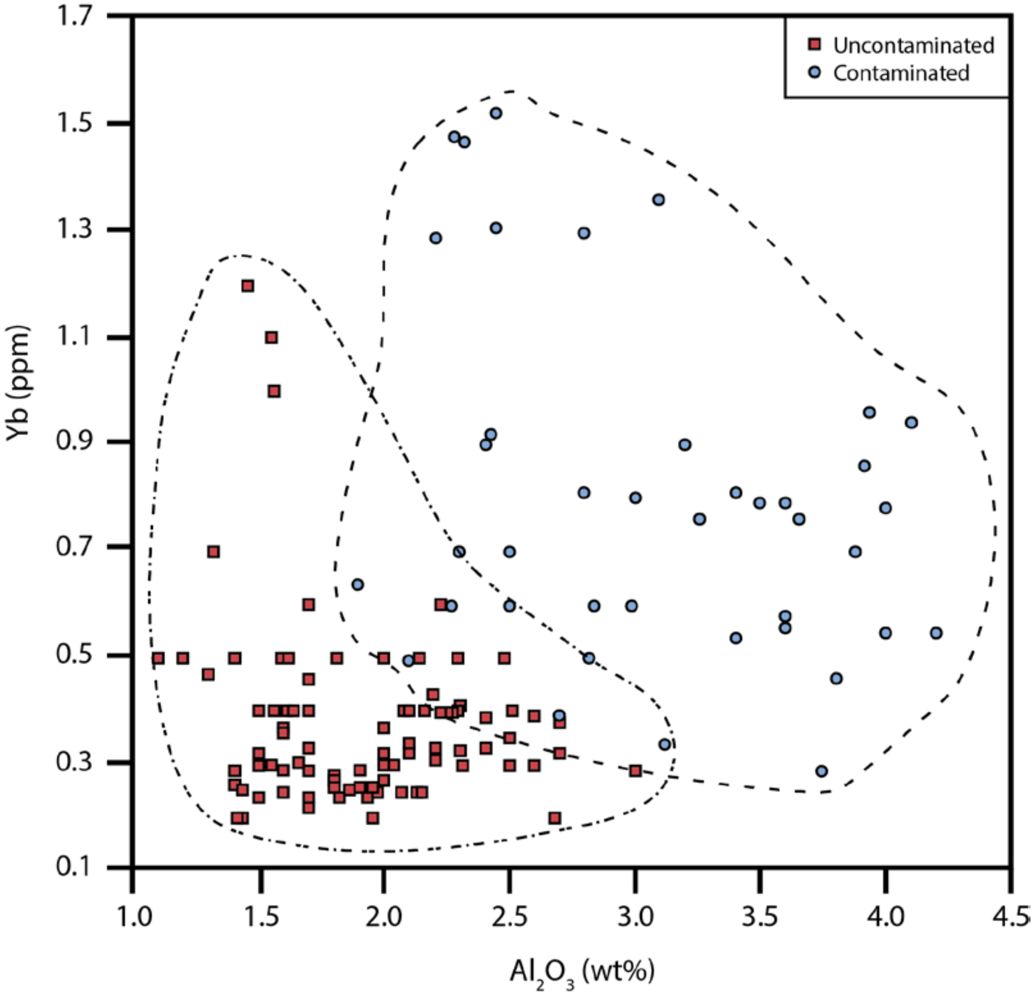

Figure A.3: An Al_2O_3 versus Yb plot filtering kimberlites from the Slave and Rae cratons.

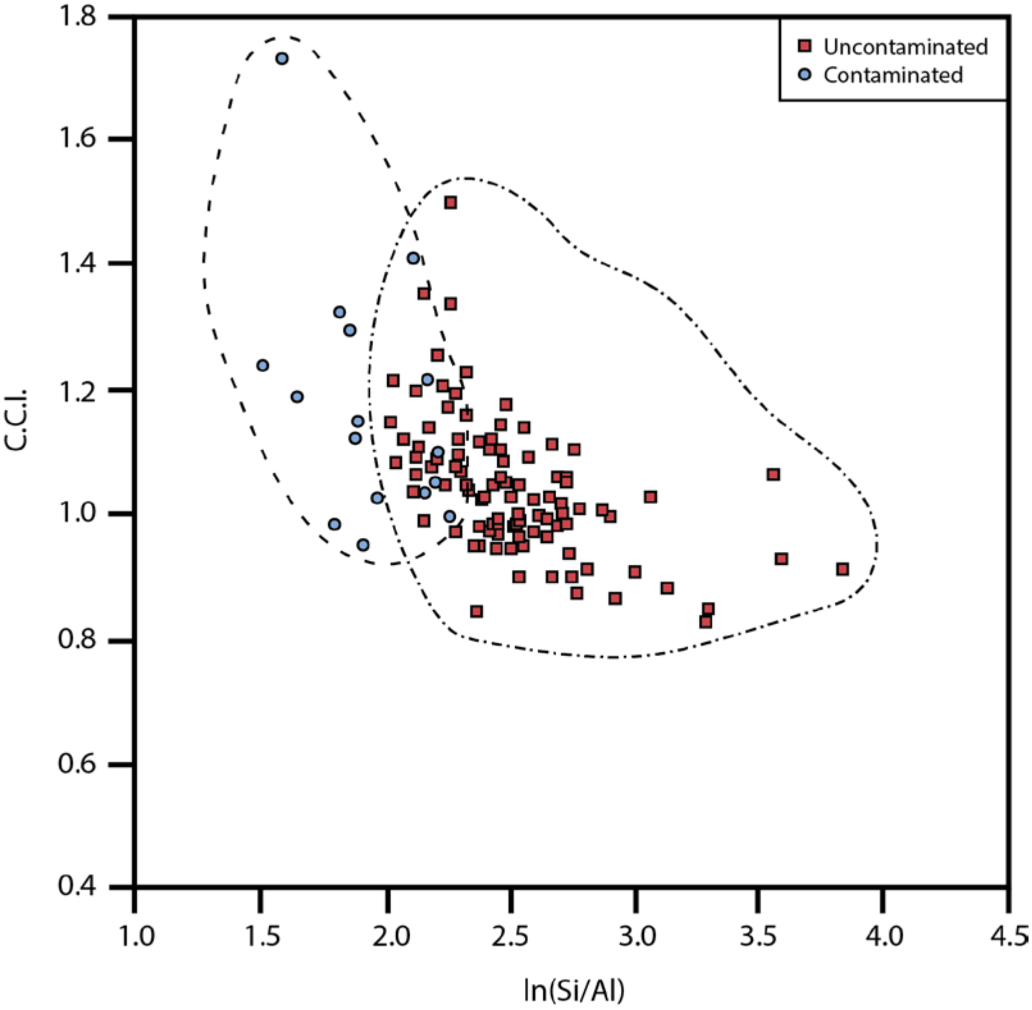

Figure A.4: A C.C.I. versus ln(Si/Al) filter for the Kaapvaal craton kimberlites.

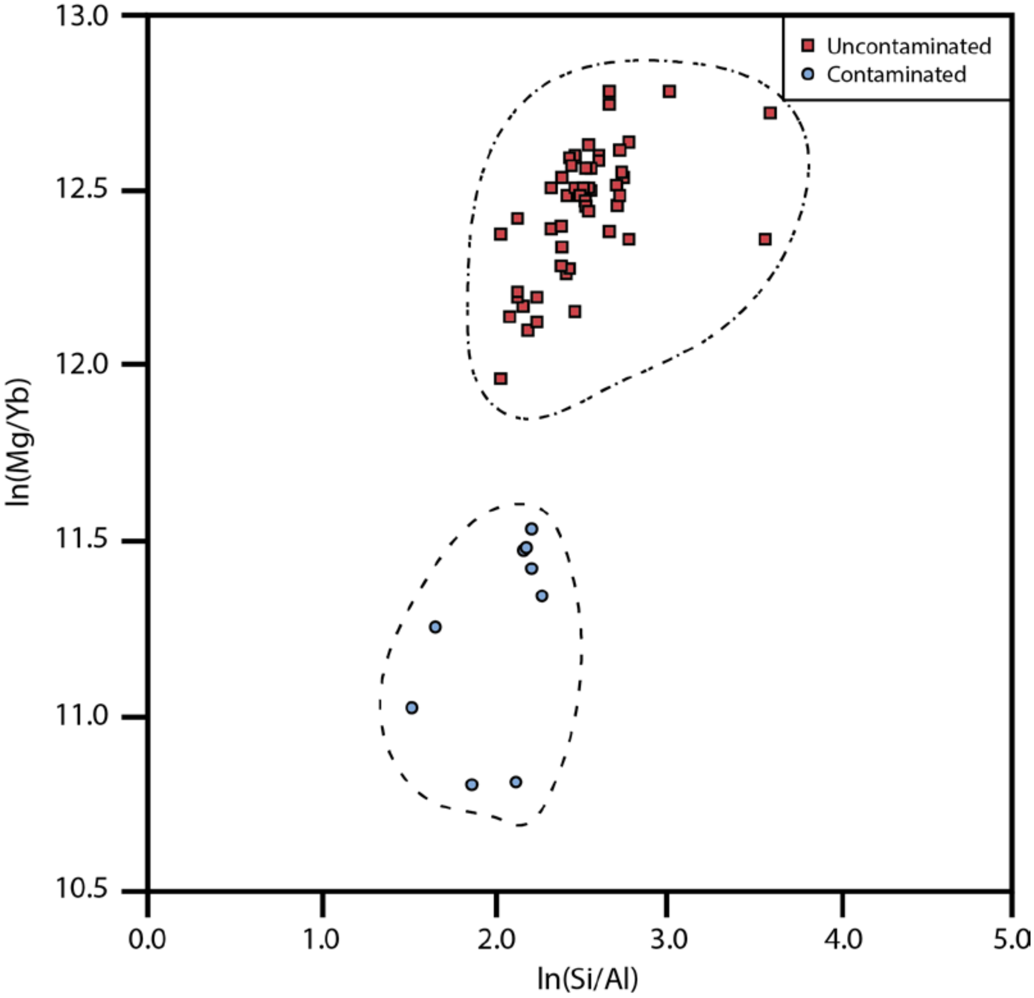

Figure A.5: A ln(Mg/Si) versus ln(Si/Al) filter for kimberlites from the Kaapvaal craton.

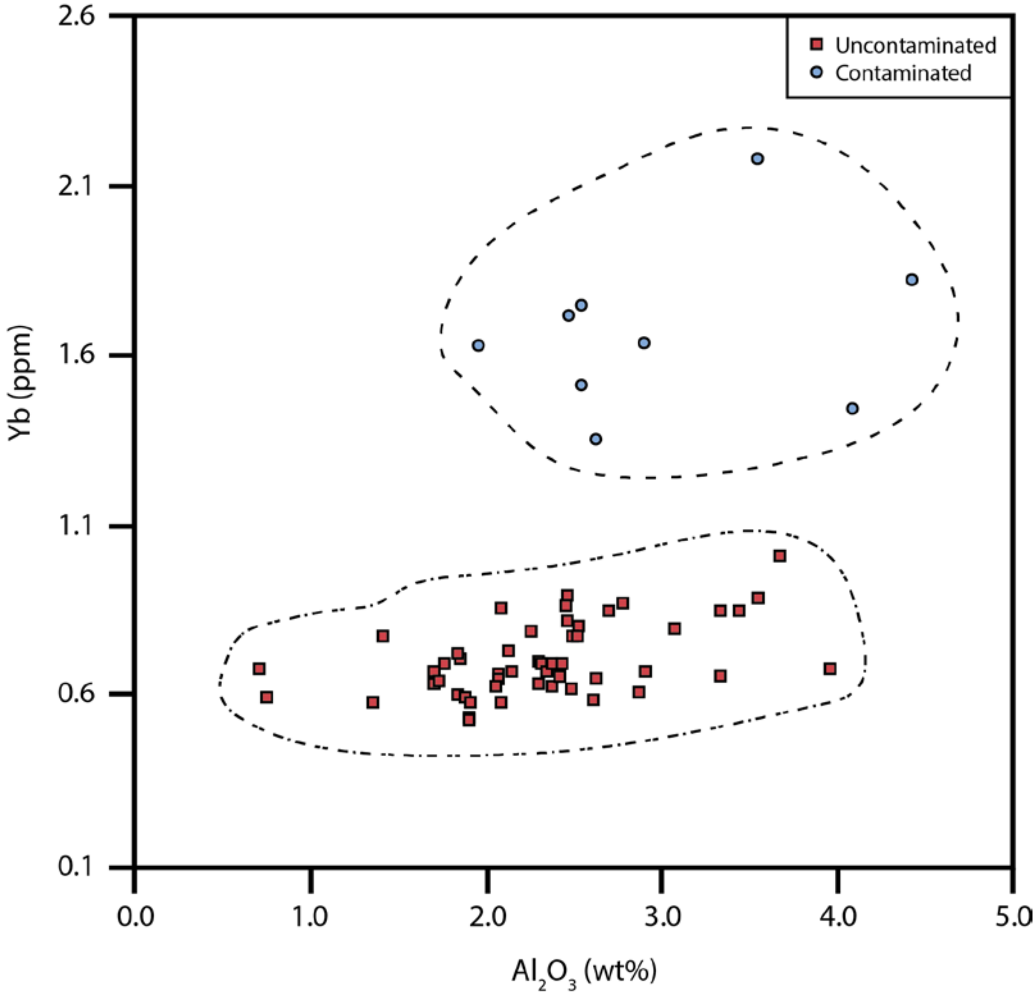

Figure A.6: An Al_2O_3 versus Yb filter for kimberlites from the Kaapvaal craton

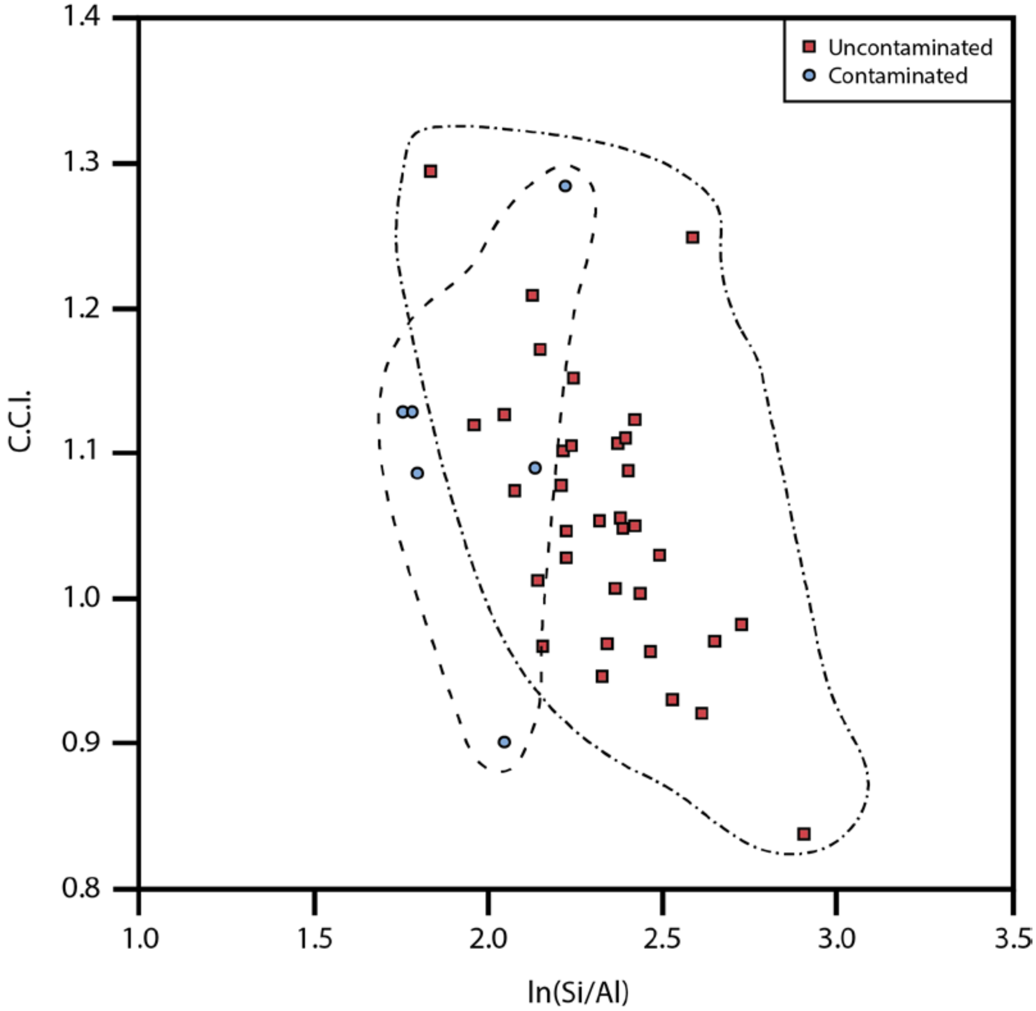

Figure A.7: A C.C.I versus ln(Si/Al) filter for kimberlites just off the Kaapvaal craton.

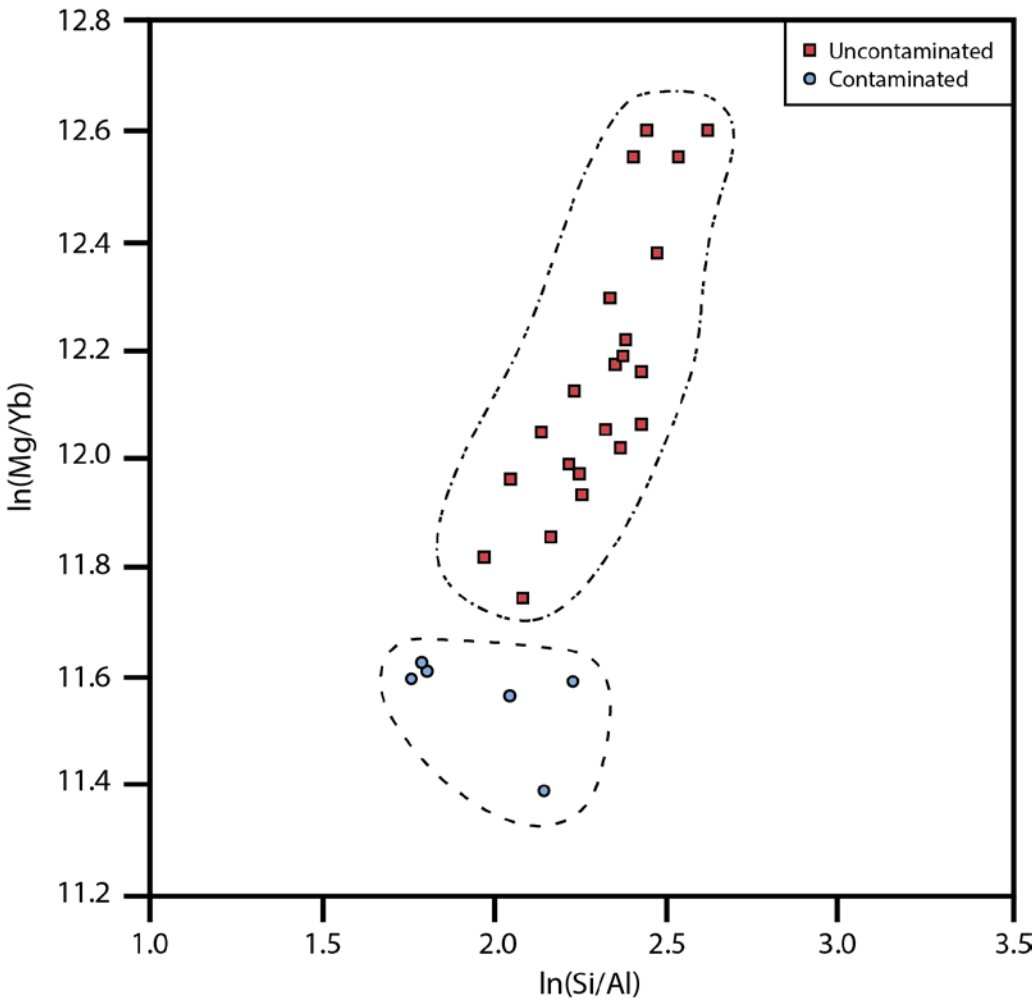

Figure A.8: A ln(Mg/Si) versus ln(Si/Al) filter for kimberlites just off the Kaapvaal craton.

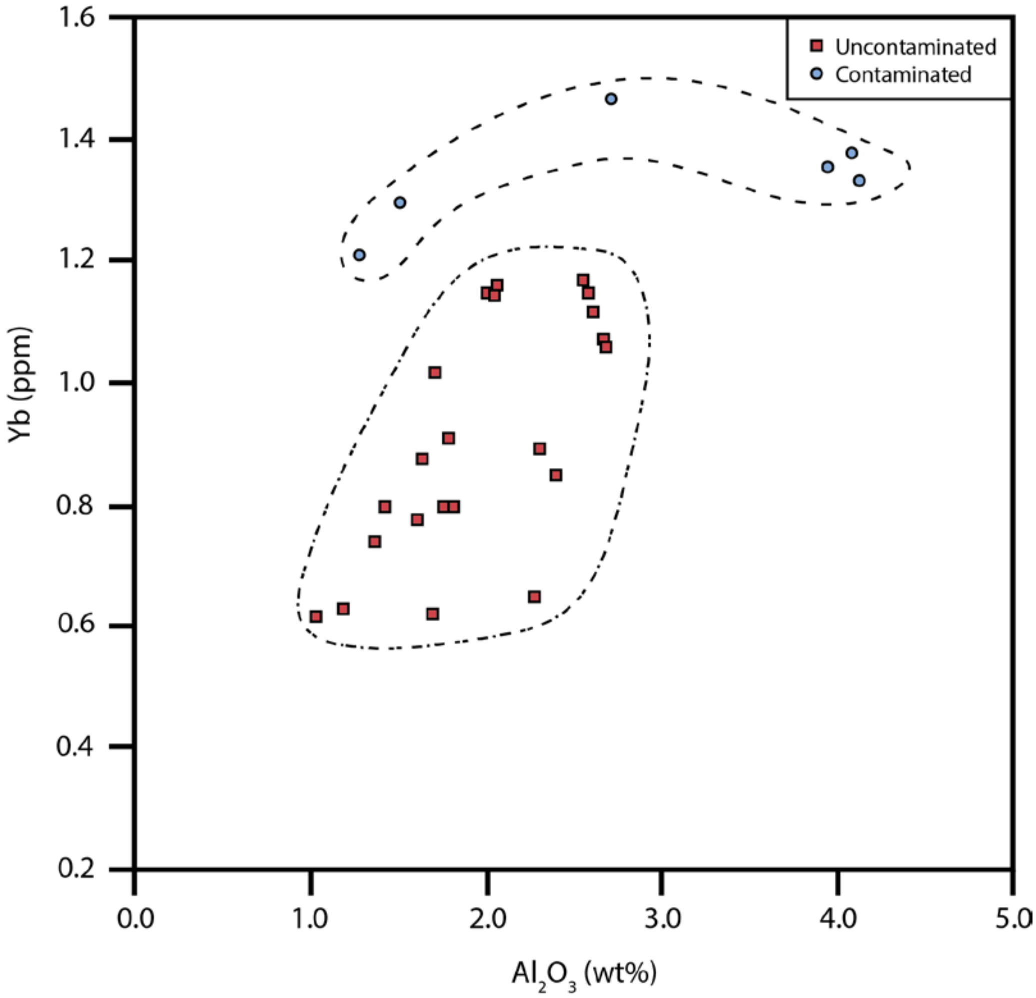

Figure A.9: An Al_2O_3 versus Yb filter for kimberlites just off the Kaapvaal craton.

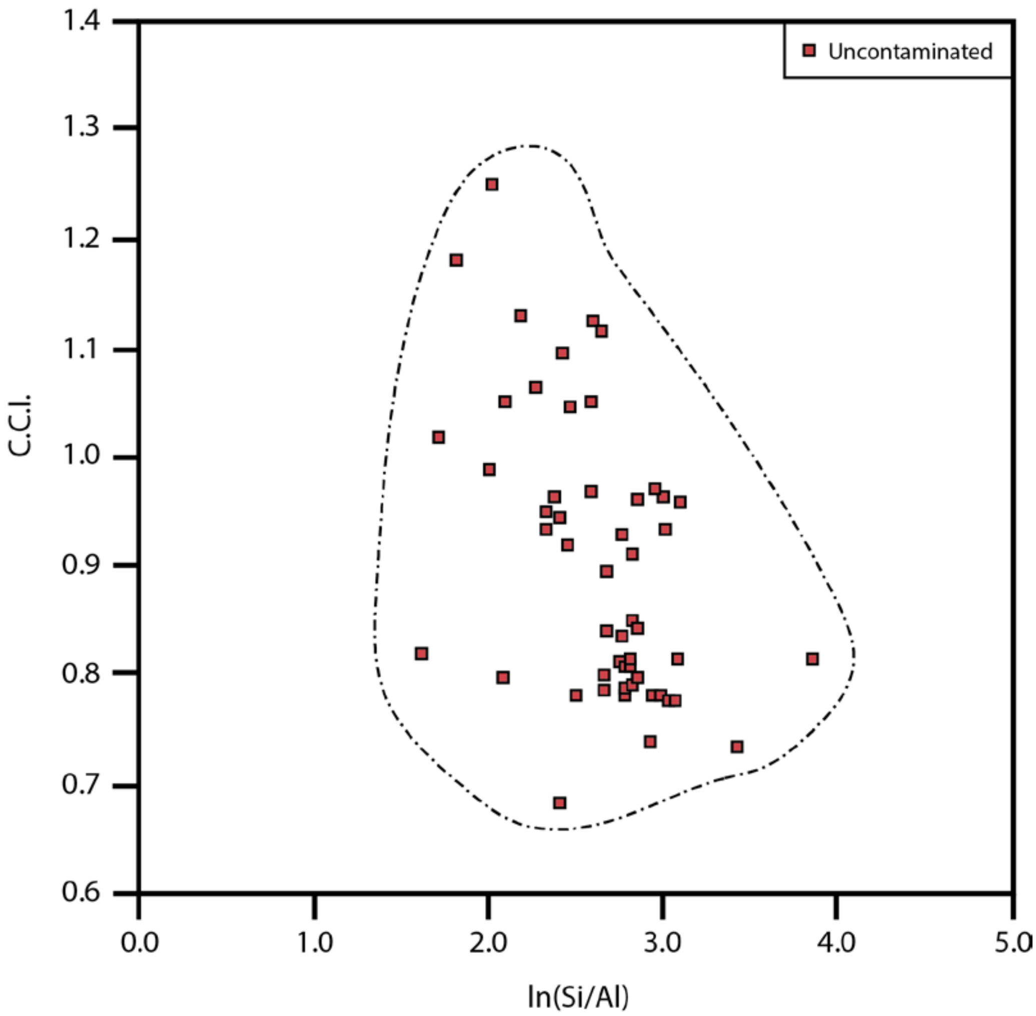

Figure A.10: A C.C.I versus ln(Si/Al) filter for kimberlites from the North American Craton.

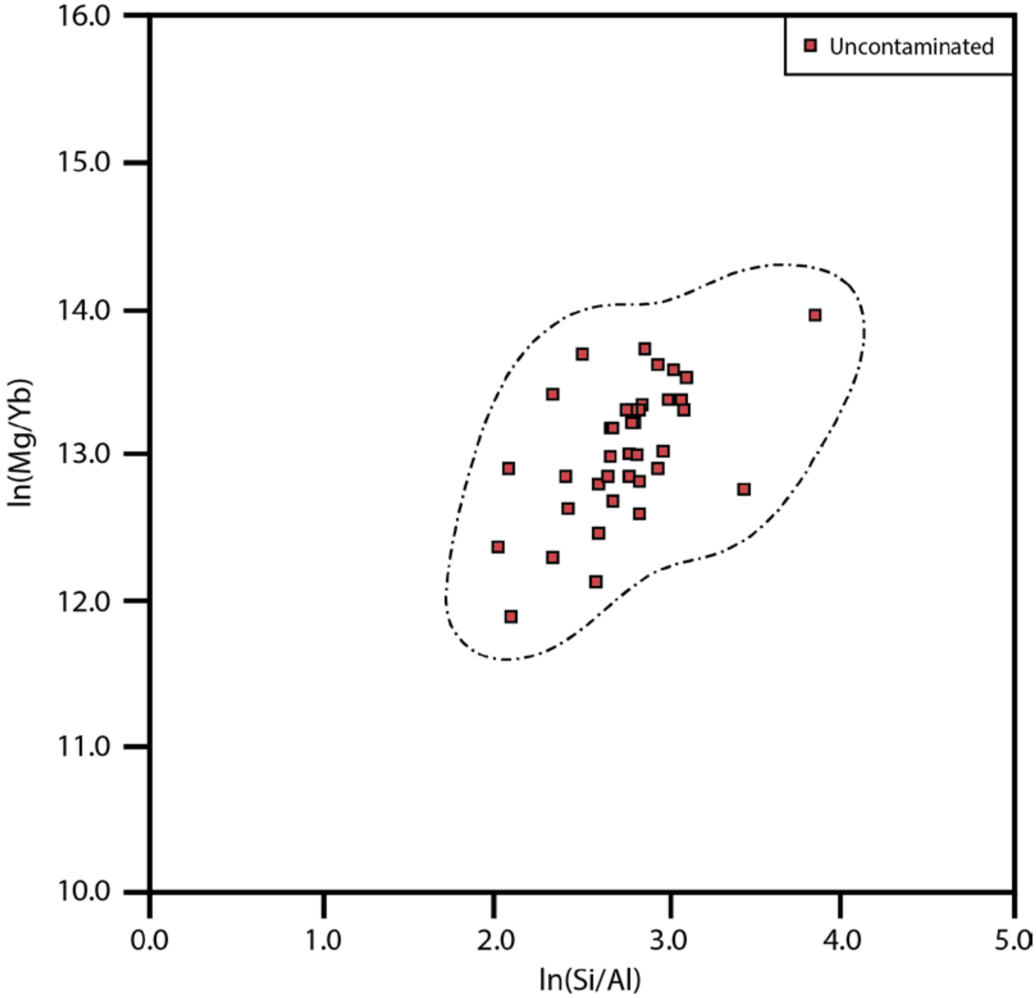

Figure A.11: A ln(Mg/Si) versus ln(Si/Al) filter for kimberlites from the North American Craton.

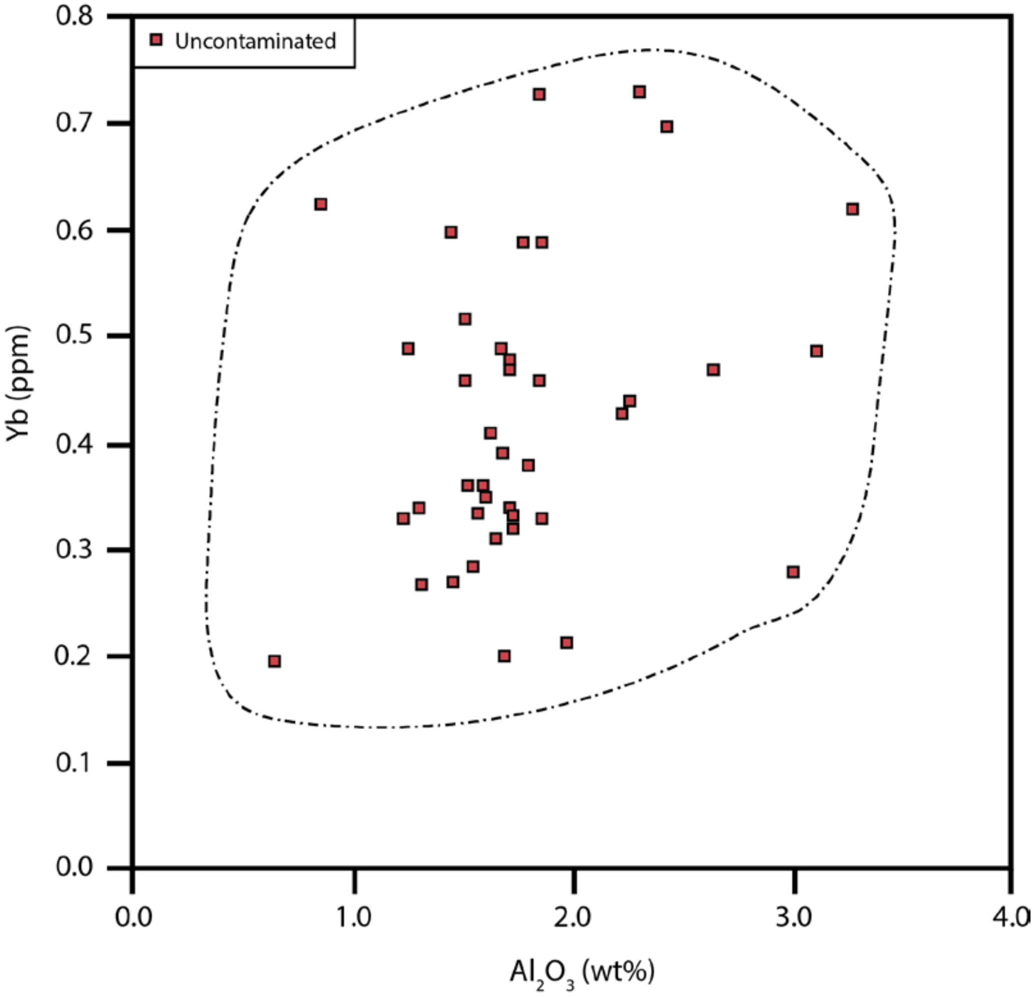

Figure A.12: An Al_2O_3 versus Yb filter for kimberlites from the North American Craton.

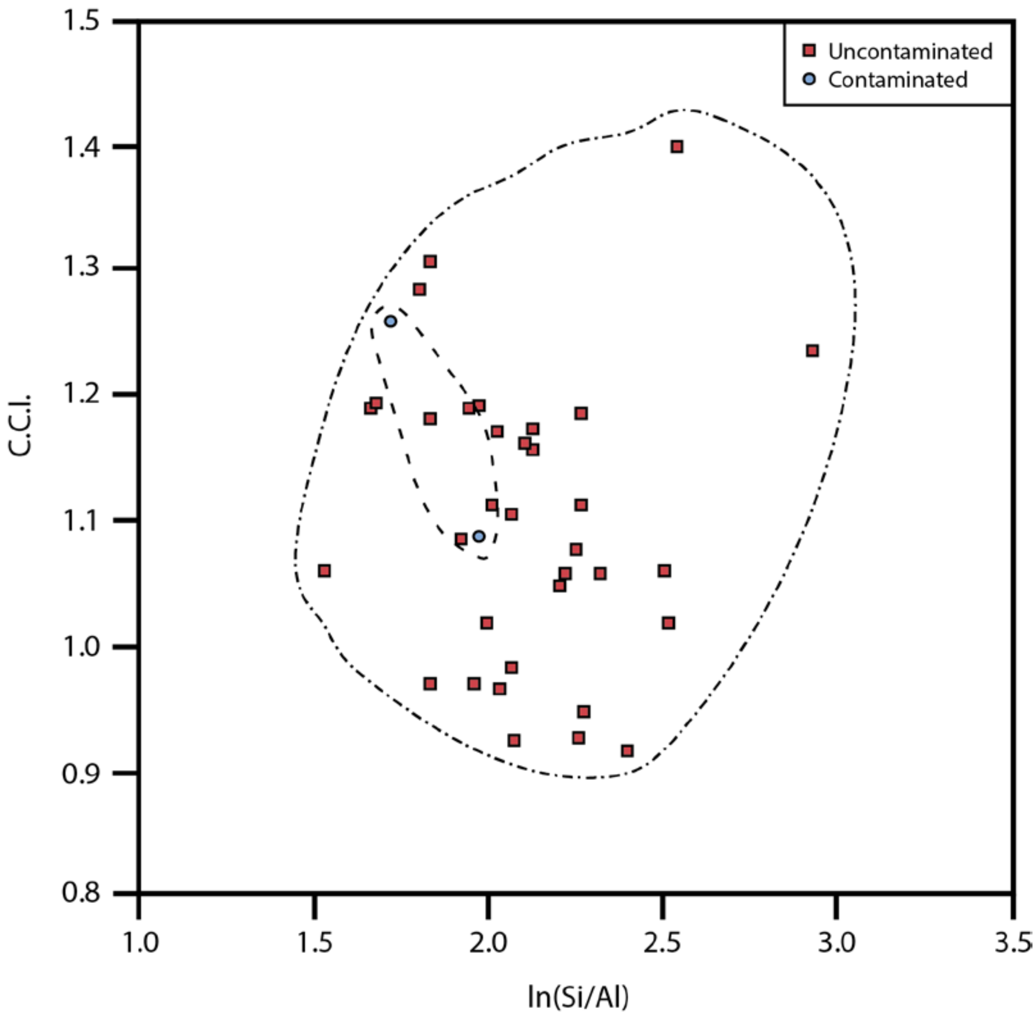

Figure A.13: A C.C.I versus ln(Si/Al) filter for kimberlites from the Sino-Korean, West African, and Russian cratons.

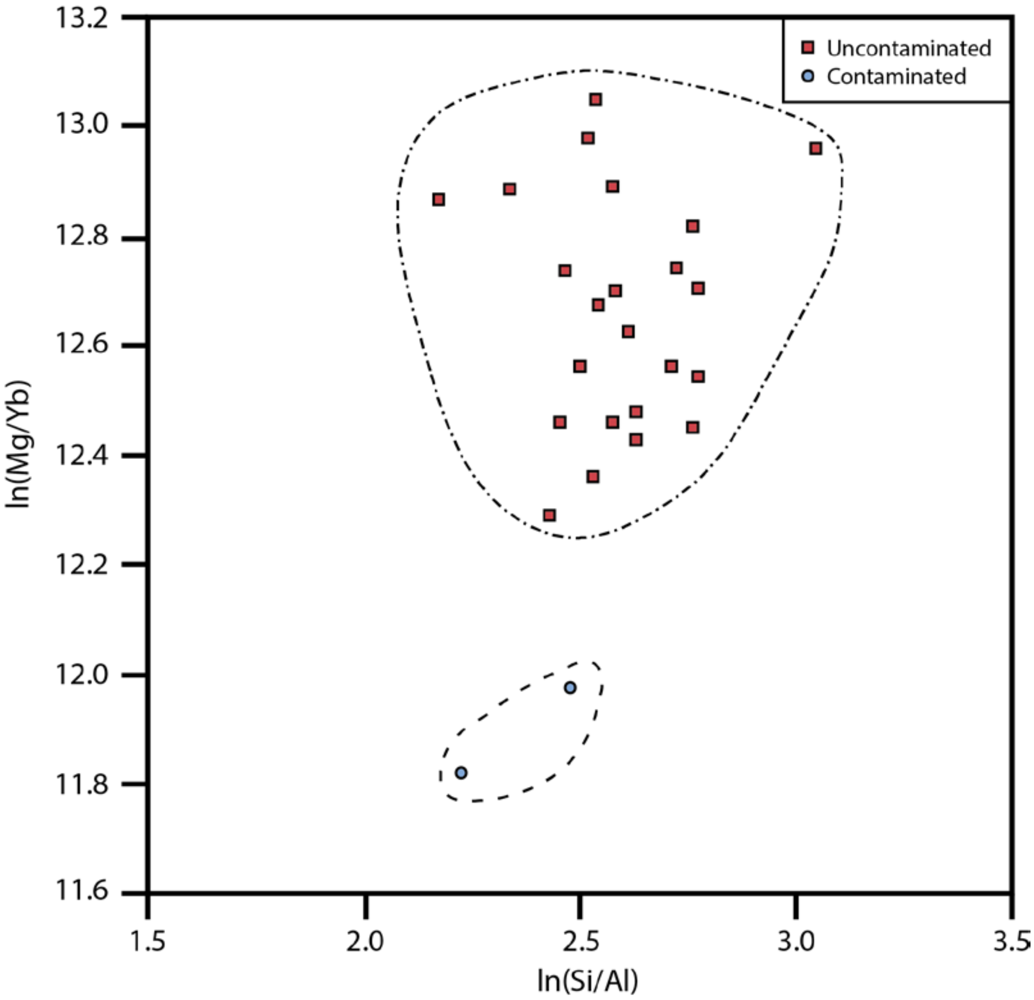

Figure A.14: A ln(Mg/Si) versus ln(Si/Al) filter for kimberlites from the Sino-Korean, West African, and Russian cratons.

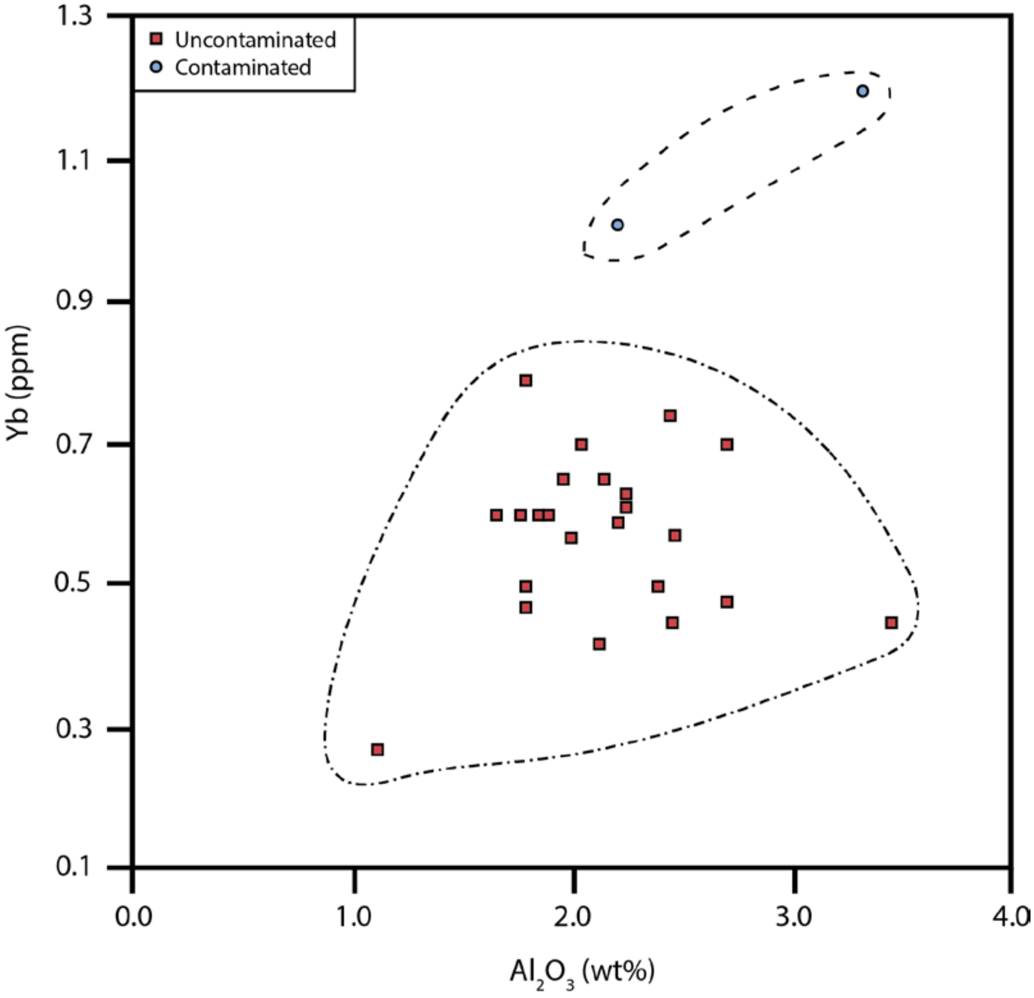

Figure A.15: An Al_2O_3 versus Yb filter for kimberlites from the Sino-Korean, West African, and Russian cratons.

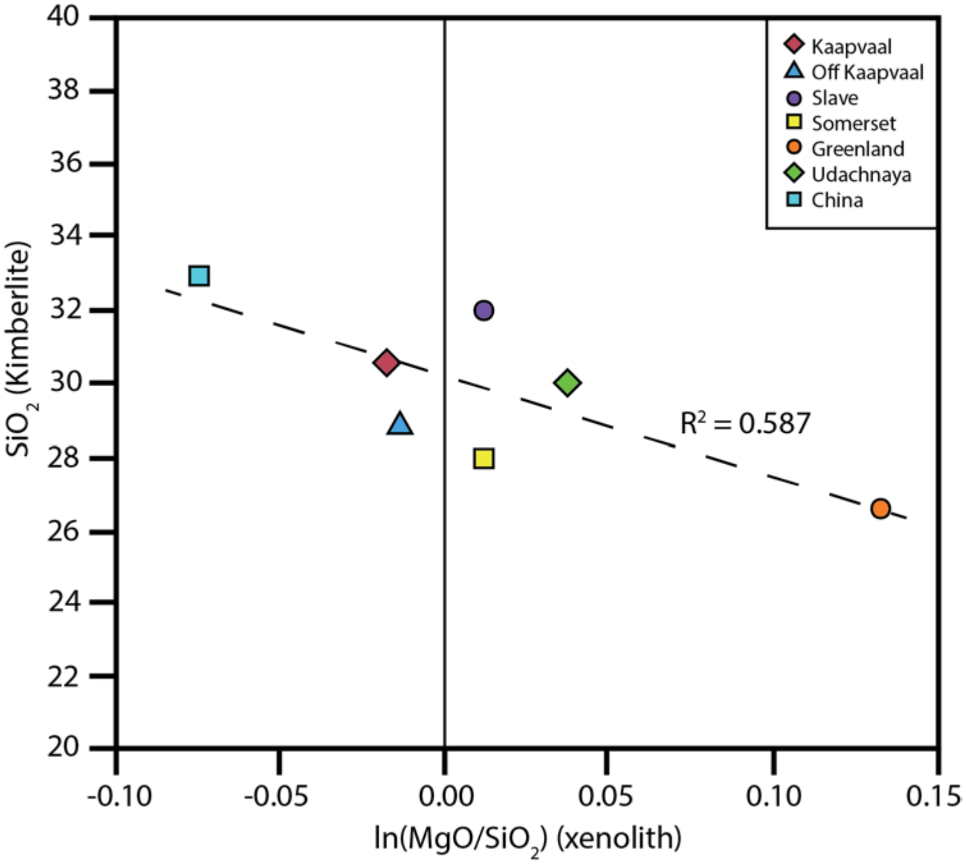

Figure A.16: The average kimberlite SiO_2 content in wt.% versus the average xenolith $\ln(MgO/SiO_2)$ for each craton.

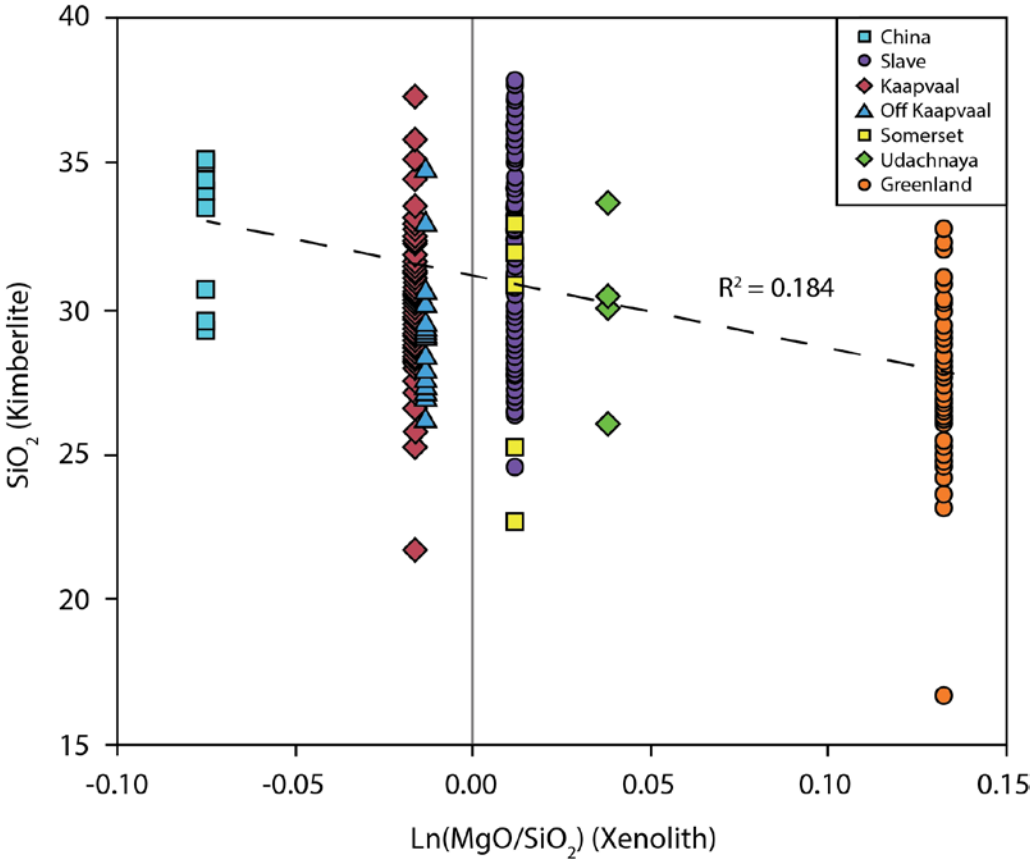

Figure A.17: Each individual kimberlite SiO_2 content versus the average xenolith ln(MgO/SiO_2) for each craton.

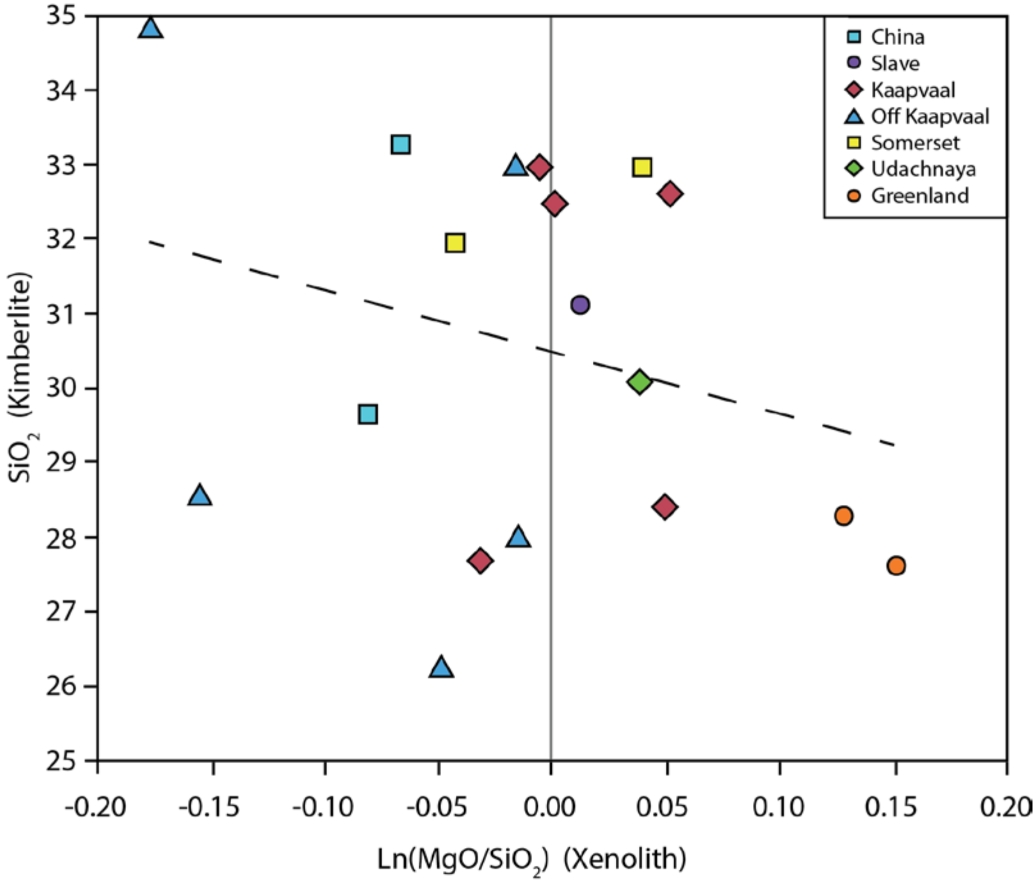

Figure A.18: The average SiO_2 kimberlite content versus the average xenolith $\ln(MgO/SiO_2)$ for the kimberlite fields listed in Table A.9.

Appendix A.5 Tables:

Table A.8: Average Kimberlite SiO_2 Concentration versus Average Xenolith Petrology

Locality	Kimberlite	Xenolith	
	SiO_2 (wt%)	MgO/SiO_2	$\ln(Mg/SiO_2)$
Rae	28.76	1.012	0.012
Slave	32.21	1.012	0.012
Off Kaapvaal	28.90	0.986	-0.014
Kaapvaal	30.88	0.983	-0.017
Sino-Korean	33.32	0.928	-0.075
Udachnaya	30.10	1.038	0.038
North American	27.33	1.142	0.132

Table A.9: Individual Kimberlite SiO_2 Content versus matching Xenolith Petrology

Craton	Locality	Kimberlite	Xenolith	
		SiO_2 (wt%)	MgO/SiO_2	$\ln(MgO/SiO_2)$
Slave	Slave	31.13	1.012	0.012
Rae	SI Batty Bay	32.00	0.958	-0.043
	SI Nord	33.00	1.039	0.039
Kaapvaal	Bultfontein	27.72	0.968	-0.032
	Frank Smith	32.66	1.053	0.052
	Jagersfontein	32.98	0.994	-0.006
	Monastery	28.41	1.050	0.049
	Premier	32.50	1.001	0.001
Off Kaapvaal	Venetia	28.57	0.856	-0.156
	Gibeon	33.00	0.985	-0.015
	Hebron	26.25	0.952	-0.049
	Melton Wold	34.90	0.837	-0.178
	Uintiesberg	27.99	0.985	-0.015
Sino-Korean	Fuxian	29.67	0.922	-0.081
	Mengyin	33.32	0.935	-0.067
Udachnaya	Yakutsk Udachnaya	30.10	1.038	0.038
North American	Pyramidefjeld	27.65	1.162	0.150
	Sarfartoq	28.31	1.136	0.127

References

2015, T Distribution Critical Values Table, Volume 2015: https://www.easycalculation.com/statistics/t-distribution-critical-value-table.php, Hiox India.

Bernstein, S., Hanghøj, K., Kelemen, P., and Brooks, C. K., 2006, Ultra-depleted, shallow cratonic mantle beneath West Greenland: dunitic xenoliths from Ubekendt Ejland: Contributions to Mineralogy and Petrology, v. 152, no. 3, p. 335-347.

Bizzarro, M., and Stevenson, R., 2003, Major element composition of the lithospheric mantle under the North Atlantic craton: Evidence from peridotite xenoliths of the Sarfartoq area, southwestern Greenland: Contributions to Mineralogy and Petrology, v. 146, no. 2, p. 223-240.

Boyd, F., and England, J., 1960, Apparatus for phase-equilibrium measurements at pressures up to 50 kilobars and temperatures up to 1750° C: Journal of Geophysical Research, v. 65, no. 2, p. 741-748.

Boyd, F. R., Pearson, D. G., Hoal, K. O., Hoal, B. G., Nixon, P. H., Kingston, M. J., and Mertzman, S. A., 2004, Garnet lherzolites from Louwrensia, Namibia: bulk composition and P/T relations: Lithos, v. 77, no. 1–4, p. 573-592.

Boyd, F. R., Pokhilenko, N. P., Pearson, D. G., Mertzman, S. A., Sobolev, N. V., and Finger, L. W., 1997, Composition of the Siberian cratonic mantle: evidence from Udachnaya peridotite xenoliths: Contributions to Mineralogy and Petrology, v. 128, no. 2-3, p. 228-246.

Brearley, M., and Scarfe, C. M., 1986, Dissolution Rates of Upper Mantle Minerals in an Alkali Basalt Melt at High Pressure: An Experimental

Study and Implications for Ultramafic Xenolith Survival: Journal of Petrology, v. 27, no. 5, p. 1157-1182.

Brett, R. C., Russell, J. K., Andrews, G. D. M., and Jones, T. J., 2015, The ascent of kimberlite: Insights from olivine: Earth and Planetary Science Letters, v. 424, p. 119-131.

Brett, R. C., Russell, J. K., and Moss, S., 2009, Origin of olivine in kimberlite: Phenocryst or impostor?: Lithos, v. 112, p. 201-212.

Brey, G. P., Bulatov, V. K., Girnis, A. V., and Lahaye, Y., 2007, Experimental Melting of Carbonated Peridotite at 6-10 GPa: Journal of Petrology, v. 49, no. 4, p. 797-821.

Brooker, R. A., Sparks, R. S. J., Kavanagh, J. L., and Field, M., 2011, The volatile content of hypabyssal kimberlite magmas: some constraints from experiments on natural rock compositions: Bulletin of Volcanology, v. 73, no. 8, p. 959-981.

Bussweiler, Y., Foley, S. F., Prelević, D., and Jacob, D. E., 2015, The olivine macrocryst problem: New insights from minor and trace element compositions of olivine from Lac de Gras kimberlites, Canada: Lithos, v. 220–223, no. 0, p. 238-252.

Canil, D., and Bellis, A. J., 2008, Phase equilibria in a volatile-free kimberlite at 0.1 MPa and the search for primary kimberlite magma: Lithos, v. 105, no. 1-2, p. 111-117.

Canil, D., and Fedortchouk, Y., 1999, Garnet dissolution and the emplacement of kimberlites: Earth and Planetary Science Letters, v. 167, no. 227-237.

Canil, D., and O'Neill, H. S. C., 1996, Distribution of Ferric Iron in some Upper-Mantle Assemblages: Journal of Petrology, v. 37, no. 3, p. 609-635.

Canil, D., and Scarfe, C. M., 1990, Phase Relations in Peridotite + CO_2 Systems to 12 GPa: Implications for the Origin of Kimberlite and Carbonate Stability in the Earth's Upper Mantle: J. Geophys. Res., v. 95, no. B10, p. 15805-15816.

Chepurov, A. I., Zhimulev, E. I., Agafonov, L. V., Sonin, V. M., Chepurov, A. A., and Tomilenko, A. A., 2013, The stability of ortho- and clinopyroxenes, olivine, and garnet in kimberlitic magma: Russian Geology and Geophysics, v. 54, p. 406-415.

Clement, C. R., 1982, A comparative geologic study of some major kimberlite pipes in the Northern Cape and Orange Free State [Ph.D. Thesis: University of Cape Town.

Dalton, J. A., and Presnall, D. C., 1998a, Carbonatitic melts along the solidus of model lherzolite in the system CaO-MgO-Al2O3-SiO2-CO2 from 3 to 7 GPa: Contributions to Mineralogy and Petrology, v. 131, no. 2-3, p. 123-135.

Dalton, J. A., and Presnall, D. C., 1998b, The continuum of primary carbonatitic-kimberlitic melt compositions in equilibrium with lherzolite: Data from the system CaO-MgO-Al_2O_3-SiO_2-CO_2 at 6 GPa: Journal of Petrology, v. 39, no. 11 & 12, p. 1953-1964.

Dasgupta, R., and Hirschmann, M., 2007, A modified iterative sandwich method for determination of near-solidus partial melt compositions. II. Application to determination of near-solidus melt compositions of carbonated peridotite: Contributions to Mineralogy and Petrology, v. 154, no. 6, p. 647-661.

Dasgupta, R., and Hirschmann, M. M., Effect of variable carbonate concentration on the solidus of mantle peridotite: American Mineralogist, v. 92, no. 2-3, p. 370-379.

Dasgupta, R., Hirschmann, M. M., and Withers, A. C., 2004, Deep global cycling of carbon constrained by the solidus of anhydrous, carbonated eclogite under upper mantle conditions: Earth and Planetary Science Letters, v. 227, no. 1–2, p. 73-85.

Dawson, J. B., 1994, Quaternary kimberlitic volcanism on the Tanzania Craton: Contributions to Mineral Petrology, v. 116, p. 473-485.

Edgar, A. D., 1973, Experimetnal Petrology: Basic principles and techniques, Oxford, Clarendon Press.

Eggler, D. H., 1978, The effect of CO2 upon partial melting of peridotite in the system Na_2O-CaO-Al_2O3-MgO-SiO_2-CO_2 to 35 kb, with an analysis of melting in a peridotite-H_2O-CO_2 system: American Journal of Science, v. 278, no. 3, p. 305-343.

Eggler, D. H., Kushiro, I., and Holloway, J. R., 1979, Free energies of decarbonation reactions at mantle pressures; I, Stability of the assemblage forsterite-enstatite-magnesite in the system MgO-SiO 2 -CO 2 -H 2 O to 60 kbar: American Mineralogist, v. 64, no. 3-4, p. 288-293.

Eggler, D. H., and Wendlandt, R. F., 1979a, Experimental studies on the relationship between kimberlite magmas and partial melting of peridotite, Kimberlites, Diatremes, and Diamonds: Their Geology, Petrology, and Geochemistry, Volume 15: Washington, DC, AGU, p. 330-338.

-, 1979b, Experimental studies on the relationship between kimberlite magmas and partial melting of peridotite, Washington, DC, American Geological Union, Proceedings of the Second International Kimberlite Conference, 330-338 p.:

Emeleus, C. H., and Andrews, J. R., 1975, Mineralogy and petrology of kimberlite dyke and sheet intrusions and included peridotite xenoliths from South-West Greenland: Physics and Chemistry of the Earth, v. 9, no. 0, p. 179-197.

Enggist, A., Chu, L., and Luth, R. W., 2012, Phase relations of phlogopite with magnesite from 4 to 8 GPa: Contributions to Mineral Petrology, v. 163, p. 467-481.

Foley, S. F., Yaxley, G. M., Rosenthal, A., Buhre, S., Kiseeva, E. S., Rapp, R. P., and Jacob, D. E., 2009, The composition of near-solidus melts of peridotite in the presence of CO_2 and H_2O between 40 and 60 kbar: Lithos, v. 112, p. 274-283.

Gaffney, A. M., Blichert-Toft, J., Nelson, B. K., Bizzarro, M., Rosing, M., and Albarède, F., 2007, Constraints on source-forming processes of West Greenland kimberlites inferred from Hf–Nd isotope systematics: Geochimica et Cosmochimica Acta, v. 71, no. 11, p. 2820-2836.

Ghosh, S., Litasov, K., and Ohtani, E., 2014, Phase relations and melting of carbonated peridotite between 10 and 20 GPa: a proxy for alkali- and CO2-rich silicate melts in the deep mantle: Contributions to Mineralogy and Petrology, v. 167, no. 2, p. 1-23.

Ghosh, S., Ohtani, E., Litasov, K. D., and Terasaki, H., 2009, Solidus of carbonated peridotite from 10 to 20 GPa and origin of magnesiocarbonatite melt in the Earth's deep mantle: Chemical Geology, v. 262, no. 1–2, p. 17-28.

Girnis, A. V., Brey, G. P., and Ryabchikov, I. D., 1995, Origin of Group 1A kimberlites: Fluid-saturated melting experiments at 45–55 kbar: Earth and Planetary Science Letters, v. 134, no. 3–4, p. 283-296.

Girnis, A. V., Bulatov, V. K., and Brey, G. P., 2011, Formation of primary kimberlite melts – Constraints from experiments at 6–12GPa and variable CO_2/H_2O: Lithos, v. 127, no. 3-4, p. 401-413.

Grégoire, M., Bell, D., and Le Roex, A., 2002, Trace element geochemistry of phlogopite-rich mafic mantle xenoliths: their classification and their relationship to phlogopite-bearing peridotites and kimberlites revisited: Contributions to Mineralogy and Petrology, v. 142, no. 5, p. 603-625.

Griffin, W. L., Doyle, B. J., Ryan, C. G., Pearson, N. J., O'Reilly, S. Y., Davies, R., Kivi, K., Achterbergh, E. V., and Natapov, L. M., 1999, Layered Mantle Lithosphere in the Lac de Gras Area, Slave Craton: Composition, Structure and Origin: Journal of Petrology, v. 40, no. 5, p. 705-727.

Griffin, W. L., O'Reilly, S. Y., Natapov, L. M., and Ryan, C. G., 2003a, The evolution of lithospheric mantle beneath the Kalahari Craton and its margins: Lithos, v. 71, no. 2–4, p. 215-241.

Griffin, W. L., O’Reilly, S. Y., Abe, N., Aulbach, S., Davies, R. M., Pearson, N. J., Doyle, B. J., and Kivi, K., 2003b, The origin and evolution of Archean lithospheric mantle: Precambrian Research, v. 127, no. 1–3, p. 19-41.

Gudfinnsson, G. H., and Presnall, D. C., 2005, Continuous Gradations among Primary Carbonatitic, Kimberlitic, Melilititic, Basaltic, Picritic, and Komatiitic Melts in Equilibrium with Garnet Lherzolite at 3–8 GPa: Journal of Petrology, v. 46, no. 8, p. 1645-1659.

Harmer, R. E., and Gittins, J., 1997, The origin of dolomitic carbonatites: field and experimental constraints: Journal of African Earth Sciences, v. 25, no. 1, p. 5-28.

Harris, M., le Roex, A., and Class, C., 2004, Geochemistry of the Uintjiesberg kimberlite, South Africa: petrogenesis of an off-craton, group I, kimberlite: Lithos, v. 74, no. 3–4, p. 149-165.

Harte, B., 1983, Mantle Peridotites and Processes - the Kimberlite Sample, *in* C.J., H., and M.J., N., eds., Continental Basalts and Mantle Xenoliths, Shiva

Hirschmann, M. M., 2000, Mantle solidus: experimental constraints and the effects of peridotite composition: Geochemistry, Geophysics, Geosystems, v. 1, no. 10.

Ionov, D. A., Doucet, L. S., and Ashchepkov, I. V., 2010, Composition of the Lithospheric Mantle in the Siberian Craton: New Constraints from Fresh Peridotites in the Udachnaya-East Kimberlite: Journal of Petrology, v. 51, no. 11, p. 2177-2210.

Irvine, G. J., Pearson, D. G., Kjarsgaard, B. A., Carlson, R. W., Kopylova, M. G., and Dreibus, G., 2003, A Re–Os isotope and PGE study of kimberlite-derived peridotite xenoliths from Somerset Island and a comparison to the Slave and Kaapvaal cratons: Lithos, v. 71, no. 2–4, p. 461-488.

Janney, P. E., Shirey, S. B., Carlson, R. W., Pearson, D. G., Bell, D. R., Le Roex, A. P., Ishikawa, A., Nixon, P. H., and Boyd, F. R., 2010, Age, Composition and Thermal Characteristics of South African Off-Craton Mantle Lithosphere: Evidence for a Multi-Stage History: Journal of Petrology.

Kamenetsky, V. S., Grütter, H., Kamenetsky, M. B., and Gömann, K., 2012, Parental carbonatitic melt of the Koala kimberlite (Canada): Constraints from melt inclusions in olivine and Cr-spinel, and groundmass carbonate: Chemical Geology, v. In Press.

Kamenetsky, V. S., and Yaxley, G. M., 2015, Carbonate–silicate liquid immiscibility in the mantle propels kimberlite magma ascent: Geochimica et Cosmochimica Acta, v. 158, no. 0, p. 48-56.

Keshav, S., and Gudfinnsson, G., H., 2014, Melting phase equilibria of model carbonated peridotite from 8 to 12 GPa in the system CaO-MgO-Al2O3-SiO2-CO2 and kimberlitic liquids in the Earth's upper mantle, American Mineralogist, Volume 99, p. 1119.

Kjarsgaard, B. A., Pearson, D. G., Tappe, S., Nowell, G. M., and Dowall, D. P., 2009, Geochemistry of hypabyssal kimberlites from Lac de Gras, Canada: Comparisons to a global database and applications to the parent magma problem: Lithos, v. 112, Supplement 1, no. 0, p. 236-248.

Klein-BenDavid, O., Izraeli, E. S., Hauri, E., and Navon, O., 2007, Fluid inclusions in diamonds from the Diavik mine, Canada and the evolution of diamond-forming fluids: Geochimica et Cosmochimica Acta, v. 71, no. 3, p. 723-744.

Kopylova, M. G., Matveev, S., and Raudsepp, M., 2007, Searching for parental kimberlite melt: Geochimica et Cosmochimica Acta, v. 71, no. 14, p. 3616-3629.

Kopylova, M. G., Russell, J. K., and Cookenboo, H., 1999, Petrology of Peridotite and Pyroxenite Xenoliths from the Jericho Kimberlite: Implications for the Thermal State of the Mantle beneath the Slave Craton, Northern Canada: Journal of Petrology, v. 40, no. 1, p. 79-104.

Kushiro, I., 1970, Systems bearing on melting of the upper mantle under hydrous conditions: Carnegie Institution of Washington Yearbook v. 1968-69, p. 240-245.

Larsen, L. M., and Rex, D. C., 1992, A review of the 2500 Ma span of alkaline-ultramafic, potassic and carbonatitic magmatism in West Greenland: Lithos, v. 28, no. 3–6, p. 367-402.

Le Roex, A. P., Bell, D. R., and Davis, P., 2003, Petrogenesis of Group 1 Kimberlites from Kimberley, South Africa: Evidence from Bulk-rock Geochemistry: Journal of Petrology, v. 44, no. 12, p. 2261-2286.

Litasov, K. D., and Ohtani, E., 2009, Solidus and phase relations of carbonated peridotite in the system CaO–Al2O3–MgO–SiO2–Na2O–CO2 to the lower mantle depths: Physics of the Earth and Planetary Interiors, v. 177, no. 1–2, p. 46-58.

Litasov, K. D., Shatskiy, A., Ohtani, E., and Yaxley, G. M., 2013, Solidus of alkaline carbonatite in the deep mantle: Geology, v. 41, no. 1, p. 79-82.

Maier, W. D., Peltonen, P., McDonald, I., Barnes, S. J., Barnes, S. J., Hatton, C., and Viljoen, F., 2012, The concentration of platinum-group elements and gold in southern African and Karelian kimberlite-hosted mantle xenoliths: Implications for the noble metal content of the Earth's mantle: Chemical Geology, v. 302–303, p. 119-135.

Mitchell, R., 1986, Kimberlites: Mineralogy, geochemistry, and petrology, New York, Plenum.

Mitchell, R. H., 1973, Composition of olivine, silica activity and oxygen fugacity in kimberlite: Lithos, v. 6, p. 65-81.

Mitchell, R. H., 2004, Experimental studies At 5–12 GPa of the Ondermatjie hypabyssal kimberlite: Lithos, v. 76, no. 1–4, p. 551-564.

-, 2008, Petrology of hypabyssal kimberlites: Relevance to primary magma compositions: Journal of Volcanology and Geothermal Research, v. 174, no. 1-3, p. 1-8.

Moore, K. R., and Wood, B. J., 1998, The Transition from Carbonate to Silicate Melts in the $CaO-MgO-SiO_2-CO_2$ System: Journal of Petrology, v. 39, no. 11 & 12, p. 1943-1951.

Mysen, B., Virgo, D., and Scarfe, C., 1979, Viscosity of silicate melts as a function of pressure: structural interpretation: Carnegie Inst Washington Yearb, v. 78, p. 551-556.

Nixon, P. H., Rogers, N. W., Gibson, I. L., and Grey, A., 1981, Depleted and Fertile Mantle Xenoliths from Southern African Kimberlites: Annual Review of Earth and Planetary Sciences, v. 9, no. 1, p. 285-309.

Patterson, M., Francis, D., and McCandless, T., 2009, Kimberlites: Magmas or mixtures?: Lithos, v. 112, Supplement 1, no. 0, p. 191-200.

Pearson, D., Canil, D., and Shirey, S., 2003, Mantle samples included in volcanic rocks: xenoliths and diamonds: Treatise on geochemistry, v. 2, p. 171-275.

Pearson, D. G., Irvine, G. J., Ionov, D. A., Boyd, F. R., and Dreibus, G. E., 2004, Re–Os isotope systematics and platinum group element fractionation during mantle melt extraction: a study of massif and xenolith peridotite suites: Chemical Geology, v. 208, no. 1–4, p. 29-59.

Pilbeam, L. H., Nielsen, T. F. D., and Waight, T. E., 2013, Digestion Fractional Crystllization (DFC): an Important Process in the Genesis of Kimberlites. Evidence from Olivine in the Majuagaa Kimberlite, Southern West Greenland: Journal of Petrology, v. 0, no. 0, p. 1-17.

Powell, R., and Holland, T. J. B., 1988, An internally consistent dataset with uncertainties and correlations; 3, Applications to geobarometry, worked examples and a computer program: Journal of Metamorphic Geology, v. 6, p. 173-204.

Price, S. E., Russell, J. K., and Kopylova, M. G., 2000, Primitive Magma from the Jericho Pipe, N.W.T., Canada: Constraints on Primary Kimberlite Melt Chemistry: Journal of Petrology, v. 41, p. 789-808.

Ringwood, A. E., Kesson, S. E., Hibberson, W., and Ware, N., 1992, Origin of kimberlites and related magmas: Earth and Planetary Science Letters, v. 113, no. 4, p. 521-538.

Russell, J. K., Porritt, L. A., Lavallee, Y., and Dingwell, D. B., 2012, Kimberlite ascent by assimilation-fuelled buoyancy: Nature, v. 481, no. 7381, p. 352-356.

Schmidberger, S. S., and Francis, D., 1999, Nature of the mantle roots beneath the North American craton: mantle xenolith evidence from Somerset Island kimberlites: Lithos, v. 48, no. 1–4, p. 195-216.

Shaw, C. S. J., 1999, Dissolution of orthopyroxene in basanitic magma between 0.4 and 2 GPa: further implications for the origin of Si-rich alkaline glass inclusions in mantle xenoliths: Contributions to Mineral Petrology, v. 135, p. 114-132.

Shaw, C. S. J., Thibault, Y., Edgar, A. D., and Lloyd, F. E., 1998, Mechanisms of orthopyroxene dissolution in silica-undersaturated melts at 1 atmosphere and implications for the origin of silica-rich glass in mantle xenoliths: Contributions to Mineralogy, v. 132, p. 354-370.

Shirey, S. B., Cartigny, P., Frost, D. J., Keshav, S., Nestola, F., Nimis, P., Pearson, D. G., Sobolev, N. V., and Walter, M. J., 2013, Diamonds and the geology of mantle carbon: Rev Mineral Geochem, v. 75, no. 1, p. 355-421.

Simon, N. S., Carlson, R. W., Pearson, D. G., and Davies, G. R., 2007, The origin and evolution of the Kaapvaal cratonic lithospheric mantle: Journal of Petrology.

Sparks, R. S. J., Brooker, R. A., Field, M., Kavanagh, J., Schumacher, J. C., Walter, M. J., and White, J., 2009, The nature of erupting kimberlite melts: Lithos, v. 112, Supplement 1, no. 0, p. 429-438.

Stachel, T., and Harris, J. W., 2008, The origin of cratonic diamonds — Constraints from mineral inclusions: Ore Geology Reviews, v. 34, no. 1–2, p. 5-32.

Stachel, T., and Luth, R. W., 2015, Diamond formation — Where, when and how?: Lithos, v. 220–223, p. 200-220.

Stixrude, L., and Lithgow-Bertelloni, C., 2007, Influence of phase transformations on lateral heterogeneity and dynamics in Earth's mantle: Earth and Planetary Science Letters, v. 263, no. 1–2, p. 45-55.

Tappe, S., Pearson, D. G., Nowell, G., Nielsen, T., Milstead, P., and Muehlenbachs, K., 2011, A fresh isotopic look at Greenland kimberlites: Cratonic mantle lithosphere imprint on deep source signal: Earth and Planetary Science Letters, v. 305, no. 1–2, p. 235-248.

Thy, P., Stecher, O., and Korstgård, J. A., 1987, Mineral chemistry and crystallization sequences in kimberlite and lamproite dikes from the Sisimiut area, central West Greenland: Lithos, v. 20, no. 5, p. 391-417.

Wallace, M. E., and Green, D. H., 1988, An experimental determination of primary carbonatite magma composition: Nature, v. 335, no. 6188, p. 343-346.

Walter, M., Thibault, Y., Wei, K., and Luth, R., 1995, Characterizing experimental pressure and temperature conditions in multi-anvil apparatus: Canadian Journal of Physics, v. 73, no. 5-6, p. 273-286.

Wittig, N., Pearson, D. G., Webb, M., Ottley, C. J., Irvine, G. J., Kopylova, M., Jensen, S. M., and Nowell, G. M., 2008, Origin of cratonic lithospheric mantle roots: A geochemical study of peridotites from the North Atlantic Craton, West Greenland: Earth and Planetary Science Letters, v. 274, no. 1–2, p. 24-33.

Wyllie, P., and Huang, W.-L., 1976, Carbonation and melting reactions in the system CaO–MgO–SiO2–CO2 at mantle pressures with geophysical and petrological applications: Contributions to Mineralogy and Petrology, v. 54, no. 2, p. 79-107.

Wyllie, P. J., 1980, The Origin of Kimberlite: Journal of Geophysical Research, v. 85, no. B12, p. 6902-6910.

Wyllie, P. J., and Huang, W.-L., 1975, Peridotite, kimberlite, and carbonatite explained in the system CaO-MgO-SiO2-CO2: Geology, v. 3, no. 11, p. 621-624.

Yaxley, G. M., and Green, D. H., 1996, Experimental reconstruction of sodic dolomitic carbonatite melts from metasomatised lithosphere: Contributions to Mineralogy and Petrology, v. 124, no. 3-4, p. 359-369.

Zheng, J., Griffin, W. L., O'Reilly, S. Y., Yang, J., Li, T., Zhang, M., Zhang, R. Y., and Liou, J. G., 2006, Mineral Chemistry of Peridotites from Paleozoic, Mesozoic and Cenozoic Lithosphere: Constraints on Mantle Evolution beneath Eastern China: Journal of Petrology, v. 47, no. 11, p. 2233-2256.

Zheng, J., Yu, C., Yuan, X., Yin, L., Jiao, S., Tang, H., Zhang, Z., and Lu, F., 2007, Petrochemistry of peridotites from North China: Significance for lithospheric mantle evolution: Frontiers of Earth Science in China, v. 1, no. 1, p. 37-43.